2013

Hydrogen in the Semiconducting Oxides SnO2 and TiO2 Studied by FTIR Spectroscopy

Figen Bekisli
Lehigh University

Hydrogen in the Semiconducting Oxides SnO_2 and TiO_2 Studied by FTIR Spectroscopy

by

Figen Bekisli

A Dissertation

Presented to the Graduate and Research Committee

of Lehigh University

In Candidacy for the Degree of

Doctor of Philosophy

in

Physics

Lehigh University

September 2013

Certificate of Approval

Approved and recommended for acceptance as a dissertation in partial fulfillment of the requirements for the degree of Doctor of Philosophy

Figen Bekisli

"Hydrogen in the Semiconducting Oxides SnO_2 and TiO_2

Studied by FTIR Spectroscopy "

_____
Defense Date

_____
Dissertation Director

_____
Approved Date

Committee Members:

_____
Dr. Michael J. Stavola

_____
Dr. W. Beall Fowler

_____
Dr. James D. Gunton

_____
Dr. Gary G. DeLeo

_____
Dr. Gray E. Bebout

Acknowledgement

During my long, hard but at the same time wonderful journey towards my Ph.D., a great many people have encouraged and supported me in many ways. Foremost, I would like to express my gratitude to my advisor, Professor Michael Stavola, for his guidance, patience, and continuous support throughout this study. He has been an excellent advisor with his immense knowledge and constructive comments; a great mentor with his logical way of thinking, motivation, enthusiasm, and positive attitude. I will always be grateful to him for making my time at Lehigh such an enjoyable and less stressful experience. I would like to thank Professor Beall Fowler for his contributions to the theoretical calculations and simulations in my work. I would like to thank Professor James Gunton who has been very thoughtful and caring, and for making me believe that I can succeed. I am also very grateful to the rest of my Ph.D. Committee members; Professors Gary DeLeo and Gray Bebout for their contributions, and help.

My thanks also go to my lab mates and the previous students working in the Stavola group, especially Dr. Lanlin Wen for teaching me everything she knew about the lab. I would like to thank Joseph Zelinski for helping me in the workshop. I also acknowledge Lois Groff and Pamela Gescek for their assistance in the office. Moreover, I would like to thank the entire faculty and my fellow graduate students for their help and support.

I am so grateful to my friends, Oznur Saygi Arslan and Zumbul Bulut Atan for sharing their experience and being with me from the beginning of my Ph.D. I would like to thank to all

my friends in Bethlehem and Turkey for their support, especially Pinar Guvelioglu and Hamra Bakircioglu.

My acknowledgments would not be complete without thanking to my parents, Mesuriye and Kemal Akdin, and my twin sister, Funda Aydin, for their unselfish love, sacrifice, and support, not only during my Ph.D work, but also throughout my life.

Finally, I would like to try to express my deepest thanks to my husband, Burak Bekisli. He is the reason for me to start and finish my Ph.D. study. None of this would have been possible without his love, encouragement and patience. He has been the voice in my head saying ”You can do it” all the time. Thanks to him for knowing me better than anybody, even myself. No words can explain how much his sacrifices and support have meant to me. I am dedicating this dissertation to my better half and my love, Burak Bekisli.

Table of Contents

List of Figures

List of Tables

Abstract

In this study, hydrogen-containing defects in two semiconducting metal oxides, SnO_2 and TiO_2, have been investigated by FTIR spectroscopy. Transparent conducting oxides are unusual but highly useful materials that combine transparency in the visible range with electrical conductivity. With these unique properties, applications utilizing these materials have been continuously growing in several fields, such as display technology, solar cells, and optoelectronics.

Defects or impurities in the crystal structure of transparent conducting oxides affect the properties of these materials. Although hydrogen is the simplest atom, as an impurity, it plays remarkable roles in the electrical and optical properties of metal oxides. For example, recent research has suggested that hydrogen centers are responsible for the n-type conductivity in many metal oxides, in contrast to the traditionally accepted idea that native defects, such as oxygen vacancies and cation interstitials, are the source of conductivity. In order to utilize transparent conducting oxides to their highest potential, the conductivity needs to be controlled and engineered. However, a modern understanding of the conductivity of transparent conducting oxides and the role played by hydrogen is still at an early stage. In this study, IR spectroscopy experiments have been performed to probe the structures and reaction of hydrogen related centers and their relationship to changes in the conductivity of SnO_2 and TiO_2.

In SnO_2, the relationship between H and the free carriers it introduces has been investigated. The thermal stability of the free carrier absorption and its relationship to the thermal stabilities of the O-H lines have been examined. Distinctive polarization properties of several O-H centers have been used to test microscopic defect models. Temperature dependent interactions between electrically active and inactive defects have been identified by annealing studies.

Studies of TiO_2 have focused on the fundamental O-D center and the strong dependence of its vibrational spectrum on temperature. The behavior of three closely spaced O-D lines have been studied by IR spectroscopy and theory and explained with a small polaron model.

Chapter 1

Introduction: Transparent Conducting Oxides

1.1 Transparent Conducting Oxides

Hydrogen impurities in crystalline semiconducting materials have long been a subject of active research. Even simple imperfections in the crystal structure can cause significant changes in the properties of semiconductors and the electronic devices made from them. Hydrogen impurities, which can be introduced into the crystal structure intentionally or unintentionally, are known to participate in a wide range of phenomena that affect the properties of conventional semiconductor materials; examples are the passivation of donor and acceptor impurities [1.1-1.3], the elimination of the deleterious properties of defects, and even the modification of the band gap of the host crystal [1.1, 1.2, 1.4]. The identification and characterization of hydrogen-related defects are often necessary to understand, control and engineer the properties of semiconductors. Substantial research over recent decades has provided scientists and engineers with a better understanding of hydrogen in commonly used semiconductors such as Si and compounds like GaAs. However, hydrogen is not yet well understood for the case of transparent metal oxides.

Although they have been known for more than a century, the transparent metal oxides are receiving renewed interest as semiconductors. The reason for this growing attention is the unusual coexistence of optical transparency and electrical conductivity. This is attractive for many applications, especially in the optoelectronics and energy areas. A common example of a transparent conducting oxide (TCO) is the indium tin oxide (ITO) system which is widely used

as a transparent electrode in flat panel and touch screen display technology [1.5-1.8] and in solar cells [1.6, 1.9-1.11]. ITO has also found applications in electromagnetic shielding [1.6, 1.8] and thermal management for energy-efficient windows [1.6, 1.8]. Although ITO possesses highly desirable electrical and optical properties [1.12], the scarcity and cost of indium have encouraged researchers to seek alternative TCO materials. The other two TCO's that dominate the market are tin oxide (SnO_2) and zinc oxide (ZnO) [1.13]. SnO_2 is one of the oldest TCOs that found practical use for defrosting windows in airplanes during World War II [1.8]. Subsequently, it has been used in low-emissivity windows for architectural, aerospace and automotive applications [1.5-1.6, 1.8-1.9]; solid-state gas sensors [1.14-1.15]; transparent electrodes in thin film solar cells [1.8, 1.16]; and transparent thin film transistors [1.17]. A lower cost alternative to ITO in applications such as display technology and solar cells is ZnO [1.8, 1.18-1.19]. Titanium oxide (TiO_2) is another metal oxide that has been of recent interest for applications as catalysts in solar cells, paint pigments, optical coatings and gas sensors [1.10, 1.20]. As the demand increases for higher efficiency and higher performance products in the optoelectronics and energy industries, it is natural to assume a growing demand for the unique properties provided by transparent conducting metal oxides.

Due to fundamental differences in the mechanisms that define the electrical and optical properties of metal oxides compared to conventional semiconductors, outcomes of previous research efforts concentrated mainly on the latter class do not necessarily apply to the former. Despite many successful applications of transparent conducting oxides, much remains to be done to understand the sources of their unique properties and effects of other parameters, such as impurities [1.13]. The purpose of this work is to contribute to this understanding by

conducting experimental and theoretical research on hydrogen-related impurities in two common metal oxides, SnO_2 and TiO_2, with the rutile crystal lattice structure. The experimental method employed in this study to detect and identify defects is Fourier transform infrared (FTIR) spectroscopy which will be briefly discussed in the following sections. Prior to that, an introduction to the crystal structures and some properties of metal oxides will be given.

1.2 Selected Crystal Structures of Transparent Conducting Oxides

This section will include basic information about various types of crystal structures that are found in metal oxides and that are important to establish a baseline for the study of these materials. In many cases, understanding of metal oxides requires knowledge of crystal structures that are more exotic than diamond cubic.

The first crystal structure of interest is rutile, which is the crystalline form of SnO_2 and is also the most frequently encountered form for TiO_2. The unit cell of rutile SnO_2 is shown in Fig. 1.1. Each Sn atom is surrounded octahedrally by six oxygen atoms. Two of these oxygen atoms lie in the axial direction while the remaining four are termed as equatorial [1.21]. Each oxygen atom is surrounded by three coplanar Sn atoms, to form an almost equilateral triangle. The low symmetry of this structure makes it an ideal candidate for analysis by vibrational spectroscopy, since vibrational modes have distinctive polarization properties that reveal clues to the structure. TiO_2 has the same rutile structure as SnO_2 with each Sn atom in the structure replaced by Ti.

ZnO has the crystal lattice structure known as wurtzite, which is shown in Fig. 1.2. Each Zn atom is tetrahedrally surrounded by four oxygens atom and vice versa. In addition to ZnO,

many important semiconductors with large band gaps, such as GaN and CdS, crystallize in this form. The structure is similar to zincblende, except for different orientations of the Zn- and O-centered tetrahedra.

Indium oxide (In_2O_3) and crystalline ITO both have the cubic bixbyite crystal structure. A total of 80 atoms form the unit cell for this structure (shown in Fig. 1.3). Although each indium atom has six oxygen neighbors, there are two different configurations for the neighboring oxygens, resulting in two different indium sites. The complexity of this crystal structure makes the analysis of these materials challenging.

The perovskite structure, as shown in Fig. 1.4, is encountered for oxides with the general form of ABO_3, such as $SrTiO_3$ and $CaTiO_3$. In the ideal high symmetry case, perovskites have a simple cubic lattice with A atoms, i.e. Sr or Ca, placed on the corners of the cube, B atoms, i.e. Ti, sitting at the body center and oxygens on the face centers. Many symmetry-lowering distortions of the perovskite lattice are commonly observed, making this a fascinating class of materials.

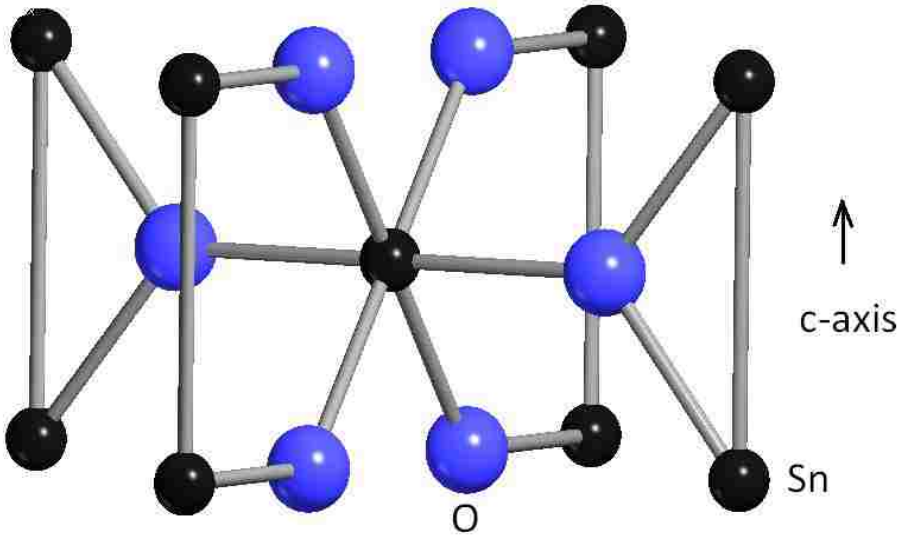

Fig. 1.1: Rutile structure for SnO_2 [1.22]. Compliments of W. B. Fowler.

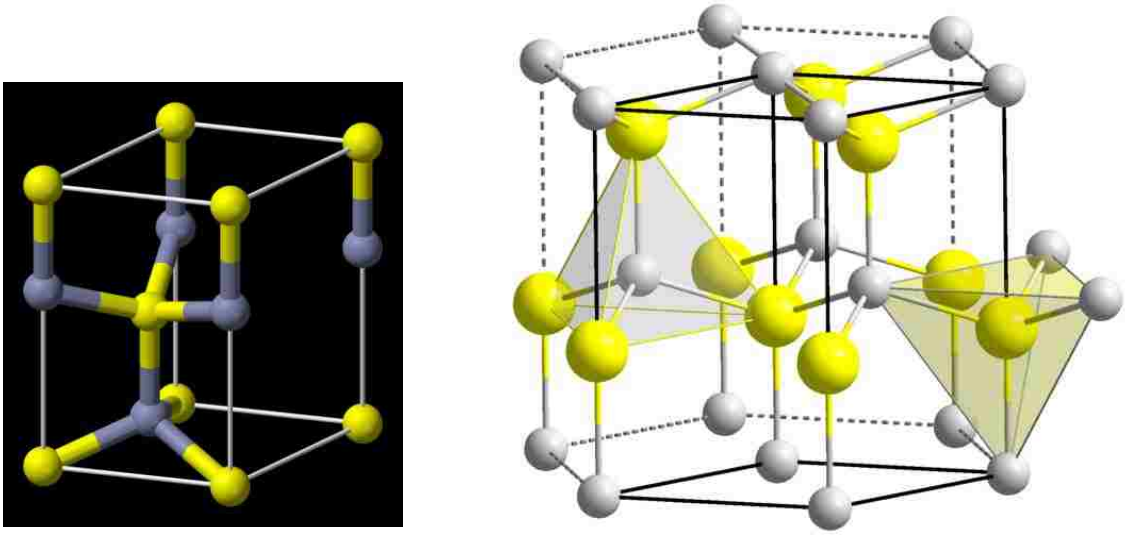

Fig. 1.2: Wurtzite structure, (left) unit cell, (right) orientations of Zn and O-centered tetrahedra.

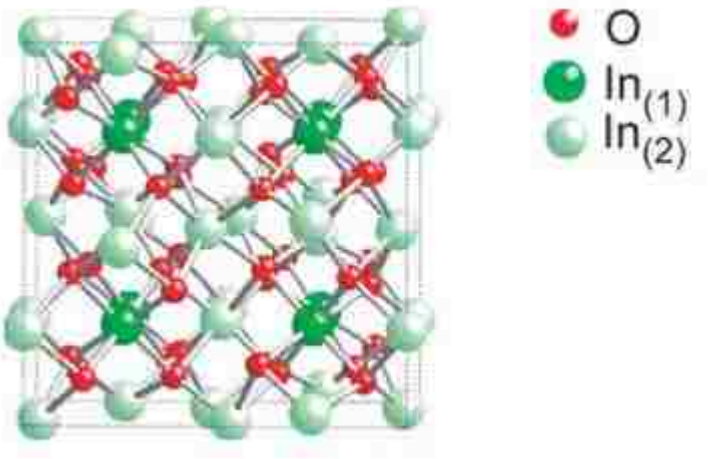

Fig. 1.3: Unit cell structure of bixbyite [1.23].

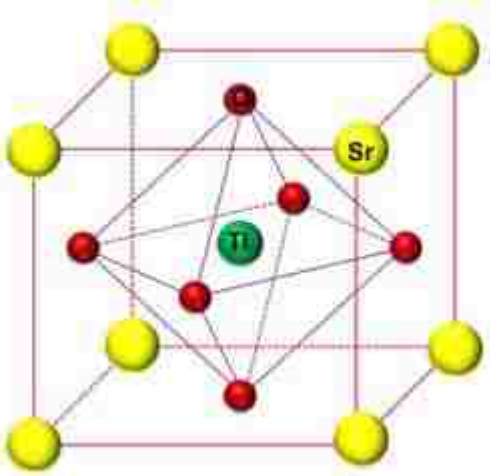

Fig. 1.4: Unit cell of the perovskite structure for $SrTiO_3$ [1.10].

1.3 Conductivity of Transparent Metal Oxides

Transparent metal oxides are wide band gap materials, with a fundamental band gap typically of 3 eV or more [1.6, 1.9, 1.24-1.26], which combine electrical conductivity with optical transparency. A list of a few transparent metal oxides and their corresponding band gaps is given in Table 1.1. With the wide band gaps that are required for optical transparency, these materials might be expected to be insulators in the undoped state at room temperature [1.9]. By increasing the free carrier density through doping, they can be typically converted to n-type semiconducting materials. Although this fact has been known and employed in many successful applications for many decades, the source of n-type conductivity is surprisingly still controversial. Traditionally, native defects such as O vacancies and cation interstitials have been invoked as possible sources of n-type conductivity [1.27-1.30]. However, more recent theoretical and experimental work has suggested that these defects cannot be the primary source of n-type conductivity since the O vacancy is likely to be a deep donor rather than a shallow donor and cation interstitials are likely to be unstable at room temperature [1.31-1.32]. Other native defects, defect complexes, and impurities also have been proposed as alternative sources of conductivity. Hydrogen impurities in particular have appeared as a strong candidate in recent studies [1.32].

Material	Structure type	Band-gap (eV)	references
ZnO	Wurtzile	3.1-3.6	[1.10], [1.26], [1.27], [1.33]
SnO_2	Rutile	3.6-4.6	[1.14], [1.27]
TiO_2	Rutile	3.0	[1.34],[1.35]
In_2O_3	Bixbyite	3.5-3.75	[1.36],[1.9],[1.27]
ITO	Bixbyite	3.5-4.6	[1.26],[1.27]
$SrTiO_3$	Perovskite	3.25	[1.37]

Table 1.1: Crystal structures and band gaps of a selection of transparent conducting oxides at room temperature.

Hydrogen has long been known to be an important impurity in conventional semiconductors. Hydrogen introduces electrical levels in the band gap and participates in a wide range of phenomena that affect the properties of the semiconductor. Since it is difficult to remove hydrogen from the growth environment, it is expected to be present in almost all semiconductors as an impurity. Perhaps hydrogen is best known for its ability to passivate shallow impurities and deep level defects [1.3, 1.38-1.43]. For example, H is intentionally introduced into the Si bulk to passivate defects and consequently improve the performance of solar cells made from low cost Si materials [1.44-1.46]. In most cases, hydrogen impurities reduce the conductivities introduced by other dopants [1.3, 1.32]. However, for metal oxides, hydrogen surprises us by acting as a shallow donor and causing conductivity by itself [1.47-1.51]. From the 1950's, it has been known that hydrogen impurities give rise to shallow donors in ZnO [1.47, 1.49, 1.52-1.55]. Similar effects caused by hydrogen, i.e. increased n-type conductivity, have also been reported for other conducting oxides; In_2O_3 [1.51], Ga_2O_3 [1.56]

and SnO_2 [1.21]. Mechanisms that explain the effect of hydrogen on metal oxides are different from those for other semiconductors.

Hydrogen, as an interstitial impurity in common semiconductors, is stable in either the +1 (donor) or the -1 (acceptor) charge states. The transition point where hydrogen changes from being a donor to an acceptor is called the H(+/-) transition level [1.10, 1.32]. The relative position of this level with respect to the Fermi level determines whether hydrogen forms a donor or an acceptor in the semiconductor. For conventional semiconductors, the transition level is near the middle of the band gap. Therefore, for Fermi levels close to the conduction band, i.e. n-type semiconductors, hydrogen acts as an acceptor. Conversely, for Fermi levels close to the valence band, i.e. p-type semiconductors, hydrogen acts as a donor. Interstitial hydrogen in these materials always counteracts the prevailing conductivity [1.3, 1.32, 1.57-1.58]. However, in the case ZnO, H+ is the stable charge state for all Fermi level positions, and hydrogen acts as a shallow donor, i.e. as a source of conductivity, even in n-type semiconductors [1.32, 1.59-1.62]. For this case, the H(+/-) transition level lies above the conduction band minimum. The H(+/-) transition levels determined by muon experiments [1.62] and by two separate theoretical calculations [1.48, 1.52] are shown in Fig. 1.5 in relation to band gaps of various metal oxides and other semiconductors [1.10]. Although there is a significant discrepancy between the determined transition level positions, all lie above the conduction band minimums of metal oxides.

Following the brief discussion above, two points should be emphasized: 1) transparent conducting metal oxides are an important class of semiconductors with unique properties and exceptional potential for technological applications, 2) the effect of impurities, particularly of

hydrogen, on the properties of transparent conducting oxides is critically important. However, much research remains to be done to advance these materials to their highest potential. This study contributed to progress in this field by investigating hydrogen-related impurities and their effects on the chemical and electrical properties of two important metal oxides; namely SnO_2 and TiO_2. The backbone of the study was built by experimental analysis. FTIR Spectroscopy which detects local vibrational modes due to impurities and absorption due to free carriers was the preferred experimental method and will be briefly introduced in the following sections.

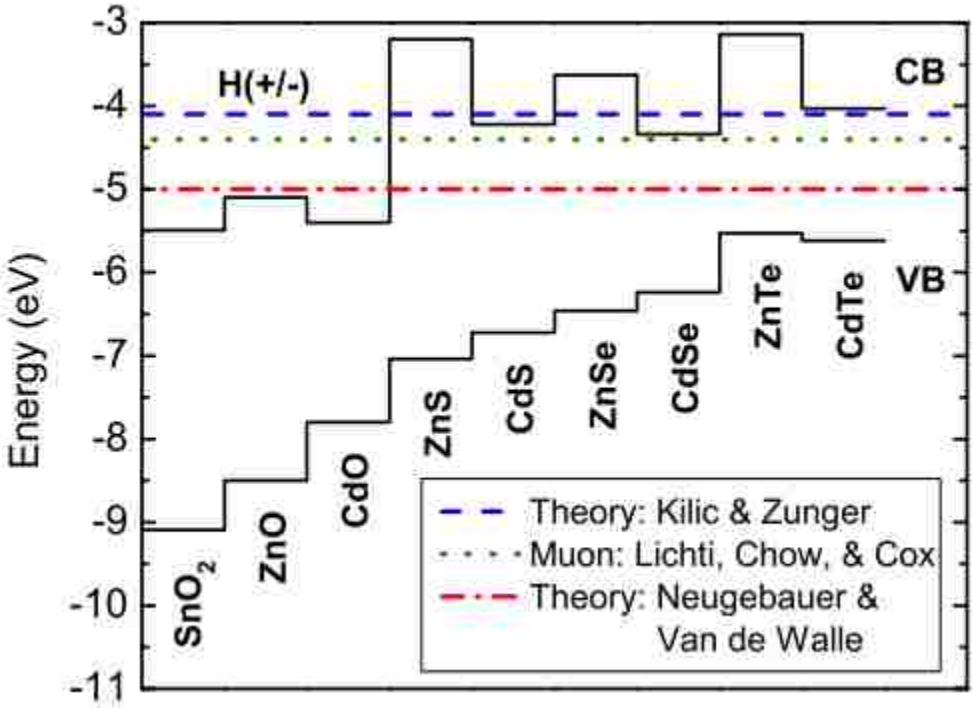

Fig. 1.5: Experimentally determined [1.62] and theoretically predicted [1.48, 1.59] H(+/-) transition level for various semiconductors in relation to their band gaps. [1.10]

REFERENCES:

[1.1]. A. Polimeni, M. Bissiri, M. Felici, M. Capizzi, I. A. Buyanova, W. M. Chen, H. P. Xin, and C. T. Tu, Phys. Rev. B, 67, 201303(R), (2003).

[1.2]. A. Polimeni, G. Baldassari H.v.H., M. Bissiri, M. Capizzi, A. Frova, M. Fischer, M. Reinhardt, and A. Forchel, Semicond. Sci. Tech. 17, 797, (2002).

[1.3]. Hydrogen in Material and Vacuum Systems, edited by G.R. Myneni and S. Chattopadhyay (AIP, New York, 2003)

[1.4]. A. Polimeni, G. Baldassari H.v.H., M. Bissiri, M. Capizzi, M. Fischer, M. Reinhardt, and A. Forchel, Phys. Rev. B. 63, 201304(R), (2001).

[1.5]. D. S. Ginley, C. Bright, MRS Bulletin, 25 (08), (2000).

[1.6]. B. G. Lewis, D. C. Paine, 25 (08), (2000).

[1.7]. P.P Edwards, A. Porch, M. O .Jones, D. V. Morgan, and R. M. Perks, Dalton Trans., (19) (2004).

[1.8]. R. G. Gordon, MRS Bulletin, 25 (08), (2000).

[1.9]. E. Fortunato, D. Gingley, H. Hosono, and D. C. Paine, MRS Bulletin , 32, (03), (2007),

[1.10]. M. D. McCluskey, C. Tarun, and S. T. Teklemichael, Journal of Materials Research, 27, 17,(2012).

[1.11]. A. N. Tiwari, G. Khrypunov, F. Kurdzesau, D. L. Batzner, A. Romeo, and H. Zogg, Prog. Photovoltaics Res. Appl., 12, (2004).

[1.12]. T. Minami, MRS Bulletin, 25 (08), (2000).

[1.13]. T. J. Coutts, J.D. Perkins, and D. S. Ginley, Electrochemical Society Proceedings, **99** (11), (1999).

[1.14]. M. Batzill and U. Diebold, Prog. Surf. Sci., **79**, (2005).

[1.15]. W. Göpel and K. D. Schierbaum, Sens. Actuators, B **26-27**, (1995).

[1.16]. A.E. Delahoy and S. Guo, *Transparent conducting oxides for photovoltaics. In Handbook of Photovoltaic Science and Engineering*, 2nd ed., edited by A. Lugue and S. Hegedus (John Willey & Sons Ltd, United Kingdom, 2011).

[1.17]. R. E. Presley, C. L. Munsee, C-H Park, D. Hong, J. F. Wager, and D. A. Keszler, J. Phys. D, **37**, (2004).

[1.18]. J. F. Wager, Science, **300**, (2003).

[1.19]. K. Ellmer, J. Phys. D: Appl. Phys., **34**, (2001).

[1.20]. U. Diebold, Surf. Sci. Rep., **48**, (2003).

[1.21]. W. M. Hlaing Oo. S. Tabatabaei, M. D. McCluskey, J. B. Varley, A. Janotti, and C. G. Van de Walle, Phys. Rev. B, **82**, 193201, (2010).

[1.22]. P. Ugliengo, D. Viterbo, and G. Chiari, Z. Kristallogr., **207**, 9 (1993).

[1.23]. E. H. Morales, Y. He, M. Vinnichenko, B. Delley, and U.Diebold, New J. of Phys., **10**, 125030, (2008).

[1.24]. H. Hosono, *Thin Solids Films*, **515**, 15, (2007).

[1.25]. B. J. Ingram, G. B. Gonzalez, D. R. Kammler, M. I. Bertoni, and T. O. Mason , Journal of Electroceramics, **13** ,1-3, (2004).

[1.26]. T. Minami, Semicond. Sci. Technol., **20**, (2005)

[1.27]. H. L. Hartnagel, A. L. Dawar, A. K. Jain, C. Jagadish, *Semiconducting Transparent Thin Films* (Institude of Physics, London, 1995).

[1.28]. *Transparent Electronics: From Synthesis to Applications*, edited by A. Facchetti and T. Marks (Wiley, New York, 2010).

[1.29]. C. Kiliç and A. Zunger, Phys. Rev. Lett. **88**,095501, (2002).

[1.30]. P. Ágoston, K. Albe, R. Nieminen, and M. Puska, Phys. Rev. Lett. **103**, 245501, (2009).

[1.31]. J. B. Varley, H. Peelaers, A. Janotti, and C. G. Van de Walle, J. of Phys.: Condens. Matter, **23**, 334212, (2011).

[1.32]. P. D. C. King, and T. D. Veal, J. of Phys.: Condens. Matter, **23**, 334214, (2011).

[1.33]. *Wide Bandgap Semiconductors: Fundemantal Properties and Modern Photonic and Electronic Devices*, edited by K. Takahashi, A. Yoshikawa, and A. Sandhu (Springer, New York, 2007).

[1.34]. M. Landmann, E. Rauls, and W. G. Schmidt, J. of Phys.: Condens. Mattter, 24,195503, (2012).

[1.35]. L. Kavan, M. Grätzel, S. E. Gilbert, C. Klemenz, and H. J. Scheel, J. Am. Chem. Soc., **118**, (1996).

[1.36]. T. Koida, H. Fujwara, and M. Kondo, Jpn. J. Appl. Phys., **46**, (2007).

[1.37]. K. van Benthem, c. Elsässer, and R.H. French, J. Appl. Phys., **90**, (2001).

[1.38]. S.J. Pearton, J.W. Corbett, and M. Stavola, *Hydrogen in Crystalline Semiconductors* (Springer-Verlag, Berlin, 1992).

[1.39]. *Hydrogen in Semiconductors,* edited by J.I. Pankove and N.M. Johnson (Academic, Boston, 1991).

[1.40]. *Hydrogen in Compound Semiconductors*, edited by S.J. Pearton (Trans Tech, Switzerland, 1994).

[1.41]. S.K. Estreicher, Mat. Sci. Eng. R **14**,319, (1995).

[1.42]. *Hydrogen in Semiconductors II*, edited by N.H. Nickel (Academic, San Diego, 1999).

[1.43]. J. Chevallier and B. Pajot, Interaction of Hydrogen with Impurities and Defects in Semiconductors, Solid-State Phenomena **85-86**, 203, (2002).

[1.44]. .H. Seager, D.S. Ginley, and J.D. Zook, Appl. Phys. Lett. **36**, 831, (1980).

[1.45]. J.I. Hanoka, C.H. Seager, D.J. Sharp, and J.K.G. Panitz, Appl. Phys. Lett. **42**, 618 (1983).

[1.46]. J. Szlufcik and F. Duerinckx, Solar Energy Materials and Solar Cells, **72**, 231 (2002).

[1.47]. C. G. Van de Walle, Phys. Rev. Lett., **85**, 1012, (2000).

[1.48]. Ç. Kiliç and A. Zunger, Appl. Phys. Lett. **81**, 73, (2002).

[1.49]. A. Janotti and C. G. Van de Walle, Nature Materials, **6**, 44, (2006).

[1.50]. A. K. Singh, A. Janotti, M. Scheffler, and C. G. Van de Walle, Phys. Rev. Lett., **101**, 055502, (2008).

[1.51]. S. Limpijumnong, P. Reunchan, A. Janotti and C. G. Van de Walle, Phys. Rev B, **80**, 193202, (2009).

[1.52]. E. Mollwo, Z. Phys. **138**, 478 (1954); G. Heiland, E. Mollwo, and F. Stöckman, in *Solid State Physics*, edited by F. Seitz and D. Turnbull (Academic Press, New York, 1959) Vol. 8, p. 193.

[1.53]. D. G. Thomas and J. J. Lander, J. Chem. Phys. **25**, 1136 (1956).

[1.54]. A. R. Hutson, Phys. Rev. **108**, 222 (1957).

[1.55]. E. V. Lavrov, F. Herklotz, and J. Weber, Phys. Rev. B **79**, 165210 (2009).

[1.56]. J. B. Varley, J. R. Weber, A. Jonetti, and C. G. Van de Walle, Appl. Phys. Lett., **97**, 142106, (2010).

[1.57]. J. Neugebauer, and C. G. Van de Walle, *in Hydrogen in Semiconductors II, Semiconductors and Semimetals,* Vol. 61, edited by N. H. Nickel (Academic Press, Boston, 1999).

[1.58]. C. G. Van de Walle, and N. M. Johnson, in Gallium Nitride (GaN) II, *Semiconductors and Semimetals*, Vol. 57, edited by J. I. Pankove and T. D. Moustakas (Academic Press, Boston, 1998).

[1.59]. C. G. Van de Walle, and J. Neugebauer, Nature, **423**, (2003).

[1.60]. C. G. Van de Walle, Phys. Rev. Lett., **85**, (2000).

[1.61]. A. Janotti, and C. G. Van de Walle, Nature Mater., **6**, (2007).

[1.62]. R. L. Lichti, K. H. Chow, and S. F. J. Fox, Phys. Rev. Lett., **101**, 136403, (2008).

Chapter 2

Experimental Methods: Infrared Spectroscopy

2.1 Local Vibrational Modes (LVMs)

When an impurity atom that is lighter than the host atoms is present in a crystal, new vibrational modes with a higher frequency than the host-crystal's vibrational modes way appear. Vibrational spectroscopy can be used effectively to probe and identify defects containing light impurities by detecting these additional vibrational modes in the host crystal's spectra.

The effect of a light impurity in an otherwise perfect crystal on the vibratonal spectrum can be studied with a simple model given by Barker and Sievers [2.1] for GaP. This is a one-dimensional, linear diatomic chain with 48 atoms as shown in Fig. 2.1. Assuming harmonic vibrations, 24 acoustic and 24 optic vibrational modes for this perfect chain model were calculated, and the dispersion curves are presented in Fig. 2.1. A selection of the modes is illustrated in the figure by using vertical displacements for clarity, although the motions are in the longitudinal direction in reality. For instance, for mode 1, the zero frequency mode, the vibration of all atoms are in phase with each other, while for the highest frequency optic mode at the zone center, each atom vibrates against its neighbor. When an impurity atom with a mass m' that is smaller than the masses of both crystal host atoms is substituted into the chain, a new vibrational mode with a higher frequency appears. In addition to its high frequency, this new mode has also another distinctive property; that is, it is localized at the

impurity atom. Since the high frequency of this mode cannot be followed by the heavier atoms in the crystal, the wave does not propagate, and only a few neighbor atoms participate in the motion. Therefore, the high frequency vibrational mode is called a local vibrational mode (LVM). A selection of the modes calculated with an impurity in the chain is shown in Fig. 2.2 (a). The local vibrational mode due to the impurity is given as Mode 48, and as clearly seen, its frequency is higher than that of the other modes and only the atoms near the impurity are in motion. As the mass of the impurity atom is decreased, the frequency of the LVM increases and the mode becomes more localized. This is illustrated in Fig. 2.2 (b). In the calculations of Barker and Sievers, the force constant was assumed to be unchanged with or without the impurity.

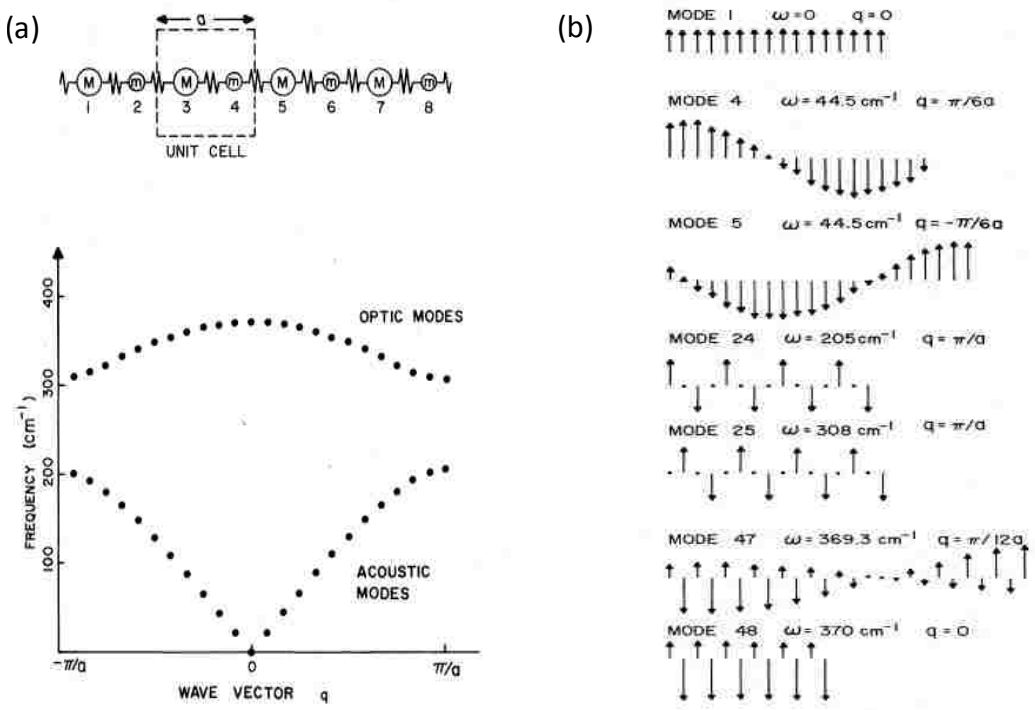

Fig. 2.1: (a) Linear chain model and dispersion curves for a 48 atom chain model of GaP. (b) A selection of the mode's eigenvectors for the 48 atom chain model of GaP [2.1-2.2].

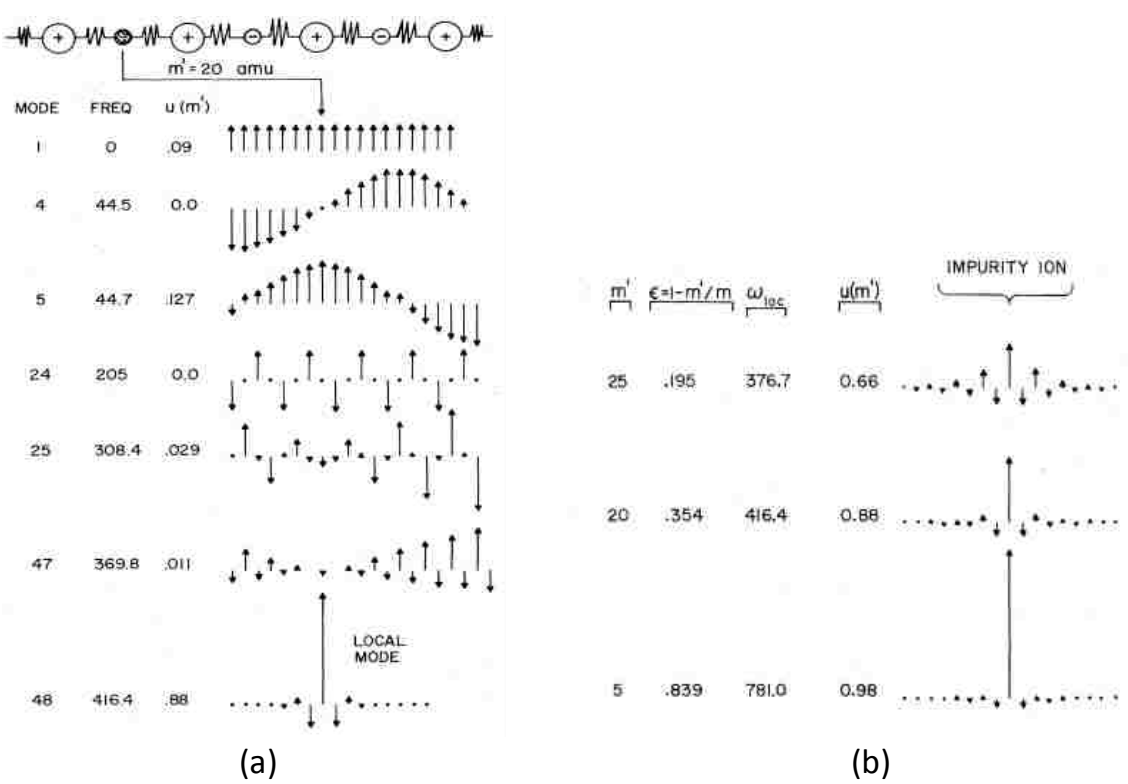

Fig. 2.2: (a) A selection of the vibrational eigenvectors for the 48 atom chain model of GaP containing a light-element impurity which is substituted for the lighter atom in the chain. Mode 48 represents the LVM with the highest frequency. (b) The eigenvectors for the LVM with different impurity mass. The highest frequency mode becomes more localized with the decreasing mass of the impurity [2.1-2.2].

The angular frequency of the LVM due to a light impurity atom (with a mass m') placed into a lattice where the nearest neighbor atom has a mass of M is given by the following commonly used equation [2.3-2.4]:

$$\omega^2 = k\left(\frac{1}{m'} + \frac{1}{XM}\right). \tag{2.1}$$

Here X is a parameter of order 1 [2.5] and k is the force constant between the impurity atom and its neighbor. Since isotopic substitutions for both the impurity atom and the nearest neighbor host atom can cause frequency shifts in the absorption lines, fine structures detected by high resolution measurements can be used to analyze the defect structure and determine the neighboring atoms. The power of vibrational spectroscopy for detecting and identifying impurity-related structures is well illustrated by a study previously performed in our group by Shi *et al*. [2.6]. This study is also relevant to this work because it investigates properties of impurities in a transparent conducting oxide, namely ZnO.

Li impurities are known to substitute for Zn in hydrothermally grown ZnO where a Li-containing solvent is used. Moreover, the strong infrared line at 3577.3 cm^{-1} in the spectrum of hydrogen-containing ZnO (Fig. 2.3) is associated with a OH-Li complex. In addition to this strong line, there are other LVMs that give rise to weak absorption lines in the spectrum. In Fig. 2.3, the spectrum for deuterium-containing ZnO is shown for comparison. The spectrum of the deuterium doped sample shows clearly a frequency shifted partner for the O-H line in the hydrogen treated sample. The strong line due to OD-Li has a frequency of 2644.5 cm^{-1}, about 1.35 times smaller than the frequency for the OH-Li line. If the ratio of the two frequencies is calculated using Eqn 2.1 as

$$\frac{\omega_H}{\omega_D} = \left(\frac{k\left(\frac{1}{m_H}+\frac{1}{XM}\right)}{k\left(\frac{1}{m_D}+\frac{1}{XM}\right)} \right)^{1/2} \approx \sqrt{2}\left(1 - \frac{m_H}{XM}\right), \qquad (2.2)$$

the expected shift is close to $\sqrt{2}$, consistent with the experimental observation.

In addition to the shifts due to the isotopes of hydrogen, the effect of the oxygen isotopes, i.e., ^{17}O and ^{18}O with natural abundances of 0.04% and 0.20%, respectively, can also be observed in both spectra (Fig. 2.3). While the strong absorption line at 3577.3 cm^{-1} (2644.5 cm^{-1}) correspond to the OH-Li (OD-Li) complex with ^{16}O, the weaker absorption lines at 3566.6 cm^{-1} (2629.2 cm^{-1}) and 3571.7 cm^{-1} (2636.4 cm^{-1}) correspond to the same complex with ^{18}O and ^{17}O, respectively. The intensities of these lines are in good agreement with the natural abundances of these isotopes due to the very useful fact that the concentration of the defect is proportional to the intensity of the absorption line.

More interesting, Li has also two isotopes, ^{6}Li and ^{7}Li, with abundances 7.5% and 92.5%, respectively, which also affect the spectra. The fine structure due to the two Li isotopes could be resolved for the OD-Li line near 2644.5 cm^{-1} and is shown in Fig. 2.4. Two separate lines at 2644.52 cm^{-1} and 2644.69 cm^{-1} with relative intensities (0.93:0.07), in very good agreement with the natural abundances of the Li isotopes, were discovered with high resolution measurements. A similar observation could not be made for the hydrogen-treated sample (Fig. 2.4) for two reasons. The OD-Li infrared lines are narrower than the OH-Li lines, and the isotope shift due to Li in OD-Li is larger than that in OH-Li. In general, H-containing defects typically have broader IR lines than the corresponding D-containing defects, therefore study of D-treated samples can give information about hydrogen-related defects that cannot be observed in H-treated samples.

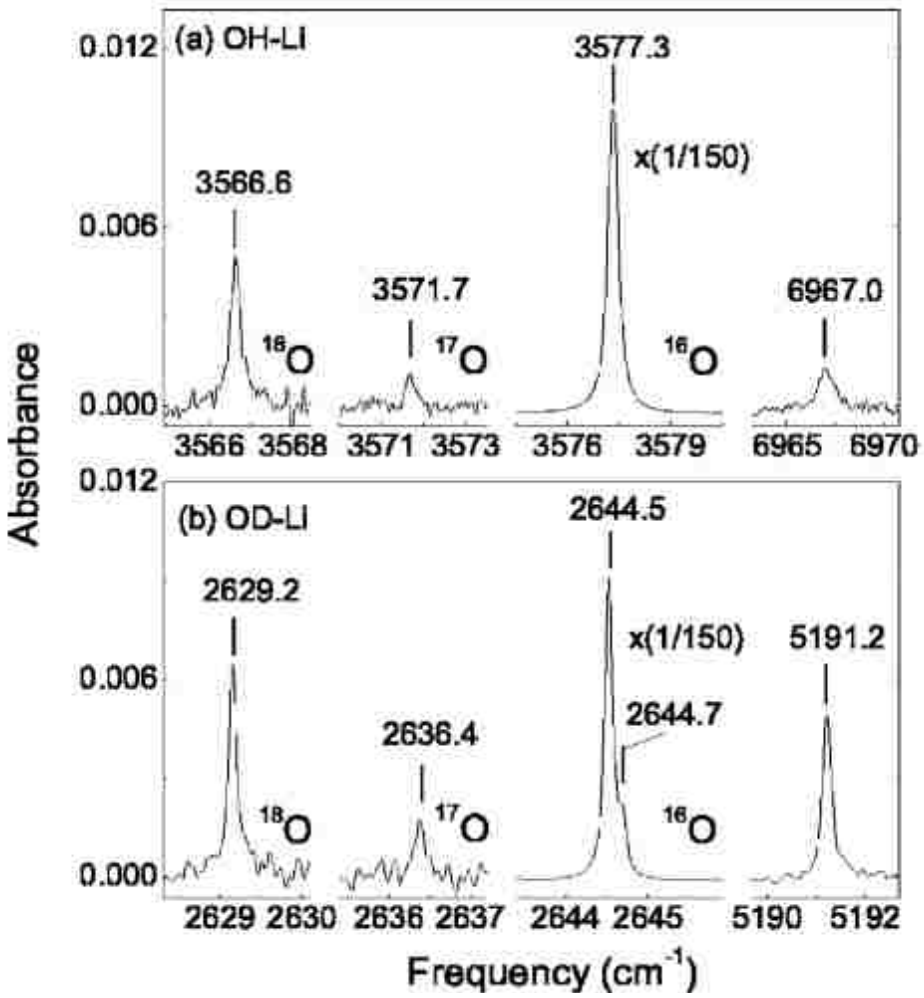

Fig. 2.3: IR absorption spectra (4.2 K) of hydrogen- (a) and deuterium- (b) treated ZnO samples that focus on the OH-Li and OD-Li absorption lines with the three oxygen isotopes ^{16}O,^{17}O, ^{18}O [2.6].

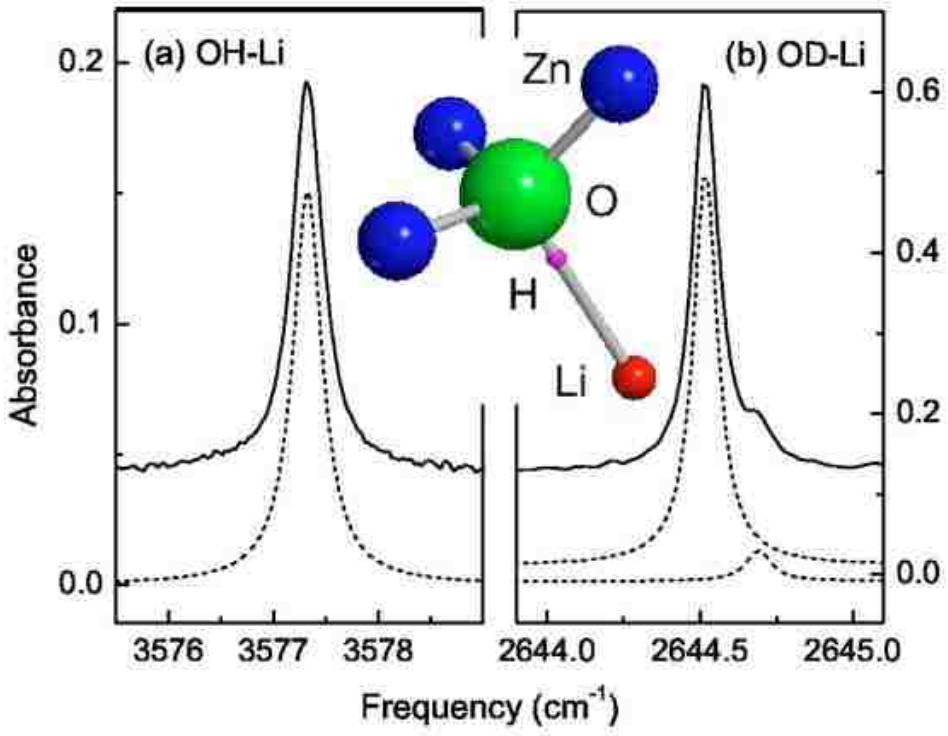

Fig. 2.4: IR absorption spectra of hydrogen- (a) and deuterium- (b) treated ZnO samples that focus on the OH-Li and OD-Li absorption lines with H or D bound to ^{16}O [2.6].

The use of polarization properties provides another strategy for analyzing defect structures with vibrational spectroscopy. A vibrational mode will be excited only if the incident light has an electric vector component in the direction of the oscillating dipole moment. Therefore, the use of polarized light can give important information about the orientations of the bonds in the defect structure. This perspective will be utilized during the course of this study.

Finally, the relationship between the strength of the absorption lines and the defect concentration should be mentioned. The integrated absorption coefficient (LVM intensity) for

a local mode is directly proportional to the defect concentration as is shown by the following equation,

$$\int \alpha(\sigma) d\sigma = \frac{\pi q^2 N}{m\eta c^2}. \tag{2.3}$$

Here N is the defect concentration per cm^{-3}, q is an effective charge for the mode, σ is the wavenumber, and η is the refractive index of the host. Eq. 2.3 can alternatively be expressed as

$$N = A \int \alpha(\sigma) d\sigma \tag{2.4}$$

where A is a calibration factor that can be determined from other methods such as secondary ion mass spectrometry (SIMS) or Hall effect [2.7].

The signal-to-noise ratio for a vibrational spectroscopy measurement depends on the concentration of the defect. In other words, there is a minimum defect concentration that can be detected by an absorption measurement. Although this minimum value is dependent on several parameters, roughly a concentration of 10^{18} cm^{-3} in a 1 μm thick layer, or 10^{14} cm^{-3} in 1 cm thick sample, can be detected [2.2]. For higher frequency LVMs, such as hydrogen-related modes, a lower concentration, near 10^{17} cm^{-3} in a 1 μm thick layer, is the detection limit [2.2].

2.2 Free Carrier Absorption

Free carriers are electrons (holes) that are free to move within the conduction (valence) band. These carriers experience no restoring force when displaced by an electromagnetic wave. Free carrier absorption occurs when an incident photon excites the

electron to a higher energy state within the same band and is proportional to the carrier concentration. The phenomenon of free carrier absorption is critically important for this work for two main reasons: 1) A high concentration of free carriers give rises to broad continuum absorption in the IR frequency range, which is of interest for vibrational spectroscopy of doped semiconductors [2.2], and 2) a high concentrations of free carriers can cause high electrical conductivity and reduced visible transparency in metal oxides [2.8]. The presence of high free carrier densities in doped metal oxides is actually desired to obtain the required electrical conductivity, and the wide band-gap structure of these materials prevents interband excitations of electrons and hole by visible light to provide an optically transparent material at the same time. However, the free carrier absorption which occurs by the excitation of free electrons in the conduction band to higher states in the same band is also a limit to the optical transparency. These transitions are generally caused by incident photons that have substantially lower energy than the band-gap energy, and they occur in an indirect fashion which involves changes in both energy and momentum. Fig. 2.5 shows a schematic that explains the free carrier transition in a doped semiconductor. A free electron in the conduction band that is below the Fermi level is excited to a higher energy above the Fermi level by an incident photon. Photons have only very small momentum compared to electrons and some other mechanisms such as phonon scattering or scattering from ionized impurities must also come into play to conserve momentum. This corresponds to the horizontal transition shown in Fig. 2.5, and the electron arrives in an empty state above the Fermi level at the end of the process [2.9].

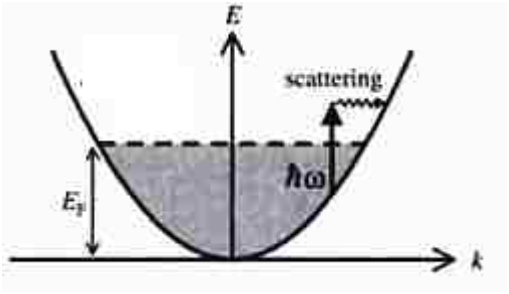

Fig. 2.5: Free carrier transition in a doped semiconductor [2.9].

Free carrier absorption can be modeled using the Drude theory which was originally used for the modeling of free electrons in plasmas. The theory considers the oscillations of the free electron induced by the electric vector of an electromagnetic field and finds the free carrier absorption coefficient to be [2.9].

$$\alpha_{FC} = \frac{nw_p^2}{cw^2\tau}. \tag{2.5}$$

Here, n is the refractive index, τ is the momentum scattering time, and w_p is the plasma frequency given by,

$$w_p{}^2 = \frac{Ne^2}{n^2\epsilon_0 m^*}. \tag{2.6}$$

Here, N corresponds to the carrier density and m* is the effective mass. The plasma frequency is important in transparent metal oxide device design because it divides the optical properties of the material. At frequencies below w_p, the material is highly reflective, whereas the material can transmit or absorb light at frequencies above w_p. The plasma frequency generally falls in the near-infrared region for most of the metal oxides, and therefore transparency is permitted

in the visible range unless a high free-carrier density introduces substantial absorption. It should be noted that the plasma frequency is proportional to the square root of the free carrier concentration, as seen in Eq. 2.6, and a high carrier density can shift this optical limit to higher frequencies into the visible range. Combining Eqs. 2.5 and 2.6 yields

$$\alpha_{FC} = \frac{Ne^2}{nc\tau\epsilon_0 m^* w^2} . \tag{2.7}$$

There is a direct proportionality of the free carrier absorption to the carrier density as seen in Eq. 2.7. The free carrier absorption is also proportional to ω^{-2}, meaning that the absorption is more pronounced at lower frequencies, particularly in the infrared region where most of our defect spectroscopy studies are done. Fig. 2.6 shows a comparison of the transmission spectra of a heavily n-doped and an undoped Ge sample [2.10] . The effect of free carrier absorption is apparent in the long wavelength region.

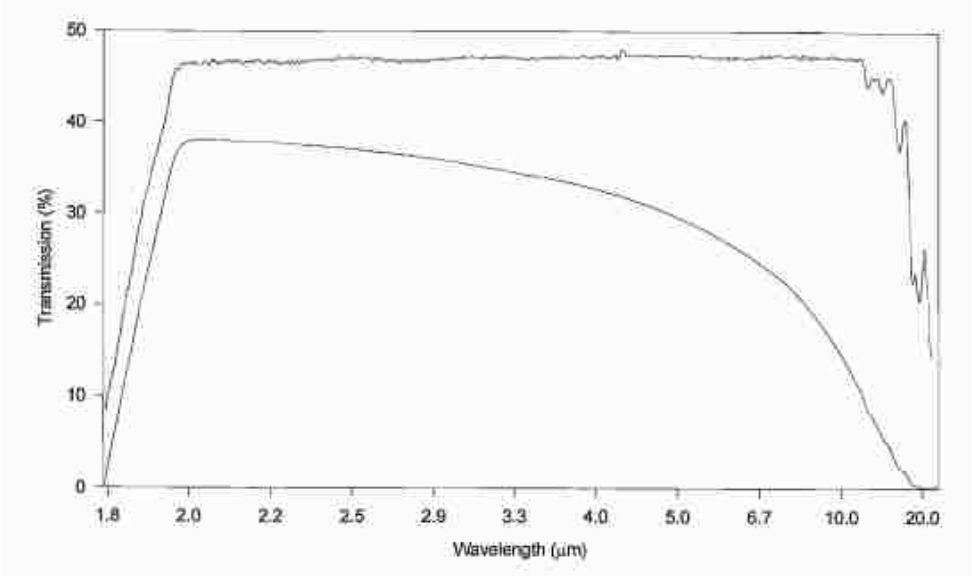

Fig. 2.6: Transmission spectra of an undoped germanium sample (upper) and a heavily n-doped germanium sample (lower) [2.10].

In conclusion, a good understanding of free carrier absorption in transparent metal oxides is useful for determining the sources and level of conductivity and also for defining the limits of optical transparency. The free carrier absorption will be frequently revisited in the following chapters as we investigate the relationship between the H-related shallow donors, and the free carrier concentration caused by these defects.

2.3 Measurement Technique

Infrared spectroscopy was used to detect and identify the defects of interest in this study by employing a Bomem DA 3.16 FTIR spectrometer. The FTIR spectrometer provides two major advantages over traditional prism or diffraction spectrometers; 1) a higher signal-to-noise ratio, 2) capability of obtaining a spectrum with broad frequency range in a single

measurement. While the former enables higher resolution measurements, the latter is especially important for time efficiency and is possible through the use of a Michelson interferometer.

The Michelson interferometer shown in Fig. 2.7 is an optical component of a FTIR spectrometer and works as follows. A light beam from an infrared source reaches the beam splitter and is divided into two equal components as shown in the figure. The first component travels towards a fixed mirror and is reflected back to the beam splitter. The second component of the beam, on the other hand, is directed towards a movable mirror and is reflected back to the beam splitter. The two beam components interfere with each other at the beam splitter and the re-combined beam moves towards the sample. The light transmitted from the sample is then collected by a detector.

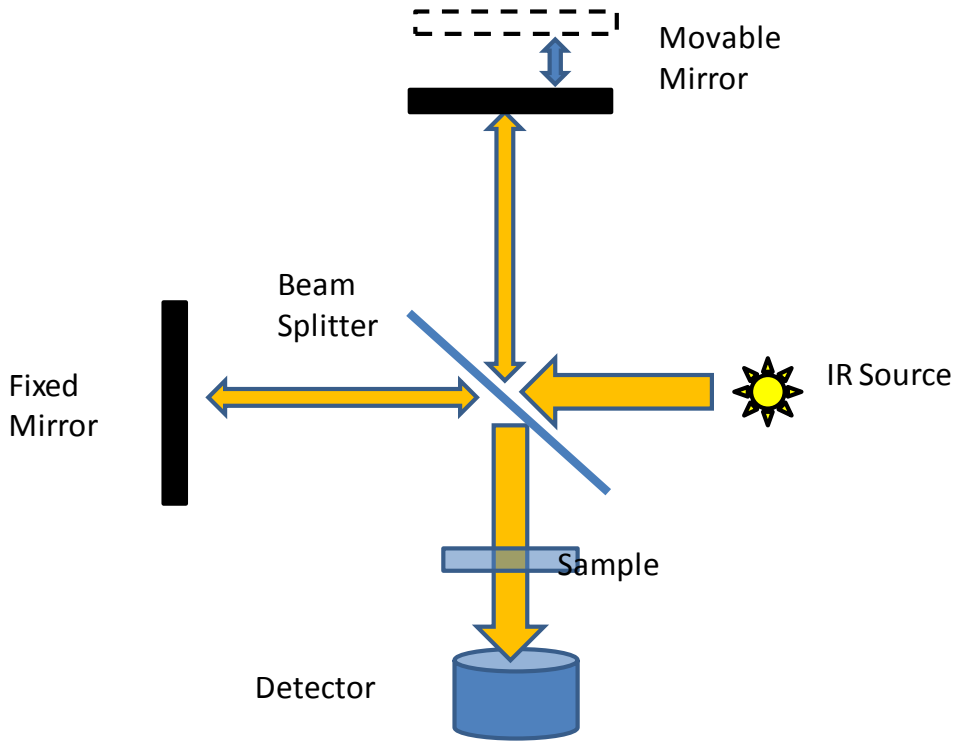

Fig. 2.7: Optical configuration of a Michelson interferometer.

The Michelson interferometer enables study of the absorption of light at different frequencies in a single measurement by the following principle. First, consider a monochromatic light source and the case with no sample. The intensity of the output from the beam splitter is determined by the position of the moving mirror, or in other words, the optical path difference between the two components of the split beam. For example, if the optical paths defined by the fixed and movable mirrors are the same or differ by an integer multiple of the light wavelength, the components interfere constructively to yield a maximum detector signal. Conversely, when the movable mirror is positioned such that the optical path difference is an integer multiple of half of a wavelength, the components interfere destructively and the detector records a minimum signal. When the movable mirror scans with a constant speed,

the detector records a cosine wave due to a continuous cycle of constructive and destructive interferences (Fig. 2.8 (a)). The intensity recorded by the detector is given by

$$I(x) = \frac{B}{2}[1 + \cos(2\pi v x)] \tag{2.8}$$

Here B is the intensity of the incoming light, *x* is the optical path difference, and *v* is the frequency. The Fourier transform of the cosine wave gives the spectrum, in this case, a single sharp line.

If a slightly different, second frequency is also introduced into the interferometer, the detector recording turns into a beating pattern as seen in (b). For polychromatic sources that include many frequencies, the interferogram recorded by the detector is the sum of many cosine waves with different amplitudes and periods and will take a more complicated shape, as shown in Fig. 2.8 (c). Again, the Fourier transform reveals the spectrum of the incident beam.

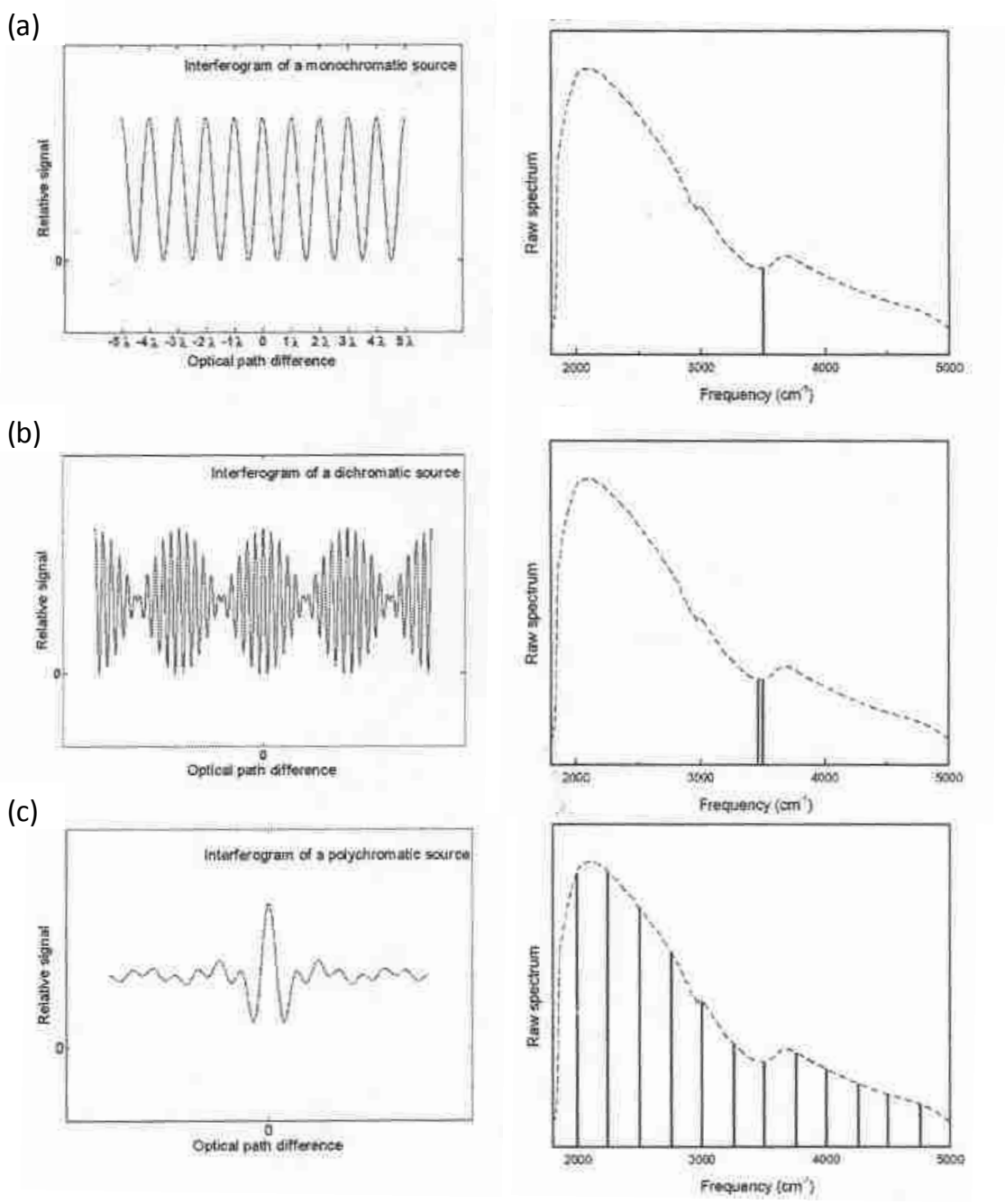

Fig. 2.8: Interferograms (left) and corresponding Fourier transformed spectra (right) for (a) a single frequency, (b) two close frequencies, and (c) a number of frequencies [2.11].

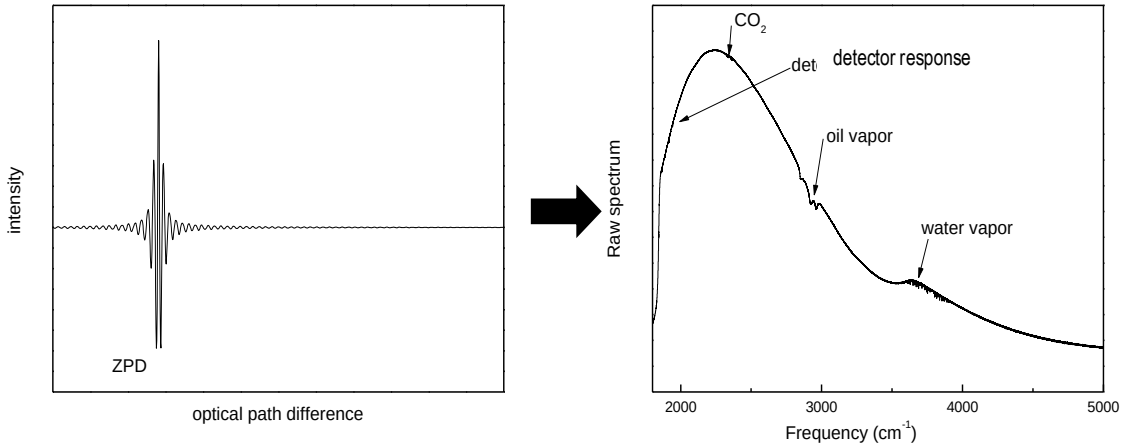

Fig. 2.9: Interferogram (left) and corresponding Fourier transform spectrum (right) measured in our equipment with no samples.

In FTIR spectrometers, an IR light with a continuum of frequencies is used as a source. For this case, the interferogram which is shown in Fig. 2.9 is mathematically expressed by an integral

$$I(x) = \frac{B(v)}{2}\int_{-\infty}^{\infty}[1 + \cos(2\pi vx)]dv \tag{1.9}$$

The largest signal in the interferogram seen in Fig. 2.9 corresponds to the constructive interference of all the light coming from the source, which occurs only at the zero path difference (ZPD) position. Immediately around the ZPD location, the signal quickly decreases to a steady state value and little information can be directly obtained by looking at the interferogram. However, a Fourier Transform can be applied to obtain the original spectrum which contains information about the light source, optical elements of the equipment and the detector. The transform can be written as

$$B(v) = \frac{1}{2}\int_{-\infty}^{\infty}[I(x)\cos(2\pi vx)dx] \tag{2.10}$$

The raw spectrum, obtained by the transform of the interferogram shown in Fig. 2.9, is given in the same figure, next to the interferogram. By using a source of continuous frequencies, a continuous broad spectrum of frequencies is obtained in a single measurement. Up to this point, no sample was considered in the system, so that the overall shape of the spectrum corresponded to the response of elements of the equipment, such as the photodetector. Therefore, it is nearly the same for every measurement using the same set-up. Environmental effects such as oil, CO_2 and water vapor present in the system can slightly modify the shape of the spectrum, as shown in Fig. 2.9.

Up to this point, no sample was considered in the measurement system and the response of the equipment was discussed. When a sample is placed and the spectrum with the sample is obtained, it can be compared with the reference spectrum, i.e. the spectrum corresponding to the "no-sample" condition, in order to cancel out the equipment response and the effects of background features. Therefore, in the ideal situation, the net spectrum corresponds solely to the chemical structure of the sample. A reference and a sample spectrum are given together in Fig. 2.10. The sample spectrum can then be divided by the reference spectrum to find the transmittance of the sample. More often, the absorbance is used, and it can be determined by taking the $-\log_{10}$ of the transmittance. The absorbance spectrum of the sample is shown in Fig. 2.10 and the peaks corresponding to some defects in the sample are shown in more detail in the inset. These peaks, seen at the interval 3150 cm^{-1} - 3400 cm^{-1}, actually correspond to O-H related defects in SnO_2, which will be an important subject of interest and treated in detail in Chapter 3.

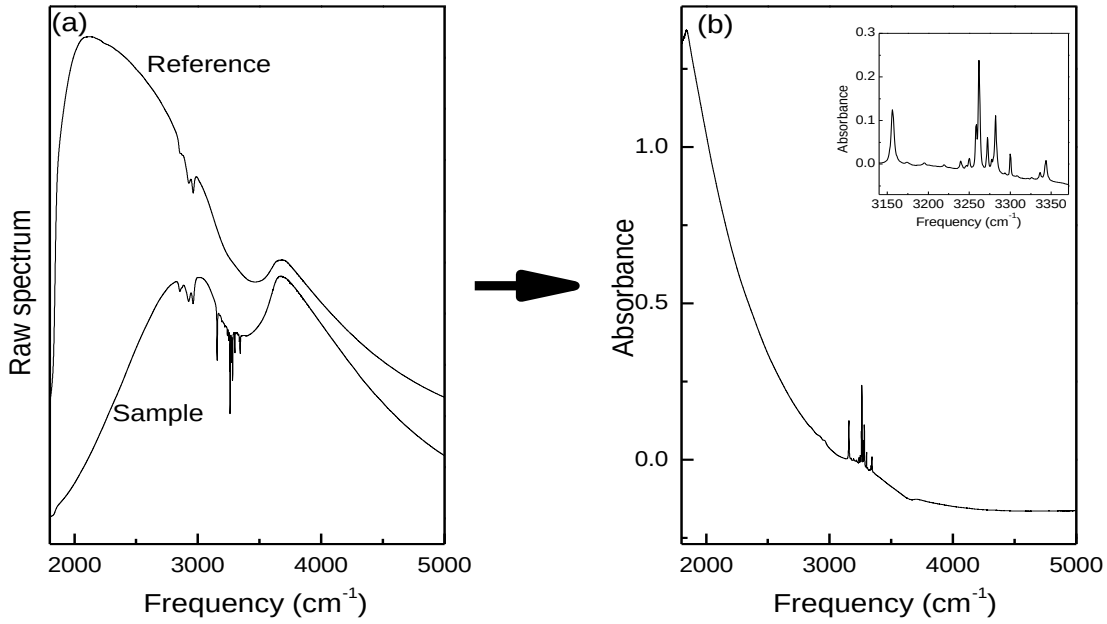

Fig. 2.10: (a) Spectrum obtained from a sample in comparison to a "no-sample" reference measurement, (b) absorption spectrum of the sample (hydrogen-treated SnO_2), inset spectrum focusing on the O-H absorption lines.

2.4 Instrumentation

Measurements in this study were performed with a Bomem DA 3.16 FTIR spectrometer. The spectrometer is controlled by a computer via a PCDA3INT VAX interface and the data acquisition is performed by the use of the Bomem PCDA data acquisition software, which allows the user to select and modify experimental parameters and collect data. The Fast Fourier Transform is performed with the interface computer and the transformed data is sent back to the computer for analysis with the Bomem GRAMs/32 software. Peak Fit v4 and Origin 8 are the other software packages used in this study for data analysis, plotting and curve fitting purposes.

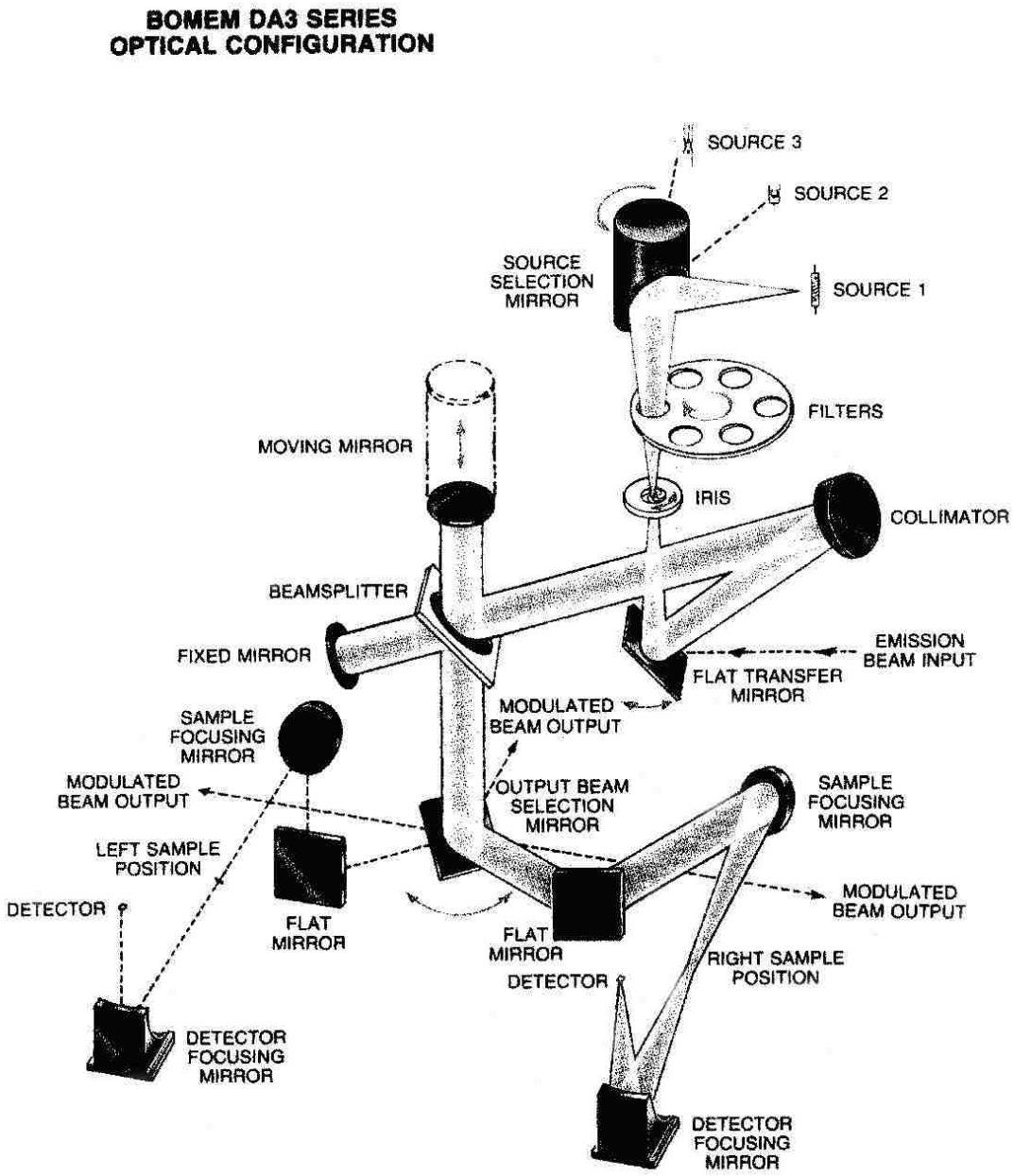

Fig. 2.11: The optical configuration of Bomem DA 3.16 spectrometer [2.12].

The schematic configuration of the Bomem spectrometer is shown in Fig. 2.11. A silicon carbide globar (mid-IR) and a quartz halogen lamp (near IR-visible) are the two available light sources which cover different ranges of frequencies. In this study, we mainly used the silicon carbide globar source since the mid-IR frequency range was of interest for our studies. The light from the source passes through a six-position rotary filter and an iris which has different diameter settings between 0.5 - 10 mm. PCDA software is used to select the desired aperture and filter type and to communicate with the set-up. Then the light is reflected from a flat mirror and transferred to the beam splitter. Two types of beam splitters were available to cover different frequency ranges; a KBr beam splitter coated with Ge/ZnSe for the 450 cm^{-1} - 5000 cm^{-1} range and a quartz beam splitter coated with TiO_2 for the 4000 cm^{-1} -27000 cm^{-1} range. The 10 cm diameter KBr beam splitter was primarily used in this study. As discussed previously, the light is split by the beam splitter and the components are re-combined after being reflected back either from a fixed or a moving mirror. Then the light is focused on the sample, a set of off-axis paraboloid mirrors, and finally to the photodetector. Liquid N_2-cooled InSb detectors which measure IR absorption in the range 1800 cm^{-1} - 8000 cm^{-1} were used in the experiments. Two other types of detectors, namely a HgCdTe (MCT) photodiode and a Si bolometer, were available to cover different frequency ranges; 800-5000 cm^{-1} and 350-2500 cm^{-1} respectively.

Most of the infrared absorption measurements were performed at liquid He temperatures in order to reduce the thermal vibration of the host crystal lattice. The sample was placed inside one of two available cryostats. The first one is an Air Products Heli-Tran cryostat equipped with either a CaF_2 or CsI window [2.13]. This is a continuous flow, cold-finger cryostat and is easy to operate. This cryostat was used in our studies of SnO_2. The

second cryostat is an Oxford CF1204 model, which is also a continuous flow cryostat that cools the sample space with He exchange gas. A schematic of this cryostat is given in Fig. 2.12. This cryostat provides a design that separates the vacuum layer and the sample chamber, which speeds up the transition between consecutive experiments using different samples. The cryostat has a six window configuration which includes 2 outer vacuum case windows and 2 inner-sample cold windows. The remaining 2 are the radiation shield windows between the outer vacuum and inner sample windows and are cooled by thermal contact with the cold shield. Therefore, the temperature in the sample chamber is protected from the effect of black-body radiation from the room temperature environment. The major advantage of this cryostat for our studies is its very good temperature stability (within ± 0.1 K [2.14]). So this cryostat was preferred especially for our TiO_2 experiments which involve repeated measurements with temperature steps as small as 0.5 K. The accuracy and stability of the temperature control were the key factors for this set of experiments.

The vacuum in IR spectroscopy is needed mainly to minimize the effects of background features, such as the absorption of light by water vapor, CO_2 and oil. Separate pumps are used for generating the vacuum in the spectrometer (a mechanical pump) and in the cryostat (a turbo pump). Liquid nitrogen cold traps inside the spectrometer and also on the turbo pump vacuum line are used to further reduce the absorption arising from water vapor, oil, and CO_2.

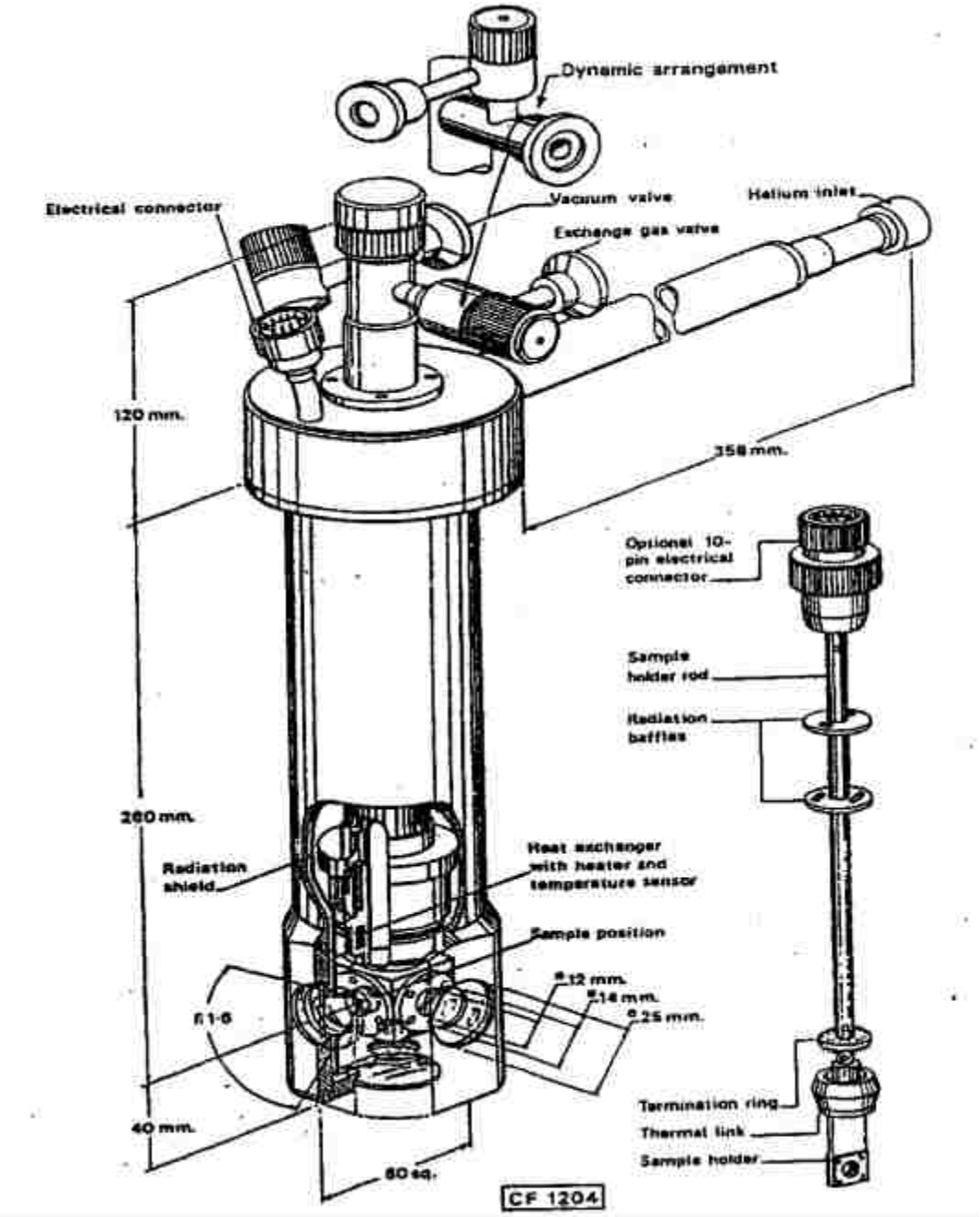

Fig. 2.12: Illustration of Oxford CF1204 cryostat [2.14].

REFERENCES:

[2.1]. S. Barker, and A. J. Sievers, Rev. Mod. Phys., **47**, S1, (1975).

[2.2]. *Identification of Defects in Semiconductors, Semiconductors and Semimetals,* Vol. 51B, edited by M. Stavola (Academic Press, San Diego, 1999).

[2.3]. R. S. Leigh, R. C. Newman, M. J. L. Sangster, B. R. Davidson, M. J. Ashwin, and D. A. Robbie, Semicond. Sci. Techol., **9**, 1054, (1994).

[2.4]. R. S. Leigh, and R. C. Newman, Semicond. Sci. Techol., **3**, 84, (1988).

[2.5]. R. C. Newman, *Infrared Studies of Crystal Defects* (Taylor and Francis, London, 1973).

[2.6]. G. A. Shi, M. Stavola, and W. B. Fowler, Phys. Rev. B., **73**, 081201(R), (2006).

[2.7]. D. M. Kozuch, M. Stavola, S. J. Pearton, C. R. Abernathy, and W. S. Hobson, J. Appl. Phys., **73**, 3716, (1993).

[2.8]. H. Peelaers, E. Kioupakis, and C. G. Van De Walle, Appl. Phys. Lett., **100**, 011914, (2012).

[2.9]. M. Fox, *Optical Properties of Solids* (Oxford University Press, New York, 2001).

[2.10]. P. D. Fairley, *Novel solid state modulator for the infrared: the germanium chopper*, University of Southampton, (2000).

[2.11]. G. A. Shi, *Physics of H in ZnO and H_2 in Si from Vibrational Spectroscopy*, Lehigh University, (2006).

[2.12]. Bomem Spectrometer System and Software User's Manual, (Bomem Inc., 1993).

[2.13]. Liquid Transfer Heli-tran Operating Manual, (Air Products and Chemicals Inc.).

[2.14]. Instruction Manual for Continuous Flow Cryostat CF1204 (Oxford Instruments Limited, England, 1988).

Chapter 3

FTIR Spectroscopy of O-H and O-D Centers in SnO_2

3.1 Introduction

Tin oxide (SnO_2) is one of the conducting metal oxides that shows great potential for use as a large gap semiconductor. It has a band gap of 3.6 eV [3.1] and a rutile structure as shown in Fig. 3.1. For this structure, there are six neighboring oxygen atoms for each Sn atom, and also each oxygen forms a plane with its three Sn neighbors. The c-axis of the structure is normal to one of the O-Sn bonds, while the other two bonds make angles of 39.3° and 140.7° with the c-axis [3.2]. SnO_2 has been used in many technological applications for many years, for example as a transparent conductor for various electronic devices [3.1, 3.3-3.4], a oxidation catalyst [3.1] and a gas sensor [3.5-3.6].

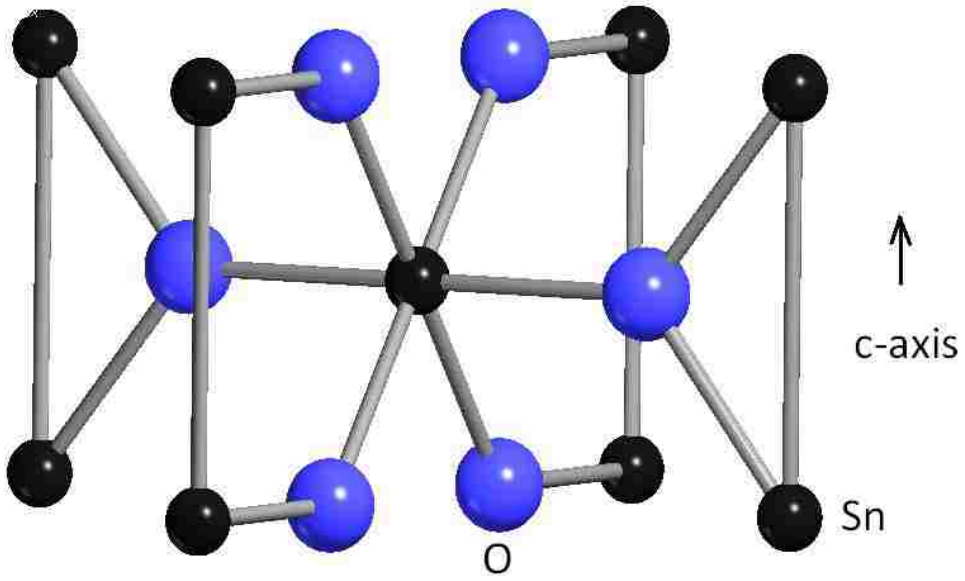

Fig. 3.1: Rutile lattice structure of SnO_2 [3.7].

The source of conductivity in SnO_2 and other similar transparent metal oxides is an active research subject because understanding these sources of conductivity would lead to optimal benefits from this emerging class of semiconductors. Previously, native defects such as oxygen vacancies and cation interstitials have been suggested to be the source of n-type conductivity [3.8-3.11]. However, recently, both theory [3.12-3.16] and experiments [3.17-3.19] have suggested that hydrogen within these crystals may act as sources of electrical conductivity. For example, hydrogen is known to give rise to shallow donors and is proposed to be an important source of n-type conductivity in ZnO. Interstitial H (H_i) and H at an O vacancy (H_O) both have been predicted to be shallow donors in ZnO [3.12-3.13, 3.17, 3.19-3.20].

Recent theory suggests that a similar situation may also exist for SnO_2. Theory predicts that native defects are unlikely to be the major source of conductivity [3.15] and that hydrogen defects can act as shallow donors. Also similar to ZnO, both H_i and H_O have been suggested to be donors in SnO_2. Illustrations of the H_i and H_O configurations in SnO_2 are shown in Fig. 3.2 (a) and (b), respectively. Near room temperature, H_i in SnO_2 is predicted to be thermally unstable [3.15], similar to H_i in ZnO [3.20] which has an O-H vibrational line at 3611 cm^{-1} [3.21]. On the other hand, H_O is more thermally stable as predicted for SnO_2 [3.15] and as shown for ZnO [3.13, 3.20]. Clearly, there is a strong analogy between the hydrogen behavior in ZnO and SnO_2. In this chapter, IR vibrational spectroscopy will be used to investigate hydrogen related defects and their effects on the electrical properties of SnO_2. Our experimental strategy is based on previous findings for ZnO and also the theoretical results and limited experimental data for SnO_2.

Thermal treatments in different ambients are known to have strong effects on the behavior of hydrogen- related defects. For instance, annealing SnO_2 in a hydrogen-containing ambient gives rise to strong n-type conductivity and generates a number of O-H absorption lines [3.22-3.26]. A recent study confirmed the increased conductivity upon annealing SnO_2 in hydrogen and assigned the vibrational lines that were generated to H_i and two different complexes of H with a Sn vacancy [3.27]. These two possible H-V_{Sn} configurations are shown in Fig. 3.2 (c) and (d). In the same study, some H in SnO_2 was determined to be undetectable by IR spectroscopy or "hidden", including H_O centers whose vibrational line is suggested to be in a spectral region where the sample is opaque.

Annealing ZnO in H or D also generates some differences in its IR spectra. For instance, H_i decays upon annealing while H_2 molecules are formed. These molecules provide a hydrogen reservoir in ZnO that can be partially converted back to H_i by further thermal treatments [3.28-3.30]. These results show that there is an inter-conversion reaction between H_i and H_2 molecules driven by thermal treatments that make the conductivity of ZnO highly sensitive to thermal history. Therefore, since H_O is thermally more stable and will not decay until annealing at around 500°C, it is believed that H_O is the hydrogen-related source of conductivity in as-grown ZnO samples. In this chapter, IR spectra obtained for SnO_2 will be evaluated in the light of information available for ZnO and its hydrogen behavior after various thermal treatments. Furthermore, the diffusion characteristics of H_i and H_O are different in ZnO; Hi diffuses rapidly through the bulk of material that is a few millimeters thick and H_O is only found in the near surface region [3.20]. The differentiation of these defects will be attempted for SnO_2. It should

be noted that both H_i and H_O can be introduced in ZnO and SnO_2 by annealing in an H_2 ambient at elevated temperatures as will be performed in this study.

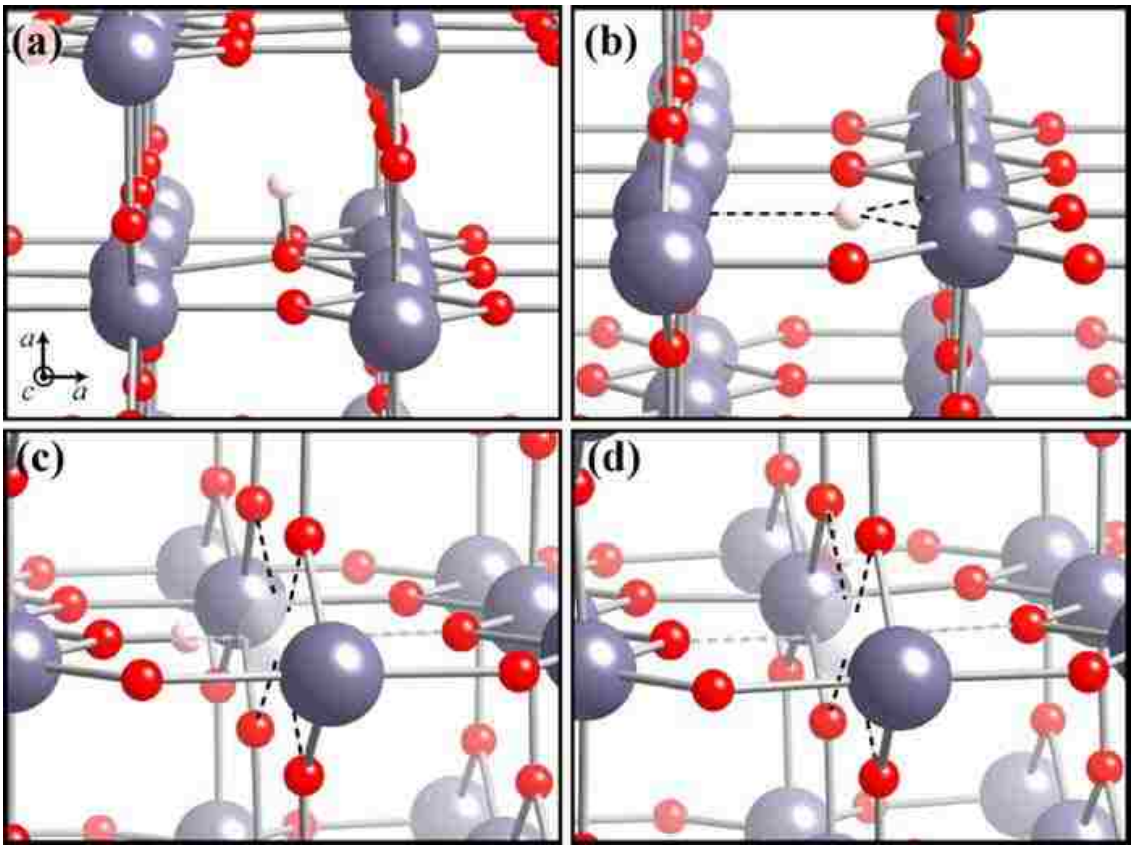

Fig. 3.2: Configurations of several H-related defects in SnO_2. (a) Interstitial hydrogen (H_i). (b) Hydrogen at an oxygen vacancy (H_O). Two possible structures of the V_{Sn}-H complexes in SnO_2 are shown: (c) H bonded to one of the Sn vacancy's axial O atoms and (d) H bonded to one of the Sn vacancy's equatorial O neighbors. The transparent atom corresponds to the V_{Sn} site. Gray (black) dashed lines correspond to the axial (equatorial) bonds.[3.27]

The polarization properties of the vibrational absorption arising from O-H centers in SnO_2 that are produced by thermal treatments will be investigated. Referring to Fig. 3.1, it can be seen that the normal to the plane of O and its three Sn neighbors is itself normal to the c-axis. The unique configuration of the Sn-O bonds with the above mentioned angles to the c-axis allows IR polarization experiments to provide additional information on the microscopic O-H defect structures in SnO_2.

This chapter reports on our IR vibrational spectroscopy study of hydrogen related impurities in SnO_2. By interpreting these results and comparing them to ZnO, we have obtained a good understanding of hydrogen centers in SnO_2, how they are formed and affected by thermal treatments, and their relationship to free carriers that are introduced by hydrogen. Moreover, we have performed a polarization study that reveals the O-H bond angles that are formed and also helps to assign defect structures to specific IR lines.

3.2 Experimental Procedures

Hydrogen impurities in SnO_2 have been analyzed experimentally using vibrational spectroscopy. Rutile phase, bulk single crystal SnO_2 samples were prepared and used in our experiments. These samples had been grown at Oak Ridge National Laboratory by the vapor transport method with H_2 carrier gas [3.31], which caused OH centers to be present even in as-grown samples. In order to introduce additional deuterium or hydrogen into the samples for our measurements, as-grown samples were placed in sealed quartz ampoules with 2/3 atm of D_2 or H_2 gas at room temperature and then annealed at elevated temperature. The treatments in D_2 or H_2 were terminated by quenching the ampoule to room temperature in

water to complete the annealing treatment. H_2 and D_2 treatments gave rise to an opaque layer of Sn at the sample surface which was removed by lapping with silicon carbide (280 and 600 mesh grit) and polishing with aluminum oxide powder (3.0 micron) and diamond paste.

IR absorption spectra were measured with a Bomem DA3.16 Fourier transform infrared spectrometer that was outfitted with an InSb detector and a KBr beam splitter. Light was polarized with a wire grid polarizer that was placed after the sample. O-H and O-D vibrational stretching modes for SnO_2 samples were measured at liquid He temperature (4.2 K). The samples were cooled with a Helitran, continuous-flow cryostat. IR spectra of the free carrier absorption were measured for SnO_2 samples at room temperature to provide a contact-free method to probe the free carrier concentration that is convenient for annealing experiments.

The subsequent anneals were performed in a tube furnace in a flowing inert gas (He) and terminated by quenching the sample in water in order to examine the reactions and thermal stabilities of OH and its OD isotope. The SnO_2 samples used in our studies were stored in liquid N_2 (at 77 K) between measurements since the OH (OD) lines and free carrier absorption are not thermally stable for long storage times at room temperatures. However, a few of our samples were intentionally stored at room temperature to probe the thermal stabilities of the various hydrogen centers.

3.3 Experimental Results

3.3.1 IR Spectra

In our first experiment, SnO_2 samples that contained H, D, or both H and D were studied using polarized light with electric vector perpendicular to the c-direction. Fig. 3.3 shows IR

spectra (4.2°K) of five specimens with different annealing conditions: (i) as grown sample, (ii) annealed in He at 500°C for 30 min and quenched rapidly in D_2O, (iii) annealed in D_2 at 700°C for 30 min (after pre-annealing in He at 1100°C for 5 hours to remove hydrogen from the as grown sample), (iv) annealed in an H_2 ambient at 700°C for 30 min, (v) annealed in a D_2 ambient at 700°C for 30 min. In spectra (iii), (iv), and (v), SnO_2 samples were placed in sealed quartz ampoules containing H_2 or D_2 gas at 2/3 atm at room temperature and annealed in a tube furnace. Each annealing treatment was terminated by quenching the ampoule in water to room temperature except for the experiment in Fig. 3.3 (ii). On the right side of Fig. 3.3, baseline corrected spectra focusing on the O-H absorption lines are also shown.

As seen from spectrum (i), the as-grown samples have hydrogen centers (a strong O-H line at 3261.5 cm^{-1} and weaker lines at 3258.0 and 3272.0 cm^{-1}) which do not give rise to electrically active shallow donors. Simply annealing the as-grown sample in He and subsequent quenching in D_2O produced an additional O-H line at 3156.0 cm^{-1} in spectrum (ii) and the optical transparency of the sample was not changed. D_2O was used to make sure that the quenching liquid was not the source of H. Annealing SnO_2 at 300°C and 700°C in a flowing He ambient also introduced the 3156.0 cm^{-1} line but with reduced intensity. Spectra (i) and (ii) are shown without baseline corrections. The spectra for annealing treatments at 300°C and 700°C in a He ambient also had flat baselines.

When a similar annealing procedure was performed in H_2 (spectrum (iv)), the 3156.0 cm^{-1} line was also introduced with a higher intensity, as well as additional lines at 3281.8, 3334.2, and 3343.2 cm^{-1}. This treatment also gave rise to broad low frequency absorption, i.e., the steeper slope of spectra seen at low frequency, due to the introduction of free carriers

[3.32], similar the results obtained by annealing ZnO in an H_2 ambient [3.29, 3.33-3.34]. Annealing in D_2 (spectrum (v)) produced several O-D lines that are frequency shifted partners of the O-H lines along with broad absorption due to free carriers.

The frequencies of the O-H and O-D lines and their ratio are listed in Table 3.1 .The ratios of H to D mode frequencies have values close to 1.34 which is consistent with their assignment to O-H and O-D stretching.

Interestingly, the O-H line spectrum that was observed in spectrum (iv) (i.e., by annealing in an H_2 ambient) was also produced by annealing in D_2. This result can be attributed to the interaction of hydrogen that was already present in our samples with native defects that were introduced by the heat treatment. This result is reinforced by spectrum (iii). For spectrum (iii), an as-grown sample was pre-annealed at 1100°C for 5 hours in a flowing He ambient to remove all of the hydrogen introduced during crystal growth. After removing hydrogen from the as-grown sample, the sample was annealed in a D_2 ambient for 30 min at 700 °C. Only deuterium centers were then produced, unlike the result shown in spectrum (v) which has both O-H and O-D centers together. Note that free carrier absorption was observed in cases (iii), (iv), and (v), in increasing order.

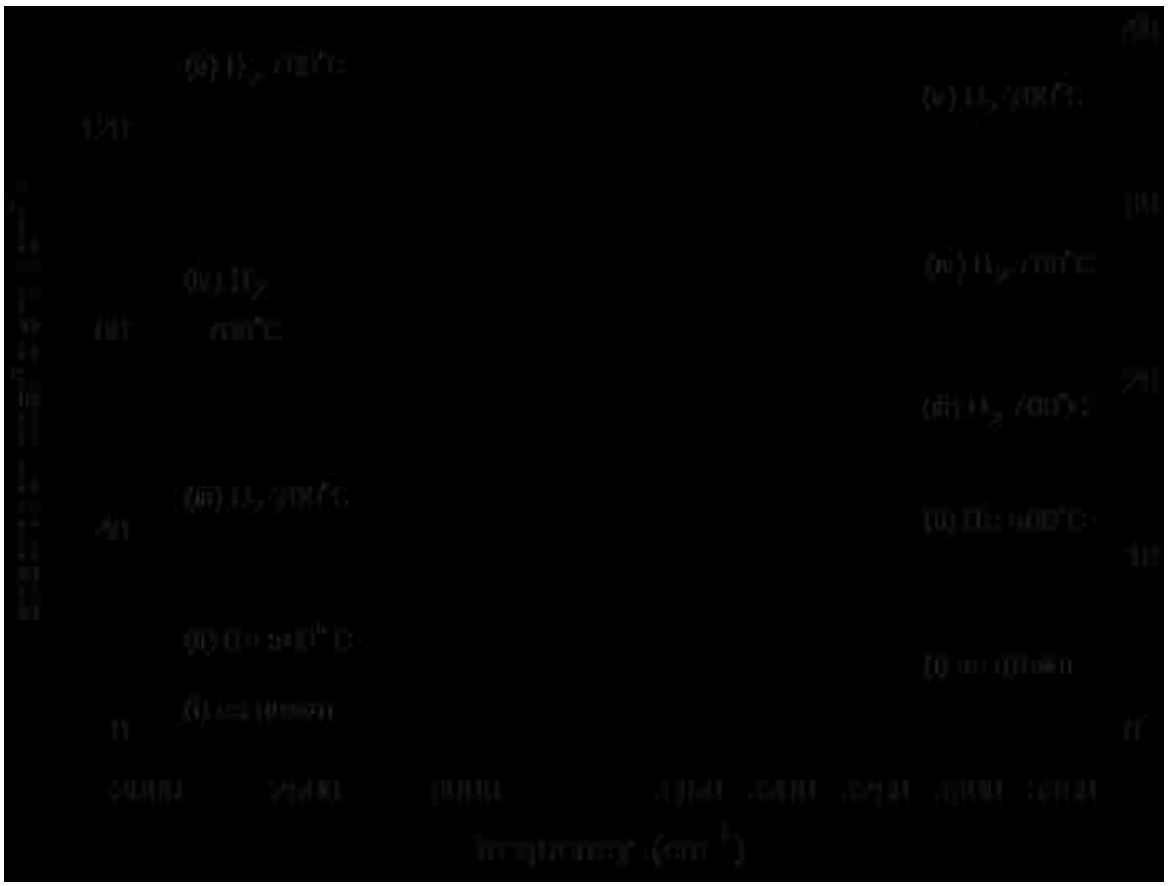

Fig. 3.3: IR absorption spectra of SnO_2 annealed in different ambients and at different temperatures for 30 min at 4.2°K and with a resolution = 1 cm^{-1}. The figure on the left shows the free carrier absorption and the figure on the right has been baseline-corrected to focus on the IR absorption lines in the O-H stretching region. An empty sample holder was used as the reference.

ω_H (cm^{-1})	ω_D (cm^{-1})	r (ω_H/ ω_D)	assignment	$I_{//}$ / $I_{\perp}$
3156.1	2360.4	1.337	H_i	0
3258.1	-----	-----	O-H	0
3261.5	2425.7	1.345	O-H	0
3272.0	2432.6	1.345	O-H	0
3281.8	2438.5	1.346	O-H	0
3281.8	2446.9	1.341	O-H	0.5
3299.9	2451.3	1.346	O-H	0
3334.2	2477.5	1.346	$(O-H)_2$	1
3343.2	2483.8	1.346	$(O-H)_2$	0

Table 3.1: Frequencies of O-H and O-D vibrational modes observed for an SnO_2 sample that had been annealed in H_2 or D_2 gas. The ratio r of the O-H and O-D line frequencies and the polarization ratio $I_{//}$ / $I_{\perp}$ for the various lines are also shown.

Annealing in H_2 and D_2 ambients made the sample partially decompose and damaged the sample surfaces. These treatments introduced an opaque layer of Sn on the surface of the samples with a thickness of about 0.05 mm that was removed by lapping and polishing. Moreover, the deuterium treated sample shown in Fig. 3.3 (v) was mechanically thinned in several steps from each side. The thinning process was started with an initial thickness of 0.5 mm and ended at 0.2 mm. After each thinning step, an IR spectrum was measured in order to determine whether the O-H and O-D lines and free carriers were located at the damaged sample surface or throughout the sample bulk. Spectra of the O-H and O-D absorption lines and for the free carrier absorption measured after each step thinning are shown in Fig. 3.4. The O-H and O-D IR lines along with the free carrier absorption were reduced uniformly as the

sample was thinned so as to keep the absorption coefficient approximately constant. These results show that the O-H and O-D defects and the free carrier absorption come from defects distributed throughout the sample's initial 0.5 mm thickness.

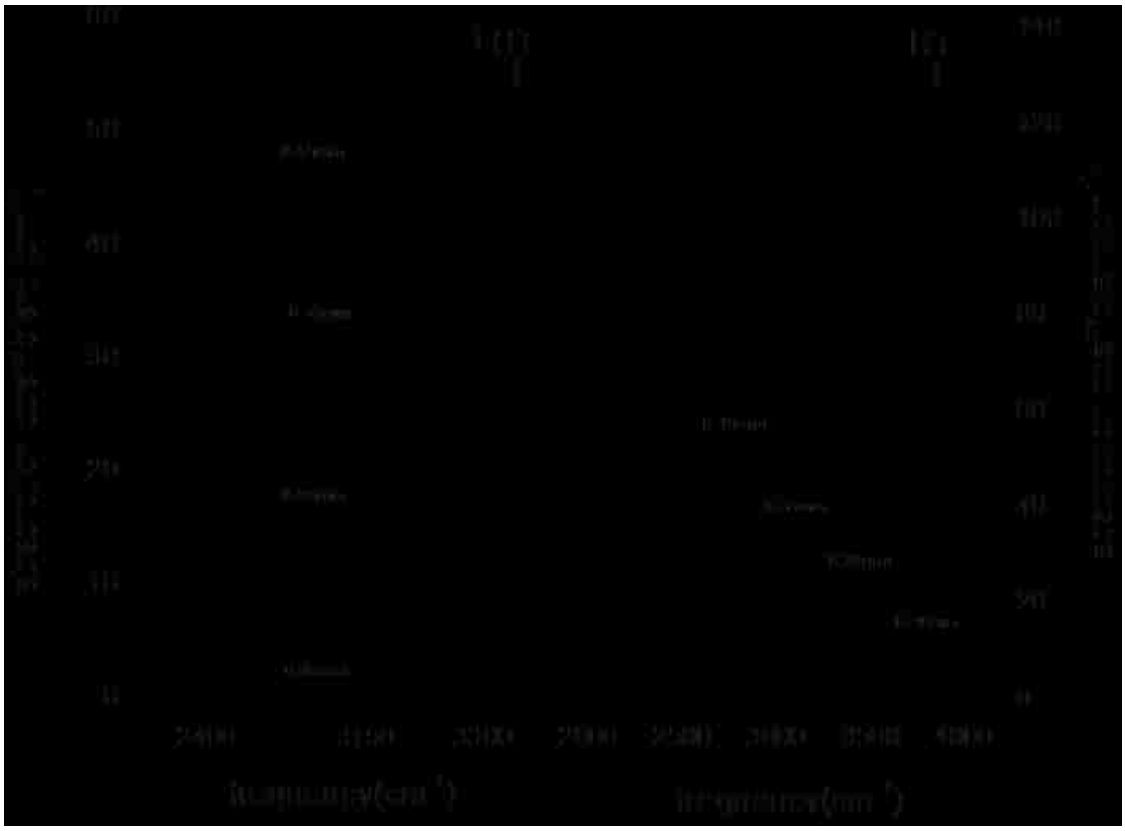

Fig. 3.4: IR absorption spectra (resolution=1cm^{-1}) for an SnO_2 sample that had been annealed in a D_2 ambient at 700°C for 30min. The sample was subsequently thinned in several steps from both sides, and measured with polarized light with **E**⊥**c**. (a)(baseline corrected) focused on the IR absorption lines seen in the O-H and O-D stretching regions and measured at 4.2°K . (b) Free carrier absorption measured at RT for each thinning step. An empty sample holder was used as the reference.

3.3.2 Polarization Properties

Fig. 3.5 shows the results for a SnO_2 sample that had been annealed in an H_2 ambient at 700°C to produce O-H centers and subsequently annealed at 100°C in a He ambient to increase the relative intensities of the 3281.8, 3334.2, and 3343.2 cm^{-1} lines. IR spectra for this sample were measured using light with two different polarizations: parallel and perpendicular to the c-direction of the rutile structure. O-H lines at 3156.1, 3261.5, and 3343.2 cm^{-1} were all polarized perpendicular to the c-direction meaning that the O-H bonds for these defects lie in the a-b plane of the rutile structure while the line at 3334.2 cm^{-1} was polarized parallel to the c-direction. Moreover, the line at 3281.8 cm^{-1} had components in both directions. Surprisingly, the intensity of the O-H line at 3281.8 cm^{-1} and its dependence on polarization have been found to depend also on the prior annealing treatment of the sample.

Treating a SnO_2 sample in a D_2 ambient (at 700°C for 30 min.) gives rise to both H- and D-containing centers together. Fig. 3.6 presents spectra for both the H and D centers for an as-treated and subsequently annealed sample (at 150°C for 30 min. in He flowing ambient) to examine the polarization properties of the lines and their annealing behavior. In the O-D region near the frequency 2400 cm^{-1} for $\mathbf{E}\perp\mathbf{c}$, the 2360.4, 2425.7, 2432.6, and 2451 cm^{-1} lines are seen in Fig. 3.6 (a), and for the O-H region [Fig. 3.6 (b)], these lines correspond to the 3156.1, 3261.5,3272.0, and 3299.9 cm^{-1} lines respectively, as shown in Table 3.1. The O-D line at 2446.9 cm^{-1} shows absorption for both the $\mathbf{E}\perp\mathbf{c}$ and $\mathbf{E}//\mathbf{c}$ polarizations, with an intensity ratio of $I_{//}/I_{\perp}$ = 0.5. The subsequent annealing of the sample at 150°C in He increases the intensity of most of the lines. For example, the intensity of the 2438.5 cm^{-1} line grows substantially for $\mathbf{E}\perp\mathbf{c}$ after annealing in He.

In order to understand the unusual behavior of the line at 3281.8 cm^{-1} upon annealing, the O-H and O-D regions in Fig. 3.6 are examined and compared for both polarizations. The intensity ratio, $I_{///}/I_{\perp,}$ for the line at 3281.8 cm^{-1} is around 0.5, which is similar to the ratio of corresponding O-D line at 2446.9 cm^{-1}, in the as-treated sample. After annealing at 150°C, the 3281.8 line for the polarization **E**⊥**c** grows in intensity more than the same line for the polarization **E//c** .The intensity ratio, $I_{///}/I_{\perp}$, is decreased to around 0.3. On the contrary, in the O-D range upon with annealing, the intensity of the 2446.4 cm^{-1} line is increased slightly for both polarizations. This is a different behavior than that of the 3281.8 cm^{-1} line which grows in intensity primarily for **E**⊥**c**. We note that the 2438 cm^{-1} line in the OD range grows substantially in intensity for **E**⊥**c**. This comparison upon annealing shown in Fig. 3.6 (a) and (b) reveals that the lines at 2438.5 and 2446.4 cm^{-1}, that are separate in the O-D spectrum, have isotopic partners in the O-H spectrum that lie at the same frequency, 3281.8 cm^{-1}. The coincidence of two O-H modes with different polarization properties and annealing behaviors explains the unusual changes in the ratio $I_{///}/I_{\perp}$ for the 3281.8 cm^{-1} line upon annealing.

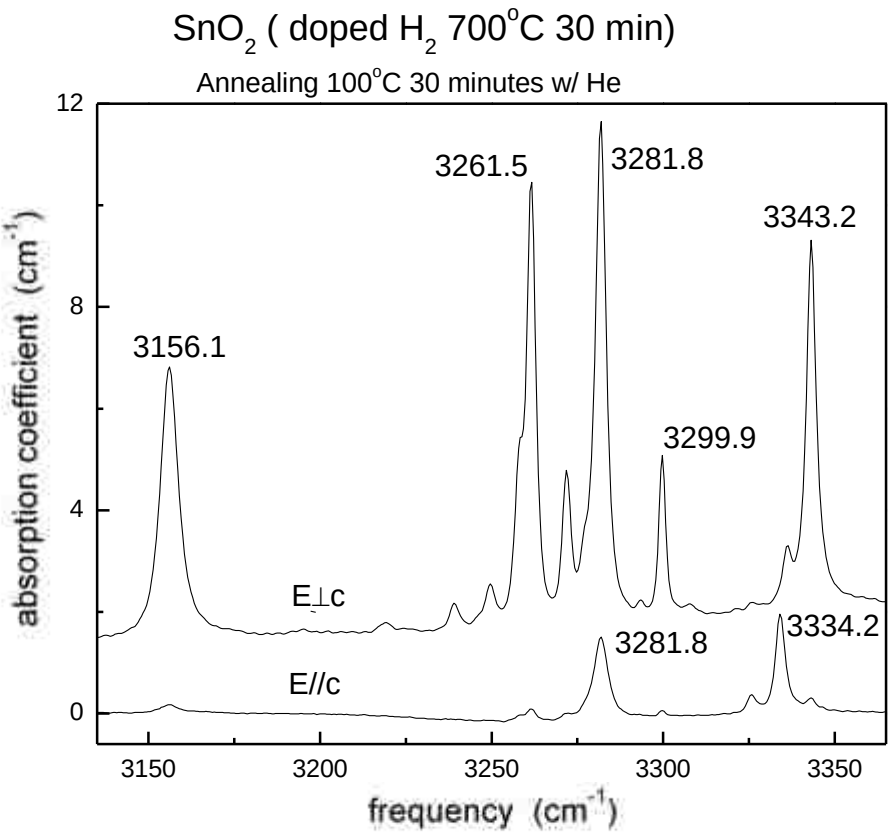

Fig. 3.5: IR absorption spectra of SnO_2 annealed in an H_2 ambient at 700°C for 30 min and subsequently annealed in a He ambient at 100°C for 30 min. Spectra were measured with polarized light with electric vectors both perpendicular and parallel to the c-axis at 4.2°K and resolution = 1 cm^{-1}.

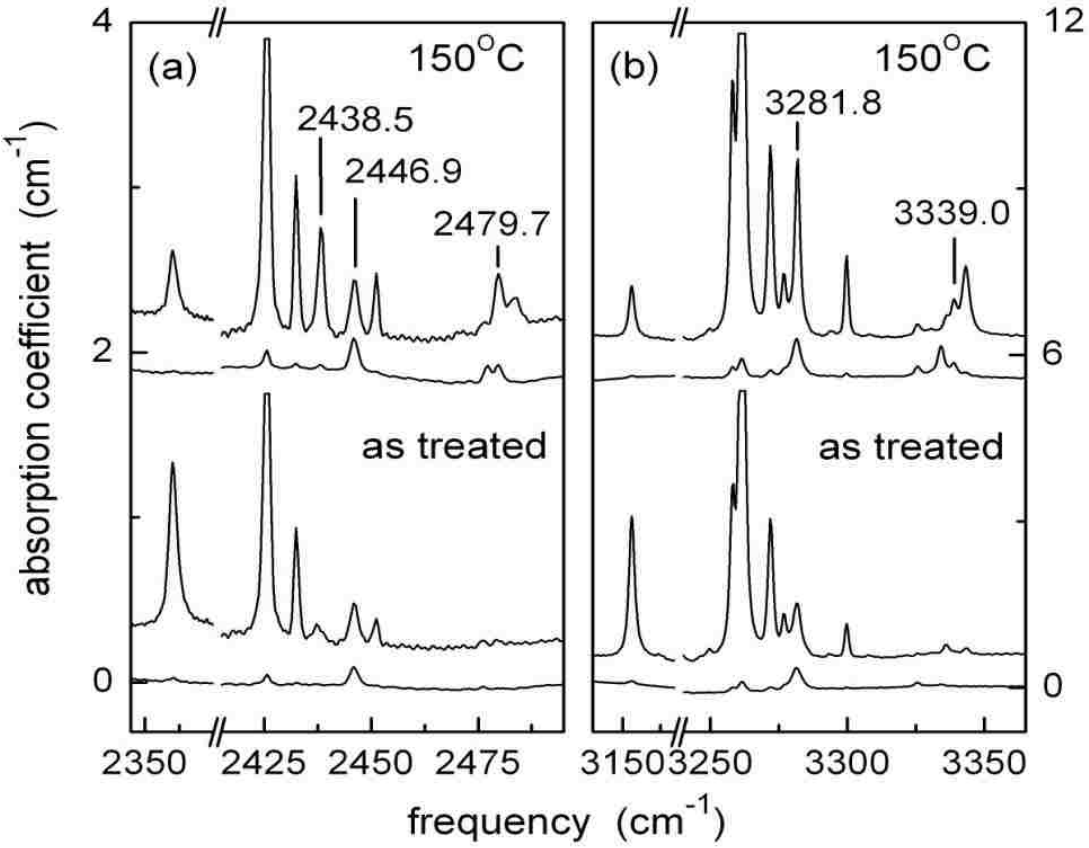

Fig. 3.6: IR absorption spectra (T=4.2° K, resolution=1 cm^{-1}) measured for light polarized with electric vector **E⊥c** (upper) and with **E//c** (lower). D was introduced by an anneal (30 min) in D_2 gas at 700 °C for the "as-treated" sample. The sample was subsequently annealed (30 min) at 150 °C in a He ambient. (a) the O-D stretching region. (b) the O-H stretching region. The line at 3261.5 (2425.7) was truncated so that weaker lines in the spectrum could be seen more clearly.

In our experiments with polarized IR light, additional O-H and O-D lines show interesting behavior upon annealing. When deuterated or hydrogenated samples are annealed near 100°C or 150°C in He as seen in Fig. 3.5 and Fig. 3.6, the intensities of the lines at 3334.2 and

3343.2 cm^{-1}, which are very weak in as treated samples, increase. However, only in a deuterated sample, the line at 3339.0 cm^{-1}, which is not present in an as-treated sample, grows in intensity upon annealing. These three lines have distinctive polarization properties: the line at 3334.2 cm^{-1} has a component only for **E//c**, and the line at 3343.2 has a component only for **E⊥c.** The 3339 cm^{-1} line is seen in both polarizations. For the O-D range, the corresponding lines have the same annealing and polarization properties. The line at 2477.5 cm^{-1} is seen for **E//c,** and the lines at 2483.8 cm^{-1} is seen for **E⊥c.** The line at 2479.7 cm^{-1} is seen for both polarizations.

Studies performed by Hlaing Oo *et al*. [3.27] reached different conclusions than the results discussed above. Absorption for only the **E⊥c** polarization was reported for the O-H and O-D centers in SnO_2. Moreover, the lines at 3334.2 and 3343.2 cm^{-1} were seen only weakly in the spectra reported by Hlaing Oo *et al.* and were not examined in their studies [3.27].

3.3.3. Annealing Behavior

The thermal stabilities of the free carrier absorption and also the various O-H and O-D centers were examined in another set of experiments. Free carrier absorption spectra, measured at room temperature, for a hydrogenated SnO_2 sample that was subsequently annealed at various temperatures in a He ambient prior to each measurement are shown in Fig. 3.7 (a). At the end of each annealing treatment, the sample was quenched rapidly in water to room temperature. Fig. 3.7 (b) shows the difference of the absorption coefficients at 2000 and 4000 cm^{-1}, which was taken as a measure of the strength of the free carrier absorption vs. the annealing temperature. The free-carrier absorption shows an interesting dependence on

the annealing temperature. The plot in Fig. 3.7 (b) shows an approximately 25% decrease in the free carrier absorption at around 100-150°C, which recovered at around 200°C. The free carrier absorption also decayed almost completely after an anneal at 650°C.

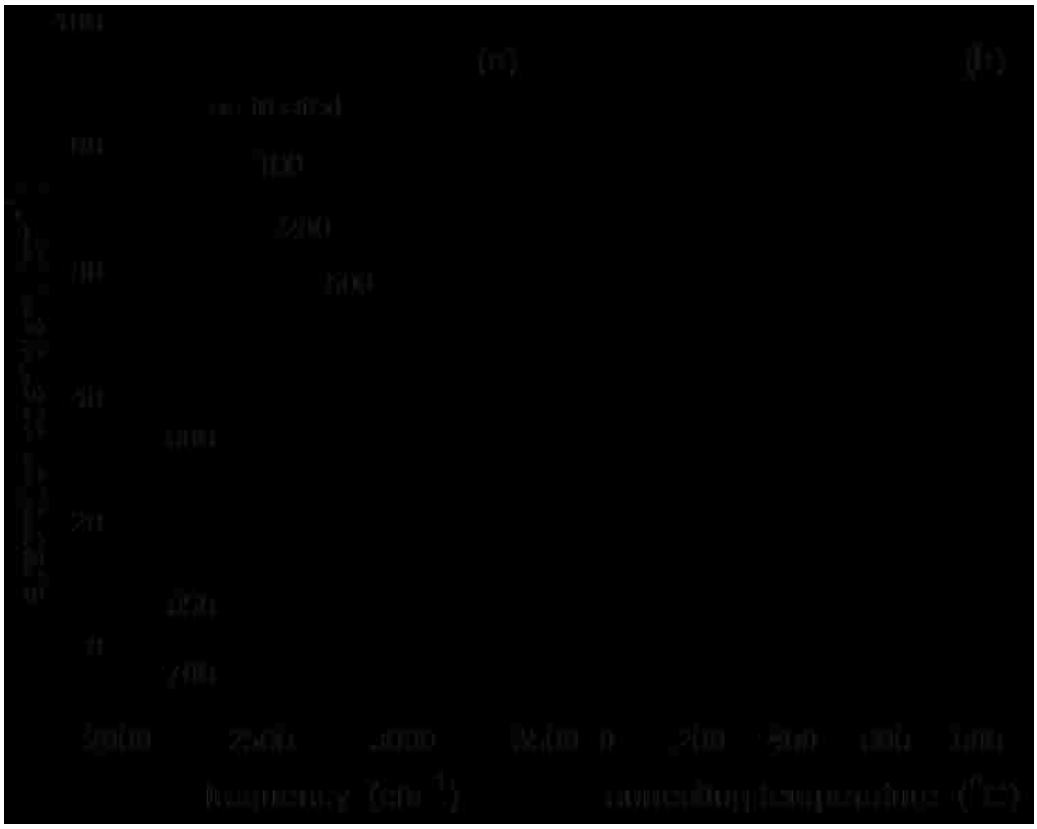

Fig. 3.7: IR absorption spectra for SnO_2 annealed in an H_2 ambient at 700°C for 30 min with a selection of subsequent annealing treatments in a He ambient for 30 min at the temperatures shown. (a) The free carrier absorption spectra for different annealing temperatures. (b) Difference in the absorption coefficients measured at 2000 cm^{-1} and 4000 cm^{-1} vs. the annealing temperature. The spectrum of SnO_2 annealed subsequently at 900°C for 30 min to remove H (measured at room temperature with a resolution = 1 cm^{-1}) was used as a reference for these data.

Fig. 3.8 shows IR spectra from the same experiments but measured at 4.2°K. The spectra are focused on the O-H absorption lines. A baseline correction has been made remove the absorption due to free carriers to help observe the individual line changes upon annealing. To investigate the annealing behavior in more detail, the areas of the individual absorption lines determined by fitting the spectra with sums of Lorentzian line shapes (by using Peak Fit v4 software) are plotted vs. the anneal temperature in Fig. 3.9 (a) and (b). A replica of Fig. 3.7 (b) is also presented as Fig. 3.9 (c) for comparison purposes. It is seen in Fig. 3.9 that upon annealing at 150°C, the intensity of the 3156.1 cm^{-1} line was decreased while the intensities of several of the other lines (3281.8, 3343.2, 3281.8, and 3334.2 cm^{-1}) was increased. After annealing at 200°C, the 3156.1 cm^{-1} line recovered while several of the other lines lost intensity. Then, upon annealing at 650°C, the majority of the 3156.1 cm^{-1} line intensity was eliminated.

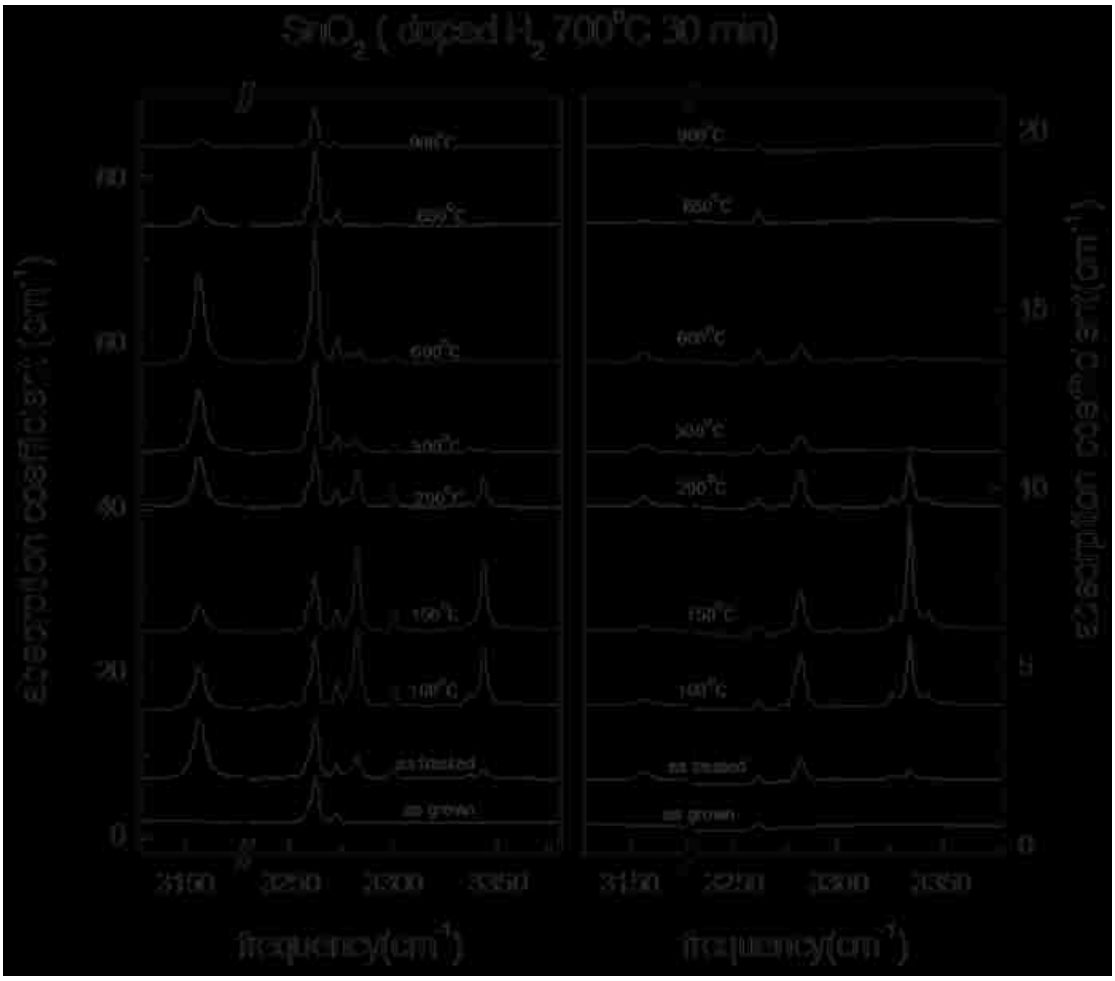

Fig. 3.8: Baseline corrected IR absorption spectra (T=4.2° K, resolution=1 cm^{-1}) for SnO_2, focused on the IR absorption lines in the O-H stretching region. The sample was first annealed (30 min) at 700 °C in H_2 gas to introduce H. This anneal was terminated by a quench to room temperature in water. The sample was then sequentially annealed (30 min) in a flowing He ambient at the temperatures shown. Anneals were terminated by a quench to room temperature in water. (a) measured with polarized light with **E⊥c** (left). (b) measured with polarized light with **E//c** (right). An empty sample holder was used as the reference.

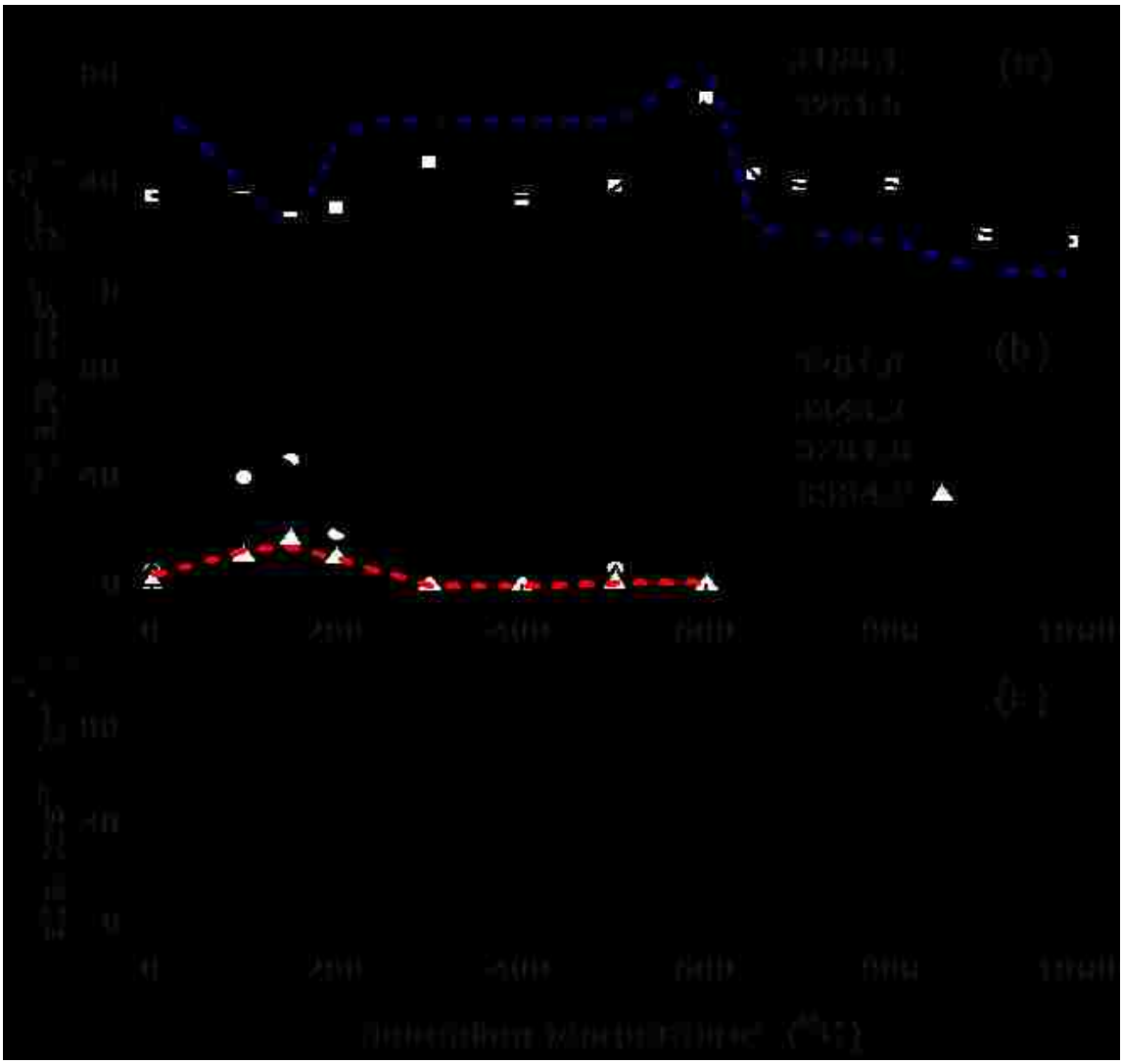

Fig. 3.9: Spectra for a SnO_2 sample annealed in an H_2 ambient at 700°C for 30 min and subsequently annealed in a He ambient at different temperatures for 30 min. Panels (a) and (b) show the integrated absorption coefficients for the IR lines at the frequencies indicated vs. annealing temperature. Open and closed circles in panel (a) and open and closed squares in panel (b) are for **E⊥c**. Open and close triangles in panel (b) are for **E//c**. Panel (c) shows the difference in the absorption coefficients due to free carriers measured at 2000 cm^{-1} and 4000 cm^{-1} vs. the annealing temperature.

Finally, an experiment to investigate the effects of room temperature storage was performed for a total of 108 days. Free carrier absorption spectra and baseline corrected IR spectra showing the O-H lines that had been measured at various times are plotted in Fig. 3.10 (a) and (b), respectively. Also, results are shown for a final measurement when the sample, at the end of the 108 day period, was re-annealed at 500°C in flowing He for 30 min and quenched rapidly. In order to examine the behavior of the individual O-H lines upon annealing at room temperature, the intensities of the lines are plotted versus the (room temperature) annealing time in Fig. 3.11 (a) and (b). Moreover, the strength of the free carrier absorption for the as-grown sample, the hydrogenated sample, and the sample annealed in He after a long time room temperature annealing are shown in Fig. 3.11 (c). The free carrier absorption decreased up to 65 days and by an amount of nearly 35% compared to the as-treated sample, whereas, after that, no significant change occurred. Similarly, the intensity of the 3156.1 cm^{-1} line decreased during the first 65 days and was nearly eliminated. Over the same time period, the intensity of the 3261.5 cm^{-1} line also decreased by 24% while the intensities of the lines at 3281.9 and 3343.2 cm^{-1} were increased. The re-annealing procedure in a He ambient at 500°C recovered the free carrier absorption, brought back the lines at 3156.1 and 3261.5 cm^{-1}, and almost eliminated the lines at 3281.9 and 3343.2 cm^{-1}. Furthermore, the total intensity of all of the O-H lines was found to be nearly constant for the various spectra shown in Fig. 3.10 and Fig. 3.11, that is, for the as-treated sample, following the subsequent storage times at room temperature, and following heat treatment at 500 °C. These results suggest that the various O-H centers have IR lines with similar oscillator strengths and that these centers can be inter-converted into one another by the appropriate thermal treatments.

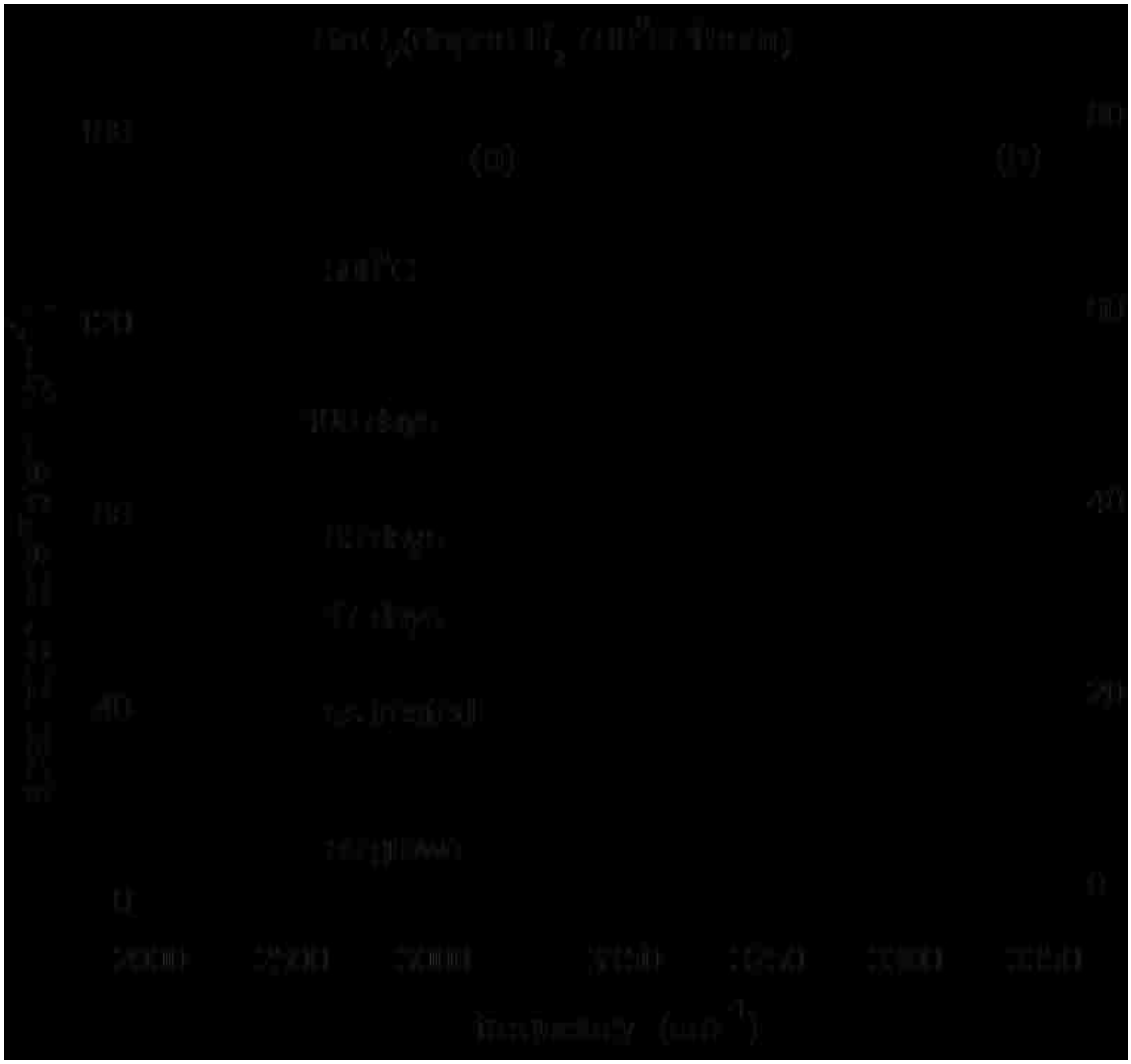

Fig. 3.10: IR absorption spectra for SnO_2 annealed in an H_2 ambient at 700°C for 30 min and subsequently stored at room temperatures for the times that are indicated. Spectra were measured at 4.2°K with a resolution = 1 cm^{-1}. (a) shows the free carrier absorption for the different storage times. (b) baseline-corrected spectra that focuses on the IR absorption lines in the O-H stretching region. Spectra were measured with polarized light with E perpendicular to the c-axis. An empty sample holder was used as the reference.

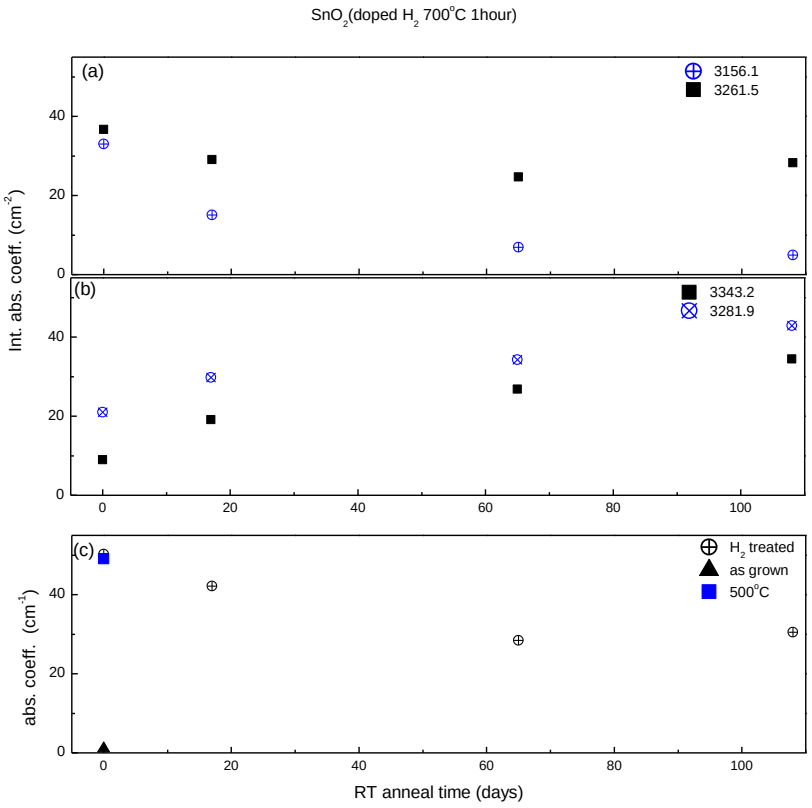

Fig. 3.11: The sample was SnO_2 annealed in a H_2 ambient at 700°C for 1h. and subsequently annealed at room temperature for the times that are indicated. Spectra were measured at 4.2°K with a resolution = 1 cm^{-1} for **E⊥c** polarization. The same sample was subsequently annealed in a He ambient at 500°C for 30 min. Panels (a) and (b) show the integrated absorption coefficients for the IR lines at the frequencies indicated vs. the storage times at RT that are indicated. Panel (c) shows the difference in the absorption coefficients due to free carriers measured at 2000 cm^{-1} and 4000 cm^{-1} vs. the storage times at RT for an as-grown sample, an H_2- treated sample, and a subsequently annealed sample in a He ambient.

3.4 Discussion

3.4.1 Production and thermal stability of H-related shallow donors

We have seen that hydrogenating SnO_2 samples at 700°C introduces a number of O-H vibrational lines along with free carrier absorption as shown in Fig. 3.3 and Fig. 3.7, similar to the results of Hlaing Oo *et.al*. [3.27]. To produce the spectra in Fig. 3.7 (a), a reference spectrum, measured for the same SnO_2 sample following a final anneal at 900°C for 30 mins in He ambient to remove H , was subtracted from the IR data. Therefore, hydrogen is the main cause for the free carrier absorption shown in Fig. 3.7 (a). Because SnO_2 and ZnO have similar electron masses and mobilities [3.35-3.37], the calibration of the free carrier absorption determined previously for ZnO annealed in an H_2 ambient [3.29, 3.33-3.34] can be applied approximately to the free carrier absorption spectra presented in Fig. 3.7 for the hydrogenated SnO_2 sample measured at room temperature. In order to determine the calibration of the free carrier absorption for hydrogenated ZnO, Hall measurements were performed by S. J. Pearton's group at the University of Florida in an earlier collaboration with our group [3.29]. The concentration of the free carriers is proportional to the absorption coefficient at a given frequency [3.33-3.34]. Thus, the absorption coefficient at 2000 cm^{-1} was taken as a measure of the free carrier absorption [3.29]. A calibration of the free carrier absorption coefficient at 2000 cm^{-1} was given by G. A. Shi *et. al.* [3.29, 3.39] for hydrogenated ZnO as

$$N_{fc} = 9.3 \times 10^{15}\ cm^{-2}\ \alpha(2000\ cm^{-1}) \qquad (3.1)$$

By applying this approximate calibration to hydrogenated SnO_2 samples, the free-carrier absorption shown in the "as-treated" spectrum in Fig. 3.7 corresponds to an electron concentration of $\approx 1 \times 10^{18}$ cm^{-3}. This result is in agreement with the early results of Samson and Fonstad [3.22]. In their studies, the hydrogenation of different SnO_2 samples (at 900°C) gave rise to shallow donors with concentrations between 9.8×10^{17} and 8×10^{18} cm^{-3}, and they suggested that H was the shallow donor [3.22].

Hydrogenation or deuteriation of SnO_2 samples gives rise to the strong free-carrier absorption and shallow donors with a concentration of approximately 10^{18} cm^{-3}. In order to understand if a large concentration of donors is produced only for the sample annealed in an H_2 or D_2 ambient, we examined the free carrier absorption for SnO_2 samples annealed in a He ambient as shown in Fig. 3.3 and Fig. 3.7. We found that these samples had at least 5 to 10 times smaller donor concentrations than was observed for hydrogenated SnO_2 samples.

From the results of annealing and room temperature storage experiments shown in Fig. 3.7 and Fig. 3.7, it can be seen that the observed thermal stabilities point to the presence of at least two H-related donors in SnO_2. The reduction of the free carrier absorption at around 100°C [Fig. 3.7 (b)] suggests that there is a donor species that is not thermally stable at this temperature. Furthermore, a more thermally stable species is seen to be responsible for the free carrier absorption that disappears at 650°C. The results for a long storage time at room temperature [Fig. 3.10 (a)] also support this conclusion since the free carrier absorption of a hydrogenated sample is reduced significantly (by 35 %) after 65 days, i.e., due to the presence of a donor that is thermally unstable at room temperature. Moreover, the remaining portion

of the free carrier absorption can be attributed to a more thermally stable donor and does not decay appreciably for longer times at room temperature.

3.4.2 Relationship of shallow donors to hydrogen centers

In this section, we will try to identify various hydrogen centers using different annealing strategies presented in the previous sections. It can be seen in Fig. 3.9 that the dip in the free carrier absorption at around 100 to 150 °C closely matches a similar reduction in the intensity of the O-H line at 3156 cm^{-1}. Additionally, the intensity of this line decays during a long storage time at room temperature [Fig. 3.10 (b)], in a fashion similar to the free carrier absorption [Fig. 3.10 (a)]. Finally, a re-annealing treatment at 500 °C in a He ambient recovers the intensity of both the 3156 cm^{-1} line and the free carrier absorption. All of these observations are consistent with the O-H center that gives rise to the 3156 cm^{-1} line being responsible for 35 % of the free carrier absorption.

A shallow donor that is thermally unstable near room temperature was found to be H_i by theory [3.10, 3.15, 3.27]. Furthermore, a strong O-H bond that lies perpendicular to the c-axis with a theoretical vibrational frequency of 3245 cm^{-1} was predicted [3.27, 3.38]. Hlaing Oo *et al.* [3.27] conducted a combined experimental and theoretical study and observed that the vibrational properties of the O-H center that gives rise to the 3156 cm^{-1} are consistent with the predicted theoretical properties. Therefore, the 3156 cm^{-1} line was assigned to H_i [3.27]. Our observations support this assignment.

Theory also predicted that H_o is a donor in SnO_2 with a greater thermal stability [3.15, 3.27]. Our experimental observations support the suggestion that H_o is responsible for the

portion of the free carrier absorption that remains stable until near 650°C for samples that had been heat treated in an H_2 ambient to introduce H. This more stable donor gave rise to about 65% of the total free carrier absorption.

The relationship between the two types of shallow donors and the corresponding H-related defects in SnO_2 closely resembles the previous findings for H in ZnO [3.29, 3.39]. In ZnO, H_i with an O-H vibrational line at 3611 cm^{-1} and H_o both act as shallow donors and approximately 85% of the donors that were formed after annealing in a H_2 ambient at 700 °C were not thermally stable near room temperature. The remaining 15% were observed to be stable up to 500 °C. Moreover, H_o in these samples was found to be formed near the sample surface.

When we introduced hydrogen (or deuterium) into SnO_2 samples, the sample surfaces were observed to be severely damaged. Both H_i and H_o are introduced deep into the bulk of the SnO_2 sample. This was determined by the step-by-step sample thinning process discussed earlier in the chapter and presented in Fig. 3.4. In SnO_2, H_o is distributed throughout the bulk of the sample following hydrogenation, in contrast to the case of ZnO, and is the dominant donor accounting for 65% of the free carrers. This result shows that the oxygen vacancies necessary for the production of the H_O donor center are introduced deep into the sample bulk by the damaging anneal in an H_2 ambient.

3.4.3 Properties of other O-H centers

Our spectra showed a number of different IR lines in addition to the 3156.1 cm^{-1} line which was assigned to H_i as a shallow donor. Most of the lines detected in our experiments

were the same as those observed by Hlaing Oo *et al.* [3.27], suggesting that these lines are due to O-H centers that involve H and intrinsic defects rather than impurities that are dependent on the sample source. In this section, an analysis of these lines will be presented, aided by the information obtained from polarized spectra.

Fig. 3.12 shows IR absorption spectra with **E⊥c** (upper) and **E//c** (lower) polarizations for SnO_2 samples that had been treated in three different conditions. In (a), the spectrum was measured for a sample that contained primarily O-D centers. Spectrum (b) was measured for a sample that contained O-H centers only. The spectra (c) and (d) focus on the D- and H-ranges, respectively, for a sample that contained both H and D. These samples were prepared by treatments in a D_2 or H_2 ambient followed by an anneal at 150 or at 200 °C in He for 30 min or for an anneal at room temperature for about 65 days to produce the defects of interest and to increase their intensities.

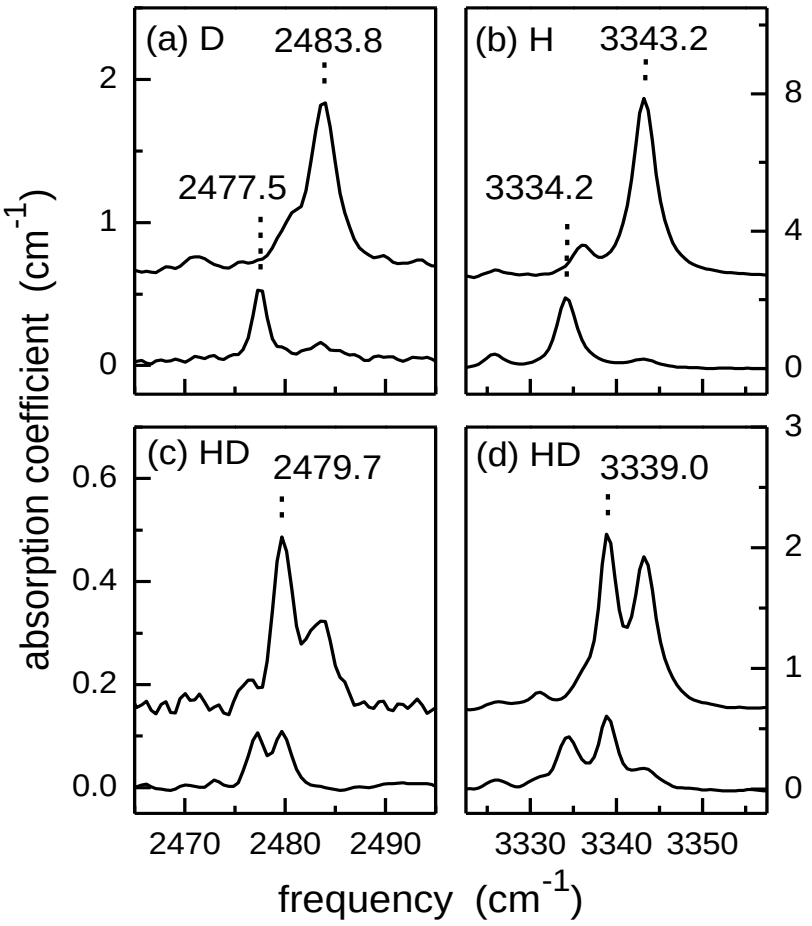

Fig. 3.12: IR absorption spectra (T= 4.2°K, resolution= 1 cm^{-1}) in the O-H and O-D stretching regions for the $(O\text{-}H)_2$ and $(O\text{-}D)_2$ centers measured with light polarized with electric vector **E⊥c** (upper) and with **E//c** (lower) for samples with different isotopic content. (a) is primarily D, (b) only H, (c) is H>D so the O-D mode of the O-HD center dominates, (d) is H ≈D. Here, H or D was introduced by an anneal (30 min) in H_2 or D_2 gas at 700°C. This treatment was followed by an additional anneal between room temperature and 200°C to produce the defect of interest.

The IR lines at 3334.2 and 3343.2 cm^{-1} were observed to be initially present in a hydrogenated sample and with distinct polarization characteristics [Fig. 3.12 (b)]. The 2477.5 and 2483.8 cm^{-1} lines are due to the corresponding O-D modes [Fig. 3.12 (a)]. When a sample that contains both H and D is measured, an additional line appears at 3339.0 cm^{-1} (2479.7 cm^{-1} for O-D), midway between the 3334.2 and 3343.2 cm^{-1} lines (2477.5 and 2483.8 cm^{-1}) and this additional line is observed for both polarizations **E⊥c** and **E//c** [Fig. 3.12 (c) and (d)]. This is a characteristic behavior of a center that has two equivalent H (D) atoms, such as $(O\text{-}H)_2$ or $(O\text{-}D)_2$ complexes. Considering H, 3334.2 and 3343.2 cm^{-1} lines are assigned to $(O\text{-}H)_2$ while the line midway between at 3339.0 cm^{-1} corresponds to the dynamically decoupled O-H mode that occurs when one of the H atoms in the $(O\text{-}H)_2$ center is replaced by a D atom. In other words, this line is due to a O-H—D-O center. Similarly, the line at 2479.7 cm^{-1} for the deuterated complex is due to the dynamically decoupled O-D mode that occurs when one of the D atoms in the $(O\text{-}D)_2$ complex is replaced by an H atom. A similar defect with two equivalent H atoms is also found in ZnO. In this case, a complex of two H atoms with a zinc vacancy (V_{Zn}-H_2) has been identified. Although the IR data and the behavior of the H or D-related defects are very similar in ZnO and SnO_2, the determination of possible candidates for microscopic defect structures in SnO_2 is not straightforward. For this purpose, a theoretical analysis based on our experimental data was performed by Prof. Fowler and will be discussed in the following section.

The polarization dependence of the O-H absorption gives us important information to help assign the O-H modes to specific structures in SnO_2. As shown in Fig. 3.5, the IR lines at 3261.5 and 3281.8 cm^{-1} have distinctive polarization properties (the 2361.5 cm^{-1} line is seen

only for **E⊥c** and the 3281.8 cm^{-1} line has components for both the **E⊥c** and **E//c** polarizations). Theory [3.27] by Hlaing Oo. *et al*. suggested that these lines were due to complexes of H with a Sn vacancy (V_{Sn}).Two possible configurations for V_{Sn}-H complexes are shown in Fig. 3.13 (a) and (b) [3.27] and in Fig. 3.2 (c)and (d). In Fig. 3.13 (a) and in Fig. 3.2(c), H has a bond with one of the Sn vacancy's axial O neighbors, and this O-H bond is perpendicular to the c-axis. In Fig. 3.13 (b) and in Fig. 3.2 (d), H has a bond with one of the Sn vacancy's equatorial O neighbors, and the O-H bond has both parallel and perpendicular components with respect to the c-axis. Therefore, the 2361.7 cm^{-1} line is consistent with an assignment to H bonded to one of the V_{Sn} defect's axial O atoms as shown in Fig. 3.13 (a) and the 3281.8 cm^{-1} line might correspond to a defect complex with H bonded to one of the V_{Sn} defect's equatorial O atoms as shown in Fig. 3.13 (b). (These assignments, based on only the polarization properties of the IR lines, are reversed from the defect assignments suggested by Hlaing Oo *et al.* [3.27]). In the next section, the insight of the theory performed by Prof. Fowler on the assignments of the various O-H modes will be discussed.

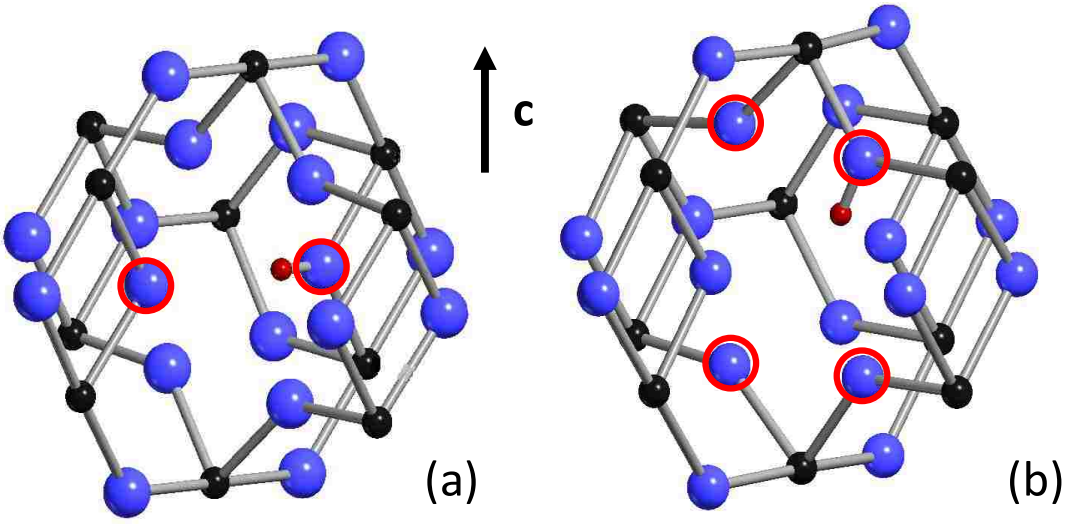

Fig. 3.13: Configurations of V_{Sn}-H complexes in SnO_2. (a) shows the structure with H bonded to one of the Sn vacancy's axial O atoms with its O-H bond perpendicular to the c axis of the rutile structure. (b) shows the structure with H bonded to one of the Sn vacancy's equatorial O neighbors.

3.4.4 Defect models from theory and polarized absorption spectra

IR absorption experiments using polarized light have resulted in significant observations on the structure and behavior of O-H defects in SnO_2. A further analysis based on theory and simulations to support our experimental data has been provided by Prof. Beall Fowler [3.40].

Top portions in Fig. 3.6 (a) and (b) show the IR spectra for D_2 and H_2 treated samples measured for **E⊥c** and **E//c**. As was discussed in the preceding sections, the line at 2360.4 cm^{-1} (3156.1 cm^{-1}) has been assigned to interstitial D (H). The O-D (O-H) line at 2425.7 cm^{-1} (3261.5 cm^{-1}) and several other lines are observed only with **E⊥c** polarization while the line at 2446.9

cm^{-1} (3281.8 cm^{-1}) had components both for **E⊥c** and **E//c**. In order to find the intensity ratio of the components of this line for the two polarizations, Gaussian line shapes were used to fit the spectra of different samples. Fig. 3.14 shows a representative fit and Table 3.2 lists the parameters obtained from this fit. The intensity ratio for the line at 2446.9 cm^{-1} with **E⊥c** and **E//c** polarizations was found to be

$$I_{//}(2446.9) \Big/ I_{\perp}(2446.9) = 0.54 \pm 0.05 \tag{3.2}$$

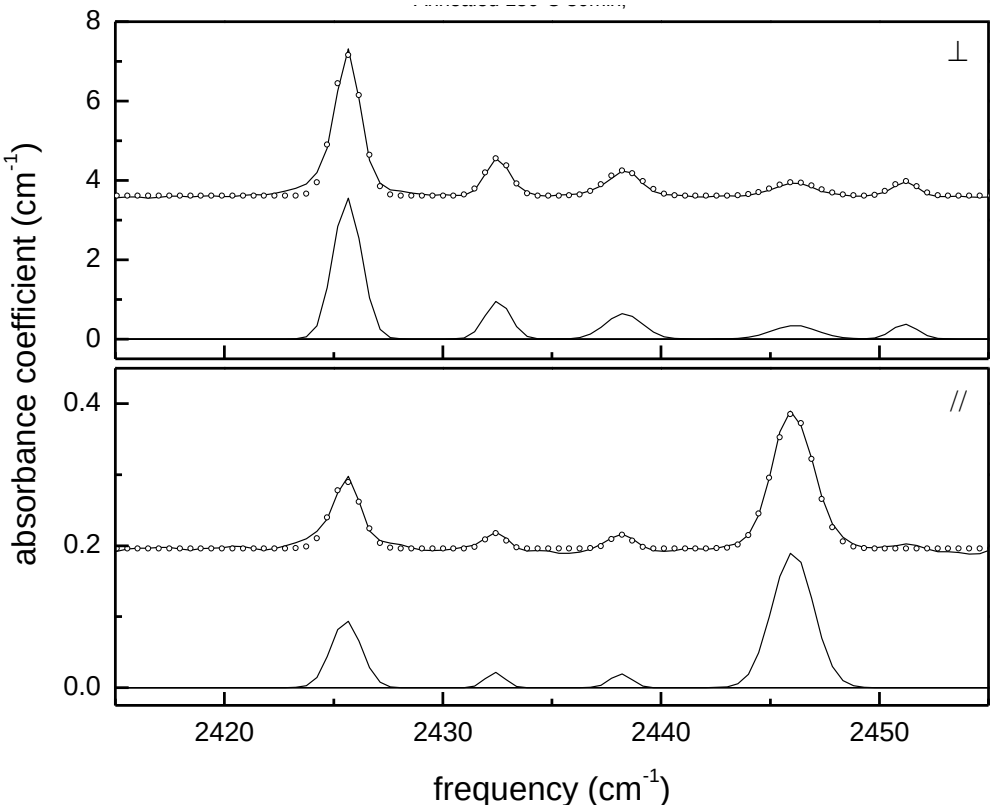

Fig. 3.14: Baseline corrected IR absorption spectra (T=4.2° K, resolution=1 cm^{-1}) focusing on O-D absorption lines of SnO_2 (treated in D_2 at 700°C for 30 min. and annealed for 30 minutes at 150°C in a He ambient) are shown for polarized light with vector **E**⊥**c** (upper) and **E**//**c** (lower). The positions and widths of individual absorption lines were determined by fitting the spectra with sums of Gaussian line shapes.

Perpendicular polarization

peak	**2425.6**	**2432.5**	**2438.5**	**2446.9**	**2451.3**
amplitude	3.561	0.957	0.639	0.341	0.376
FWHM	1.517	1.368	1.971	2.421	1.391
int. area	5.749	1.393	1.339	0.879	0.557

Parallel polarization

peak	**2425.6**	**2432.5**	**2438.5**	**2446.9**
amplitude	0.095	0.022	0.019	0.191
FWHM	1.619	1.034	1.146	2.220
int. area	0.163	0.024	0.024	0.451

Table 3.2: Frequencies, amplitudes, line widths, and integrated areas for O-D absorption lines of SnO_2 (treated in D_2 at 700°C for 30 min. and annealed for 30 minutes at 150°C in a He ambient) are listed for polarized light with vector **E**⊥**c** and **E**//**c**. Gaussian line shapes were used for these fits.

Distinctive polarization properties are also evident for the three lines at 2477.5, 2479.7, and, 2483.8 cm^{-1} (3334.2, 3339.0, and 3343.2 cm^{-1}) as is shown in Fig. 3.12. The lines at 2477.5 and 2483.8 cm^{-1} (3334.2 and 3343.2 cm^{-1}) have been assigned to $(O\text{-}D)_2$ $[(O\text{-}H)_2]$ complexes as was discussed above. The line at 2479.7 cm^{-1} (3339.0 cm^{-1}) corresponds to the O-D (O-H) mode of the dynamically decoupled (O-D—H –O) center. One of the lines arising from the $(O\text{-}D)_2$ complex, namely the 2477.5 cm^{-1} line [or 3334.2 cm^{-1} line for $(O\text{-}H)_2$] is detected only for **E//c**, while the other line, i.e. 2483.8 cm^{-1} (3343.2 cm^{-1}) is seen only for the **E**⊥**c** polarization,(neglecting the small peak observed for **E//c** due to the small deviation of the sample from perfect alignment). However, the intermediate line at 2479.7 cm^{-1} (3339.0 cm^{-1}) is seen for both polarizations. For the $(O\text{-}D)_2$ center, the different SnO_2 spectra were fit with

Gaussian line shapes. Fig. 3.15, Fig. 3.17, Table 3.3 and Table 3.5 show results for some of the fits generated for the $(O\text{-}D)_2$ center. For the $(O\text{-}H)_2$ center , Lorentzian line shapes were used to fit spectra. In this case, results are shown in Fig. 3.16, Fig. 3.18, Table 3.4 and Table 3.6.

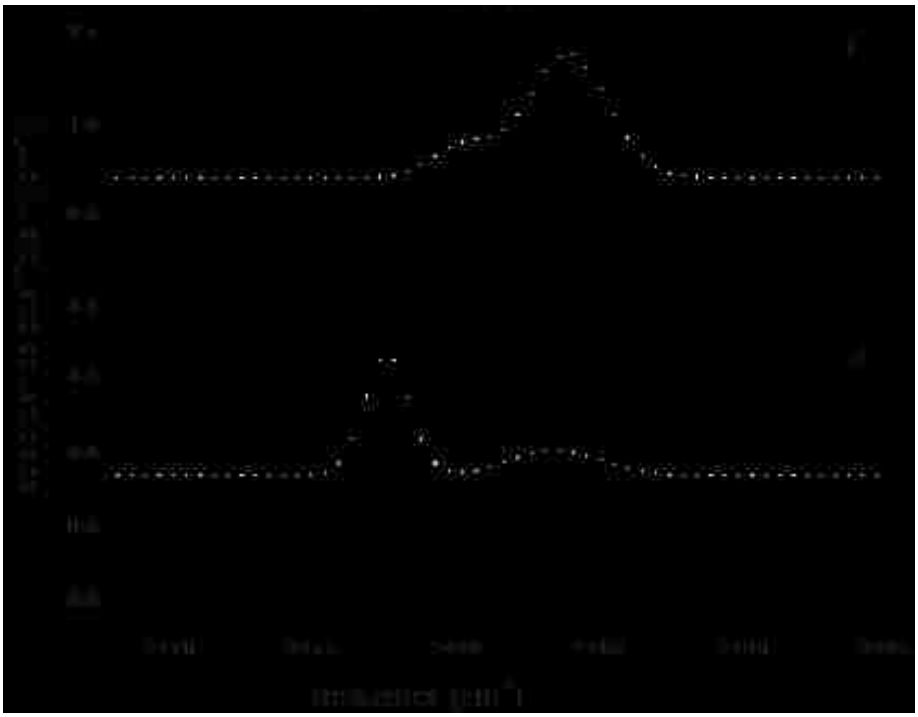

Fig. 3.15: Baseline corrected IR absorption spectra (T=4.2° K, resolution=1 cm^{-1}) focusing on the $(O\text{-}D)_2$ absorption lines of SnO_2 (primarily D_2) and annealed for 30 minutes at 150°C in a He ambient. Spectra are shown for polarized light with electric vector **E**$\perp$**c** (upper) and **E**//**c** (lower). The parameters for the individual absorption lines were determined by fitting the spectra with sums of Gaussian line shapes.

Perpendicular polarization

peak	**2480.2**	**2483.8**
amplitude	0.277	1.084
FWHM	2.887	3.298
int. area	0.734	3.805

Parallel polarization

peak	**2477.5**	**2483.4**
amplitude	0.487	0.101
FWHM	1.843	3.700
int. area	0.955	0.398

Table 3.3: Frequencies, amplitudes, line widths, and integrated areas for the $(O\text{-}D)_2$ absorption lines of SnO_2 (primarily D_2 and annealed for 30 minutes at 150°C in a He ambient) are shown for polarized light with electric vector **E**$\perp$**c** and **E**//**c** . Gaussian line shapes were used for these fits.

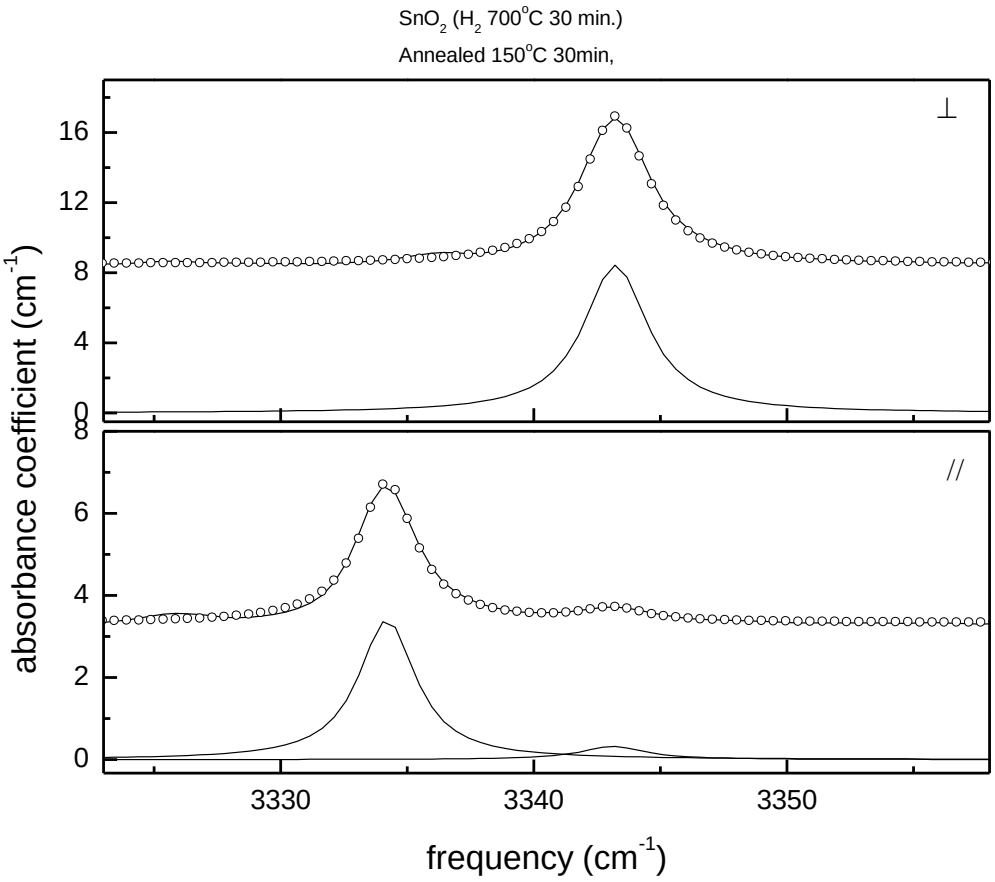

Fig. 3.16: Baseline corrected IR absorption spectra (T=4.2° K, resolution=1 cm^{-1}) focusing on the $(O\text{-}H)_2$ absorption lines of SnO_2 (H_2 at 700°C for 30 min. and then annealed for 30 minutes at 150°C in a He ambient) are shown for polarized light with electric vector **E**⊥**c** (upper) and **E**//**c** (lower). The individual absorption lines were determined by fitting the spectra with sums of Lorentzian line shapes.

Perpendicular polarization

peak	**3343.2**
amplitude	8.432
FWHM	3.089
int. area	38.860

Parallel polarization

peak	**3334.2**	**3343.2**
amplitude	3.406	0.318
FWHM	2.748	3.129
int. area	13.999	1.482

Table 3.4: Frequencies, amplitudes, line widths, and integrated areas for each of the O-H absorption lines of SnO_2 (treated in H_2 at 700°C for 30 min. and annealed for 30 minutes at 150°C in a He ambient) are shown for polarized light with electric vector **E**$\perp$**c** and **E//c**. Lorentzian line shapes were used for these fits.

From the combination of all of these fits, the intensity ratios of the parallel to perpendicular modes are determined to be

$$I_{//}(2477.5)\Big/I_{\perp}(2483.8) = I_{//}(3334.2)\Big/I_{\perp}(3343.2) = 0.306 \pm 0.05. \quad (3.3)$$

In a similar fashion, the ratios of the parallel to perpendicular components of the dynamically decoupled modes can be determined from Gaussian fits for O-D as shown in Fig. 3.17 and Table 3.5 and for O-H as shown in Fig. 3.18 and Table 3.6:

$$I_{//}(2479.7)\Big/ I_{\perp}(2479.7) = I_{//}(3339.0)\Big/ I_{\perp}(3339.0) = 0.4 \pm 0.1. \quad (3.4)$$

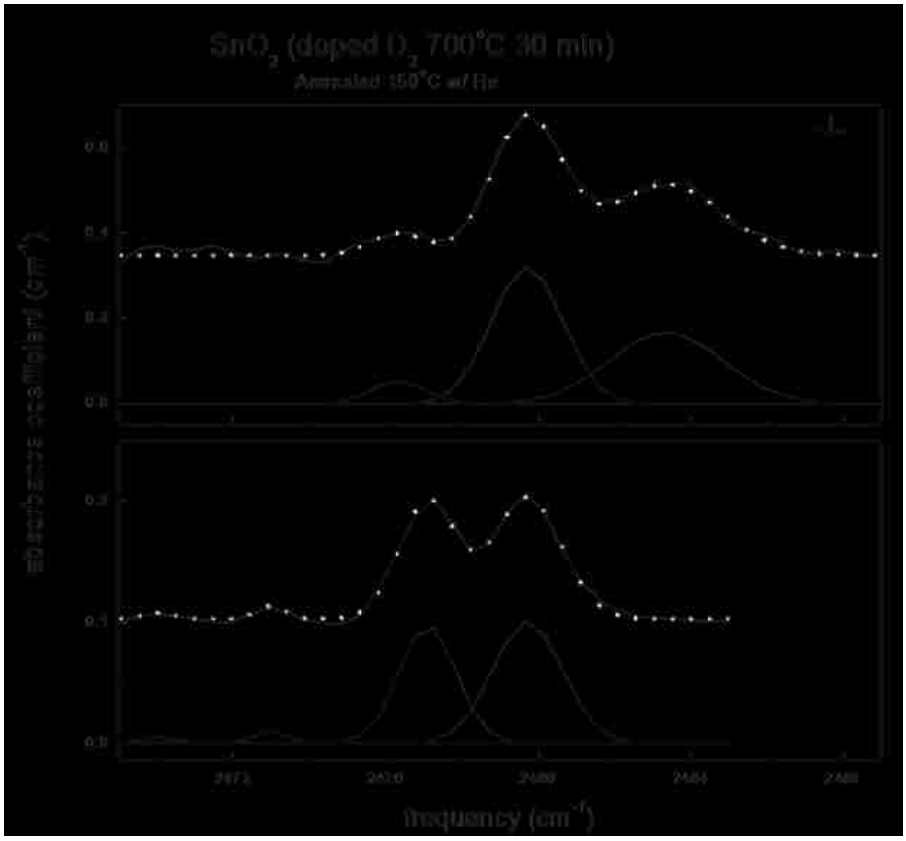

Fig. 3.17: Baseline corrected IR absorption spectra (T=4.2° K, resolution=1 cm^{-1}) focusing on the $(O\text{-}D)_2$ absorption lines of SnO_2 (D_2 at 700°C for 30 min. and annealed for 30 minutes at 150°C in a He ambient) are shown for both polarized light with electric vector **E**⊥**c** (upper) and **E**//**c** (lower). The parameters for the individual absorption lines were determined by fitting the spectra with sums of Gaussian line shapes.

Perpendicular polarization

peak	**2476.3**	**2479.7**	**2483.2**
amplitude	0.052	0.322	0.167
FWHM	1.677	2.169	3.476
int. area	0.093	0.743	0.61

Parallel polarization

peak	**2470**	**2473**	**2477.2**	**2479.7**
amplitude	0.005	0.011	0.098	0.101
FWHM	1.001	0.886	1.756	2.132
int. area	0.005	0.01	0.182	0.229

Table 3.5: Frequencies, amplitudes, line widths, and integrated areas for each of the O-D absorption lines for SnO_2 (treated in D_2 and annealed for 30 minutes at 150°C in a He ambient) are shown for polarized light with electric vector **E**$\perp$**c** and **E**//**c** . Gaussian line shapes were used for these fits.

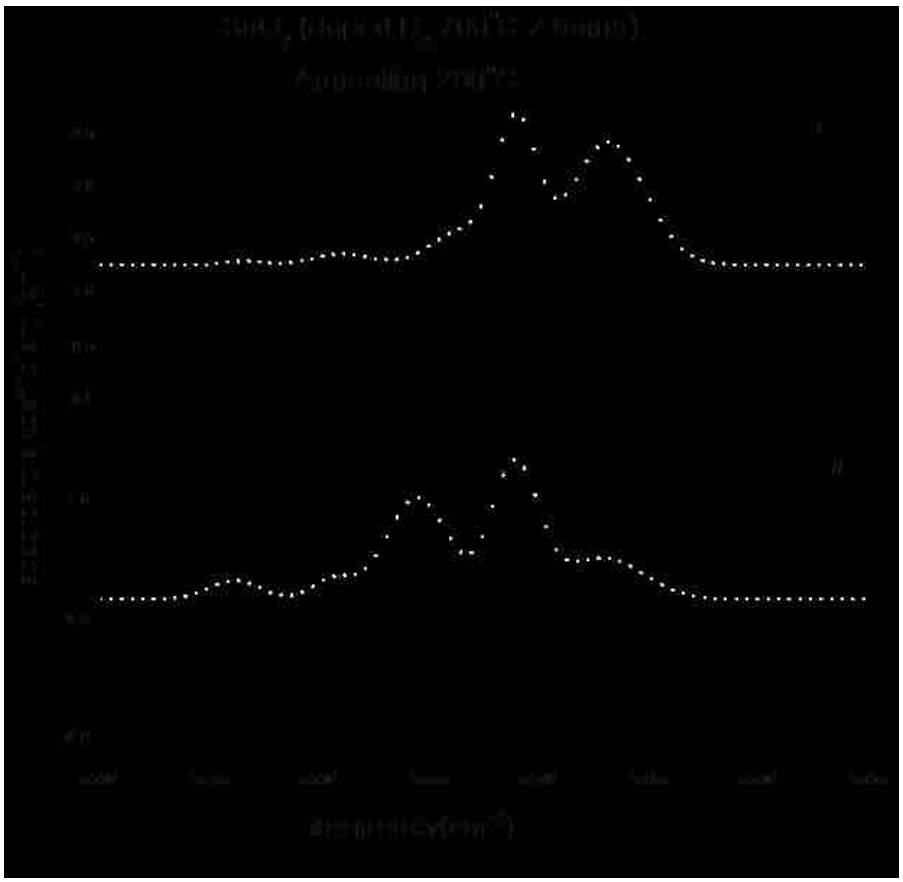

Fig. 3.18: Baseline corrected IR absorption spectra (T=4.2° K, resolution=1 cm^{-1}) focusing on the $(O\text{-}H)_2$ absorption lines of SnO_2 (D_2 at 700°C for 2 hours and annealed for 30 minutes at 200°C in a He ambient) are shown for polarized light with electric vector **E**$\perp$**c** (upper) and **E**//**c** (lower). The parameters for the individual absorption lines were determined by fitting the spectra with sums of Gaussian line shapes.

Perpendicular Polarization

peak	**3326.5**	**3331.1**	**3336.5**	**3339**	**3343.2**
amplitude	0.036	0.105	0.307	1.309	1.152
FWHM	2.141	3.051	3.323	2.208	3.937
int. area	0.083	0.341	1.086	3.075	4.825

Parallel polarization

peak	**3326.1**	**3330.6**	**3334.2**	**3339**	**3343.2**
amplitude	0.079	0.087	0.426	0.571	0.173
FWHM	2.704	2.19	3.305	2.52	4.331
int. area	0.227	0.202	1.499	1.532	0.797

Table 3.6: Frequencies, amplitudes, line widths, and integrated areas of the O-H absorption lines for SnO_2(treated in D_2 and annealed for 30 minutes at 200°C in a He ambient) are shown for polarized light with electric vector **E⊥c** and **E//c** . Gaussian line shapes were used to determine the parameters shown here.

From the rutile symmetry and the equivalence of different oxygen sites, the following equation relating the intensity ratio of parallel to perpendicular components to the angle between the O-D transition dipole with the c-axis (θ) can be used to determine bond angles:

$$I_{//}/I_{\perp} = 2\cot^2(\theta). \qquad (3.5)$$

For example, the O-D line at 2446.9 cm^{-1} was found to have a parallel to perpendicular intensity ratio of 0.54±0.05 which yields an O-D angle of 63° or (180°-63°)±1° from the c-axis.

Similarly, the O-D (O-H) bond angles for the $(O\text{-}D)_2$ ($(O\text{-}H)_2$) centers whose lines are at 2477.5 and 2483.8 cm^{-1} (3334.2 and 3343.2 cm^{-1}) were determined to be 69° or (180°-69°) ± 2°. The polarization ratios for the dynamically decoupled O-D and O-H modes of the (O-D—H-O) center at 2479.7 and 3339.0 cm^{-1} yield a bond angle of 66° or (180°-66°) ± 3°. As expected this result is consistent with the bond angle calculated for the $(O\text{-}D)_2$ complexes within experimental error.

A simple spring and mass analysis for the $(O\text{-}H)_2$ lines at 3334.2 and 3343.2 cm^{-1}, the corresponding $(O\text{-}D)_2$ lines at 2477.5 and 2483.8 cm^{-1}, and the intermediate lines at 2479.7 and 3339.0 cm^{-1} due to (O-H—D-O) center has been carried out considering only the harmonic part of the coupling force between the two (O-H) bonds. This is mainly due to the small experimental splitting that suggests a very small coupling force. However, anharmonicity is not completely negligible and it may be calculated from the isotopic data, using reduced diatomic masses. Then the 2x2 harmonic dynamical matrix was solved and the force constants were fit to the "harmonic experiment" after which the anharmonicity was added back. This analysis leads to conclusions which can be used as clues to the assignments and the structure of the $(O\text{-}H)_2$ defect and by extension some of the other (O-H) defects. These findings are as follows:

1) Since allowing the force constants of each (O-H) bond to differ worsens the experimental agreement, the two (O-H) bonds are taken to be equivalent.
2) The data can be fit to within 0.1 cm^{-1}, using one stretching and one coupling force constant.
3) The coupling force constant is very small, about 0.2% of the stretching force constant.

The polarization data and the theoretical calculations generate constraints on the possible defect models. For instance, for the $(O\text{-}H)_2$ case, the two O-H bonds are equivalent. Moreover, the perturbation of the O-H defect should cause only a modest displacement of the bond away from the normal to the c-axis.

As discussed earlier, the work by Hlaing Oo *et al.* [3.27] provided an analysis that preceded our polarization data. They suggested that the 3261.7 and 3281.8 cm^{-1} lines are associated with H trapped at a Sn vacancy. Two different types of O-H sites in this configuration are possible (named axial and equatorial) and were shown in Fig. 3.2 (c) and (d). Since the O-H bond perpendicular to the c-axis, i.e., the axial configuration, is calculated to be less stable than the equatorial configuration by ~0.1 eV, Hlaing Oo et al. [3.27] assigned the 3261.7 cm^{-1} line to the equatorial configuration and the 3281.8 cm^{-1} line to the axial one. No polarization data and an associated check of these assignments were present in this previous work. [3.27]

The experimental data generated using polarized light in our study does not support these assignments. First, the 3261.7 cm^{-1} line does not have a component in the IR spectra for **E//c**, suggesting that the bond lies in the axial direction. Conversely, the 3281.8 cm^{-1} line has components for both the **E⊥c** and **E//c** polarizations, therefore it could be a candidate for the equatorial configuration. Additionally, the assignment of H at a Sn vacancy is questionable for the equatorial configuration. A representation of a Sn vacancy within the SnO_2 rutile structure is shown in Fig. 3.19. When an H atom is trapped at this vacancy, the OH bond in the equatorial configuration would be expected to have an angle near the corresponding O-Sn direction, or ~30°-40° with the +c axis. Simulations using the CRYSTAL2006 [3.41] software

have been run to confirm this expectation by Prof. Fowler. Employing a Gaussian basis, DFT with B3LYP exchange-correlation method and using a 48 or 72 atom supercell, the results shown in Fig. 3.20 have been obtained for a single H atom trapped at a Sn vacancy and for two versions of two H atoms trapped at a Sn vacancy. These results confirm that lower than observed bond angles are predicted for such configurations. For this range of angles, the ratio of parallel to perpendicular polarization intensities would be around 3 to 6 from Eq. 3.5, which is about 6 to 12 times larger than observed value of 0.54 for the O-H line at 3281.8 cm^{-1} (and for the 2446.9 cm^{-1} line for O-D). The bond angle calculated from the observed polarization data is around 63° compared to ~30°-40° the expected for H at a Sn vacancy. Similar problems are also present for the assignment of the $(O\text{-}H)_2$ defects, for which the experimental data yield bond angles around 66°-69°. Therefore, we conclude that there is no spectroscopic evidence for the equatorial configuration of an O-H center or for an $(O\text{-}H)_2$ defect associated with a Sn vacancy. However, the axial configuration of O-H associated with a Sn vacancy could be the origin of one of the observed transitions with polarization perpendicular to c. This could be one of the lines still unassigned in the spectrum for $\mathbf{E}\perp\mathbf{c}$.

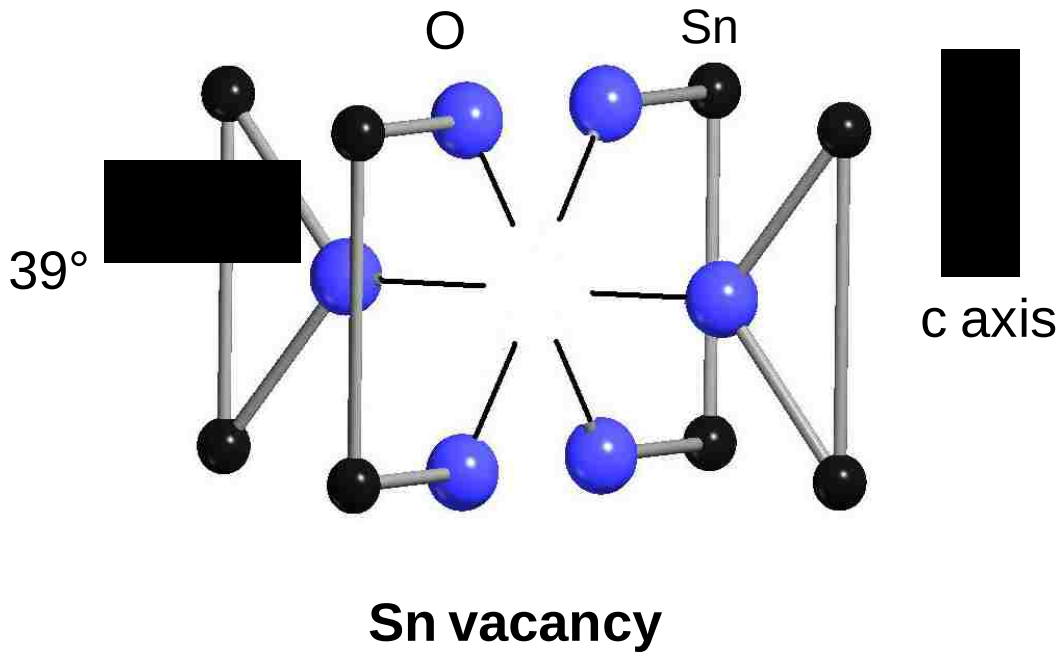

Fig. 3.19: Schematic portion of SnO_2 containing a Sn vacancy, drawn using Moldraw [3.7]. Compliments of W. B. Fowler.

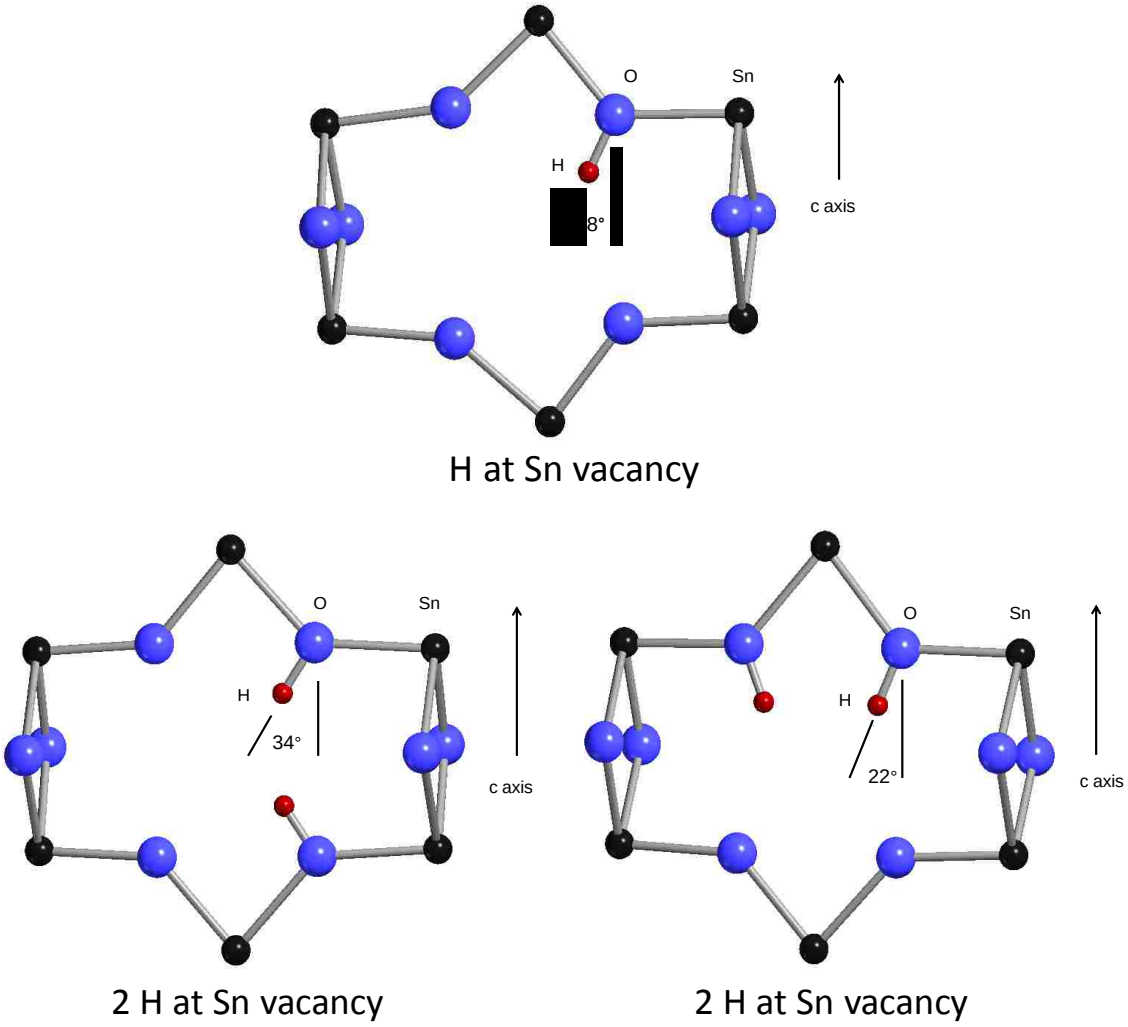

Fig. 3.20: The different configurations of SnO_2 with a single H trapped at a Sn vacancy and with two versions of two H atoms trapped at a Sn vacancy, drawn using Moldraw [3.7]. Compliments of W.B. Fowler.

Fowler's analysis was not limited to a Sn vacancy, but was continued for other lattice defects. In the rutile lattice, one or two interstitial H atoms attached to one or two O atoms near a Sn interstial could satisfy the symmetry requirements discussed earlier. The rutile structure with a Sn interstitial is shown in Fig. 3.21**.** Three of the oxygen atoms which are near

the interstitial Sn were labeled and colored differently to help discuss some of the possible configurations. If a single H atom is attached to O(1) with the same c-axis value as interstitial Sn, this configuration would have only a component for **E⊥c** and could be the origin of the O-H line at 3261.5 cm^{-1} (2425.7 cm^{-1} line for O-D). If the hydrogen is attached to O(2) or O(3), the symmetry breaking due to the presence of the Sn interstitial could lead to a small relaxation of the H along the c-direction, yielding IR components for both **E⊥c** and **E//c**. The line at 3281.8 cm^{-1} (2446.9 cm^{-1}) could arise from this configuration. Moreover, one H atom can attach to O(2) and another to O(3) to form the $(O\text{-}H)_2$ complex with a c-axis relaxation, i.e., this configuration would have components for both polarizations. This would correspond to the lines in the 3340 cm^{-1} (2480 cm^{-1}) region. Other two H defects involving more distant O atoms might also exist.

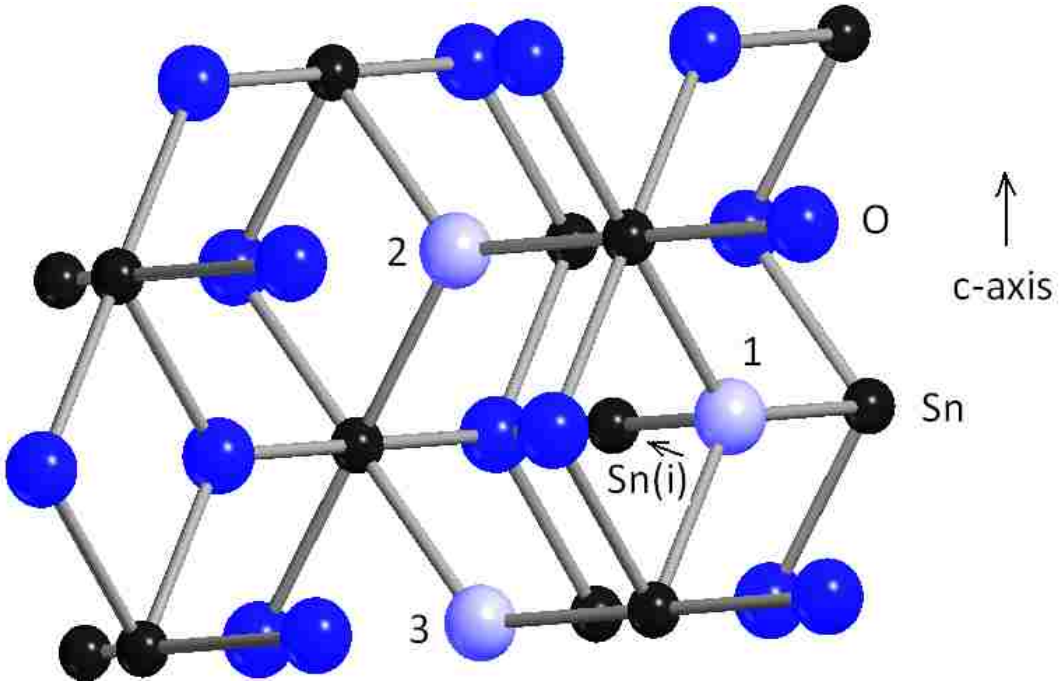

Fig. 3.21: Schematic portion of SnO_2 containing a Sn interstitial. Special neighboring oxygens [possible oxygens that H could attach to make (O-H) or $(O-H)_2$ centers] are labeled 1-3, drawn using Moldraw [3.7, 3.40].

Finally, another possible defect satisfying the constraints imposed by the polarization data should be mentioned here. Hydrogens trapped near a substitutional or an interstitial impurity metal atom can also be considered even though we believe it is unlikely to be an alternative. This is mainly due to very similar IR spectra obtained for samples from very different sources [3.27, 3.42]. Secondly, impurities associated with O-H bands in cassiterite [3.43] lead to absorption bands that are absent in our samples. However, this possibility cannot be completely ruled out.

3.4.5 Sources and sinks for hydrogen

Our IR data provide us with clues that there are hydrogen centers (a hidden source of hydrogen) in as-grown SnO_2 samples that do not give rise to free carrier absorption or electrically active shallow donors. In Fig. 3.3, spectrum (ii), when an as-grown sample was annealed in a He ambient and quenched, a small concentration of an electrically active shallow donor (H_i) was produced. Annealing an as-grown sample in an H_2 ambient produced H_i, H_o, and other O-H centers throughout the sample bulk as shown in Fig. 3.3, spectrum (iv). Moreover, annealing an as-grown sample in a D_2 ambient produced both O-D and O-H centers together throughout the sample bulk shown in Fig. 3.3, spectrum (v), even though hydrogen was not introduced deliberately. In order to better understand this interesting result, another sample was prepared by annealing an as-grown SnO_2 sample in a He ambient at 1100°C for 5h to remove hydrogen completely throughout the bulk and by subsequently annealing in a D_2 ambient. The resulting spectrum shown in Fig. 3.3, spectrum (iii), contains only O-D centers and not O-H centers. These results show that H is already present in our as-grown SnO_2 samples due to crystal growth and this H can be converted into shallow donors and O-H centers by heat treatments. In other words, there is a reservoir of electrically inactive hydrogen in as-grown samples. Moreover, annealing in a D_2 ambient demonstrates the dual role played by the damaging anneal as both a source of native defects that form the defect centers seen in our experiments and as a source of deuterium.

H_o was suggested as a possible source of hidden hydrogen in SnO_2 samples by Hlaing Oo *et al.* [3.27]. However, H_o cannot serve as a reservoir of hydrogen in our samples due to its electrical activity which gives rise to strong free carrier absorption. Instead our results reveal

that the O-H complex with an IR line at 3261 cm^{-1} is an attractive candidate as a source of H because it is already present in the sample and does not give rise to free carrier absorption. Other O-H centers are not prominent in as-grown samples. Despite the fact that a high formation energy is theoretically predicted for H_2 in SnO_2 [3.27], our data suggest that H_2 is another possible source of hidden hydrogen because it is electrically inactive and does not give rise to free carrier absorption or O-H vibrational lines, similar to the role played by H_2 in ZnO [3.29-3.30].

Our data show that H or D can be exchanged between H- or D- containing centers when samples are treated at elevated temperatures. H centers that give rise to electrically active shallow donors can be converted to centers that do not and vice versa. This is shown in Fig. 3.7-Fig. 3.11. For instance, the IR lines at 3281.8, 3334.2, and 3343.2 cm^{-1}, increase in intensity when the 3156 cm^{-1} line assigned to H_i disappears during long storage times at room temperature (Fig. 3.10, Fig. 3.11). Moreover, during the same period, the intensity of the line at 3261.5 cm^{-1} decreases as does the free carrier absorption. Recall that the 3281.8 and 3261.5 cm^{-1} lines were assigned to O-H centers while the 3334.2 and 3343.2 cm^{-1} lines correspond to $(O\text{-}H)_2$ complexes. When the sample that underwent a long storage time was re-annealed at 500°C in a He ambient and quenched, H_i recovered at the expense of the H trapped in other $(O\text{-}H)_n$ complexes as seen in Fig. 3.10. Moreover, the free carrier absorption was also recovered [Fig. 3.10 and Fig. 3.11 (bottom)] and the line at 3261.5 cm^{-1} regained its intensity (Fig. 3.10). According to these observations, an exchange of H between H_i and $(O\text{-}H)_n$ centers can occur. H_i migrates to be trapped by a native defect to form the 3281.8 cm^{-1} line during a long storage time at room temperature or by annealing at around 100-150°C. Additionally, the

intensity decrease for the 3261.5 cm^{-1} line of an (O-H) center is correlated with the intensity increase for the lines at 3334.2 and 3343.2 cm^{-1} that correspond to $(O\text{-}H)_2$ complexes. This suggests that the O-H center traps an additional H atom (that is found to be unstable at around room temperature) to form the $(O\text{-}H)_2$ center upon annealing or for long storage time. Both of these processes can be reversed, i.e., H_i from these defects can be released upon annealing at elevated temperature and this H_i can be frozen in as an isolated interstitial donor when the sample is quenched to room temperature.

Although the more thermally stable shallow donor that has been proposed to be due to H_O is not directly detectable by IR vibrational spectroscopy, our data show that it can also be converted to other defects upon annealing. This can be studied by investigating the behavior of the free carrier absorption and some of the O-H lines. As shown in Fig. 3.9, the free carrier absorption due to H_o is almost completely annealed away at 600°C while the intensities of the lines at 3156.1 cm^{-1} (H_i) and 3261.5 cm^{-1} (O-H) grow, suggesting that the exchange of H between H_o and these centers can occur.

3.5 Conclusion

Hydrogen and deuterium centers in rutile single-crystal SnO_2 have been investigated by infrared vibrational spectroscopy. Annealing as-grown SnO_2 samples in an H_2 ambient at elevated temperature gives rise to O-H vibrational lines along with the broad low frequency absorption that is the characteristic of free carriers. This annealing treatment strongly affects the conductivity of the sample because it produces the hydrogen and native defects that form shallow donors and O-H centers throughout the bulk of the SnO_2 sample. Surprisingly,

annealing an as-grown SnO_2 sample in D_2 ambient introduces not only O-D centers but also O-H centers together with free carrier absorption. The cause is that the electrically inactive hydrogen that is already present in the as-grown sample (because of the growth procedure) interacts with native defects and gives rise to O-H centers and shallow donors during the heat treatment. In summary, the introduction of hydrogen or deuterium into as grown SnO_2 samples produces shallow donors.

By investigating the thermal stabilities of the various H-containing defects and their relationship with the free carriers which are introduced by shallow donors, the role hydrogen plays as a cause of conductivity in SnO_2 has been studied. The annealing behaviors of the free carriers and O-H IR absorption show that two H-related donors that give rise to free carriers are present. The first one is marginally stable at room temperature and corresponds to around 35% of the free carriers. The O-H line at 3156.1 cm^{-1} was previously assigned to H_i and was concluded to be the less stable shallow donor by Hlaing Oo *et al*. [3.27]. Our experimental results strongly support this assignment due to the thermal stability properties and relationship of the 3156 cm^{-1} line to the free carrier absorption. A second shallow donor is assigned to H_o that is a more thermally stable donor (up to near 600°C) and is responsible for about 65% of the free carriers. H_o cannot be detected by vibrational spectroscopy, but this assignment is consistent with theory [3.15, 3.27].

Studying the annealing behavior and unique polarization properties of hydrogenated or deuterated SnO_2 samples has yielded important clues about the structures and chemical reactions of several O-H centers. Upon thermal treatment, additional O-H and $(O\text{-}H)_2$ centers that do not give rise to free carriers are also observed. It is found that an inter-conversion

between these electrically inactive centers and H-related shallow donors can occur. Therefore, the conductivity of a hydrogenated sample is highly sensitive to its thermal history.

Several O-H and $(O\text{-}H)_2$ centers have been found to have distinctive polarization properties, which led to structure-sensitive tests of proposed microscopic models. Theoretical work by Prof. Fowler that complemented our polarization data suggested that some of the previously proposed models are not consistent with experimental data and suggested new, consistent configurations. For example, the previous assignment of the line at 3281.8 cm^{-1} to H being trapped at an Sn vacancy and with an axial configuration [3.27] did not agree with our polarization data and bond angle calculations. Instead, it was proposed to be due to H being trapped next to an interstitial Sn atom with some relaxation from the normal to the c-axis. Similar proposals backed by theory were made for the 3334.2 and 3343.2 cm^{-1} lines. They were assigned to an $(O\text{-}H)_2$ center trapped by insterstitial Sn. The IR line at 3339.0 cm^{-1} was determined to be due to the same center except that one of the H atoms was replaced with a D atom to form a (O-H—D-O) center.

REFERENCES

[3.1]. M. Batzill and U. Diebold, Prog. Surf. Sci.,**79**, (2005)

[3.2]. A. A. Bolzan, C. Fong, B. J. Kennedy, and C. J. Howard, Acta Cryst. **B53**, 373, (1997).

[3.3]. R. E. Presley, C. L. Munsee, C-H. Park, D. Hong, J. F. Wager, and D. A. Keszler, J. Phys. D, **37**, (2004).

[3.4]. R. G. Gordon, MRS Bull., **25**(8), (2000).

[3.5]. W. Gopel and K. D. Schierbaum, Sens. Actuators, **B 26-27**,(1995).

[3.6]. Z. M. Jarzebski and J. P. Morton, J. Electrochem. Soc., 123, 229C, (1976).xxx

[3.7]. P. Ugliengo, D. Viterbo, and G. Chiari, Z. Kristallogr. **207**, 9 (1993).

[3.8]. H. L. Hartnagel, A. L. Dawar, A. K. Jain, C. Jagadish, *Semiconducting Transparent Thin Films* (Institute of Physics, London, 1995).

[3.9]. *Transparent Electronics: From Synthesis to Applications*, edited by A. Facchetti and T. Marks (Wiley, New York, 2010).

[3.10]. C. Kiliç and A. Zunger, Phys. Rev. Lett. **88**, 095501, (2002).

[3.11]. P. Ágoston, K. Albe, R. Nieminen, and M. Puska, Phys. Rev. Lett. **103**, 245501, (2009).

[3.12]. C. G. Van de Walle, Phys. Rev. Lett. **85**, 1012, (2000).

[3.13]. A. Janotti and C. G. Van de Walle, Nature Materials **6**, 44, (2007).

[3.14]. C. Kiliç and A. Zunger, Appl. Phys. Lett. **81**, 73 (2002).

[3.15]. A. K. Singh, A. Janotti, M. Scheffler, C. G. Van de Walle, Phys. Rev. Lett. **101**, 055502, (2008).

[3.16]. S. Limpijumnong, P. Reunchan, A. Janotti, and C. G. Van de Walle, Phys. Rev. B **80**, 193202, (2009).

[3.17]. E. Mollwo, Z. Phys. **138**, 478 (1954); G. Heiland, E. Mollwo, and F. Stöckman, in *Solid State Physics*, edited by F. Seitz and D. Turnbull (Academic Press, New York, 1959) Vol. 8, p. 193.

[3.18]. D. G. Thomas and J. J. Lander, J. Chem. Phys. **25**, 1136, (1956).

[3.19]. A. R. Hutson, Phys. Rev. **108**, 222, (1957).

[3.20]. E. V. Lavrov, F. Herklotz, and J. Weber, Phys. Rev. B **79**, 165210 (2009).

[3.21]. E. V. Lavrov, J. Weber, F. Börnert, C. G. Van de Walle, and R. Helbig, Phys. Rev. B **66**, 165205 (2002).

[3.22]. S. Samson and C. G. Fonstad, J. Appl. Phys. **44**, 4618, (1973).

[3.23]. R. S. Katiyar, P. Dawson, M. M. Hargreave, G. R. Wilkinson, J. Phys. C: Solid St. Phys. **4**, 2421, (1971).

[3.24]. A. Beran and J. Zemann, Tschermaks Min. Petr. Mitt. **15**, 71, (1971).

[3.25]. F. Bréhat, B. Wyncke, J.M. Léonard and Y. Dusausoy, Phys. Chem. Minerals **17**, 191, (1990).

[3.26]. J. Maldener, F. Rauch, M. Gavranic, and A. Beran, Mineral. Petrol. **71**, 21, (2001).

[3.27]. W. M. Hlaing Oo. S. Tabatabaei, M. D. McCluskey, J. B. Varley, A. Janotti, and C. G. Van de Walle, Phys. Rev. B **82**, 193201, (2010).

[3.28]. G. A. Shi, M. Stavola, S. J. Pearton, M. Thieme, E. V. Lavrov, and J. Weber, Phys. Rev. B **72**,195211 (2005).

[3.29]. G. A. Shi, M. Saboktakin, M. Stavola, and S. J. Pearton, Appl. Phys. Lett. **85**, 5601 (2004).

[3.30]. E. V. Lavrov, F. Herklotz, and J. Weber, Phys. Rev. Lett. **102**, 185502 (2009).

[3.31]. B. Thiel and R. Helbig, J. Crystal Growth **32**, 259 (1976).

[3.32]. P. Y. Yu and M. Cardona, *Fundamentals of Semiconductors* (Springer, Berlin, 1996).

[3.33]. D. G. Thomas, J. Phys. Chem. Solids **10**, 47, (1959).

[3.34]. C. H. Seager and S. M. Myers, J. Appl. Phys. **94**, 2888, (2003).

[3.35]. Z. M. Jarzebski and J. P. Marton, J. Electrochem. Soc. **123**, 299C, (1976).

[3.36]. S. J. Pearton, D. P. Norton, K. Ip, and Y. W. Heo, J. Vac. Sci. Technol. B **22**, 932 (2004).

[3.37]. C. Klingshirn, Phys. Stat. Sol. (b) **244**, 3027 (2007).

[3.38]. J. B. Varley, A. Janotti, A. K. Singh, and C. G. Van de Walle, Phys. Rev. B **78**, 245206, (2009).

[3.39]. G. A. Shi, *Physics of H in ZnO and H_2 in Si from Vibrational Spectroscopy*, Lehigh University, (2006).

[3.40]. F. Bekisli, W. B. Fowler, M. Stavola, Lynn A. Boatner, Erik Spahr, and Gunter Lüpke, Phys. Rev. B 85, 205202, (2012).

[3.41]. R. Dovesi, V. R. Saunders, C. Roetti, R. Orlando, C. M. Zicovich-Wilson, F. Pascale, B. Civalleri, K. Doll, N. M. Harrison, I. J. Bush, Ph. D'Arco, M. Llunell, ***Crystal06 User's Manual***, University of Torino, Torino, 2006.

[3.42]. F. Bekisli, M. Stavola, W. B. Fowler, L. Boatner, E. J. Spahr, and G. Lüpke, Phys. Rev. B **84**, 035213 (2011).

[3.43]. Z. Losos and A. Beran, Mineral Petrol **81**, 219 (2004).

Chapter 4

FTIR Spectroscopy of O-H and O-D centers in TiO_2

4.1 Introduction

In this chapter, studies of hydrogen related defects within the rutile TiO_2 structure will be presented. TiO_2 is of particular interest because it has received attention from many application areas, such as optics, electronics and energy efficiency [4.1-4.2]. Furthermore, the effect of impurities on the electrical and chemical properties is known to be critical for many of these applications. For instance, the n-type conductivity that this material typically exhibits has been traditionally attributed to native defects. Another reason for the selection of TiO_2 is because of the differences between the findings of two previous studies of the interstitial hydrogen atom in TiO_2. These differences will be explained and analyzed in the following paragraphs after a brief introduction to the rutile TiO_2 structure and hydrogen-related defects in TiO_2.

Rutile TiO_2 has six fold coordinated Ti and 3 fold coordinated oxygen atoms as seen in Fig. 4.1. Interstitial hydrogen (H_i) in TiO_2 has unique properties that have been studied over many years. Researchers have obtained several significant results: (1) H_i attaches to a single lattice O such that the O-H bond lies at (1/2, 0, 0) which is perpendicular to the [001] c-axis of the rutile lattice [4.3-4.4]. (2) The diffusion of H_i in TiO_2 involves hydrogen jumps from one oxygen atom to another along the c-direction, which makes the existence of hydrogen at room temperature puzzling [4.5-4.7]. (3) IR measurements reveal that TiO_2 shows strong OH, OD and

OT stretching modes (D and T being the isotopic siblings of H) with unusually large anharmonicity [4.8].

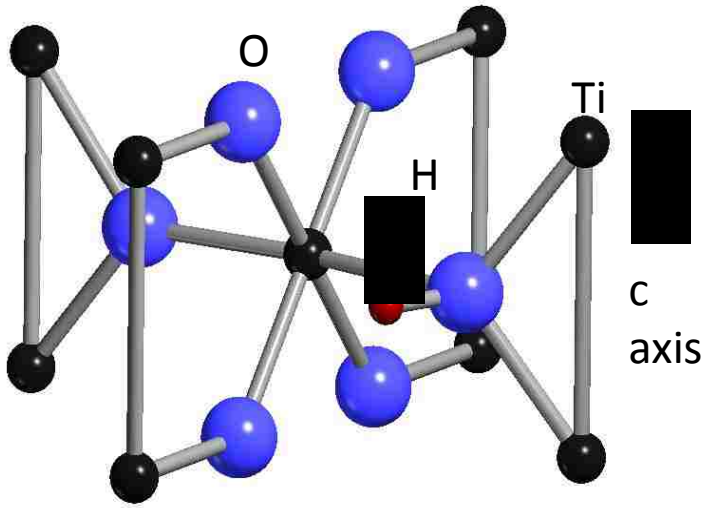

Fig. 4.1: Rutile lattice structure of TiO_2 with O-H bond.

Furthermore, recent Electron Paramagnetic Resonance (EPR) experiments on neutral H_i, as well as on F substituting for O in mildly reduced TiO_2, show a characteristic that is unusual in most materials, especially semiconductors: the spin associated with the unpaired electron in each case is localized on a single Ti, rather than being spread out over many sites [4.9-4.10]. In another important study performed by Bates and Perkins in the 1970s [4.8], OD, OH and also OT infrared vibrational modes were analyzed. It was found that each of these bonds generated a single, sharp and strongly polarized line with E⊥c at 2445 cm^{-1}, 3286 cm^{-1}, and 2071 cm^{-1} for OD, OH and OT, respectively, as seen in Fig. 4.2. Also, they reported no evidence that these centers were shallow donors.

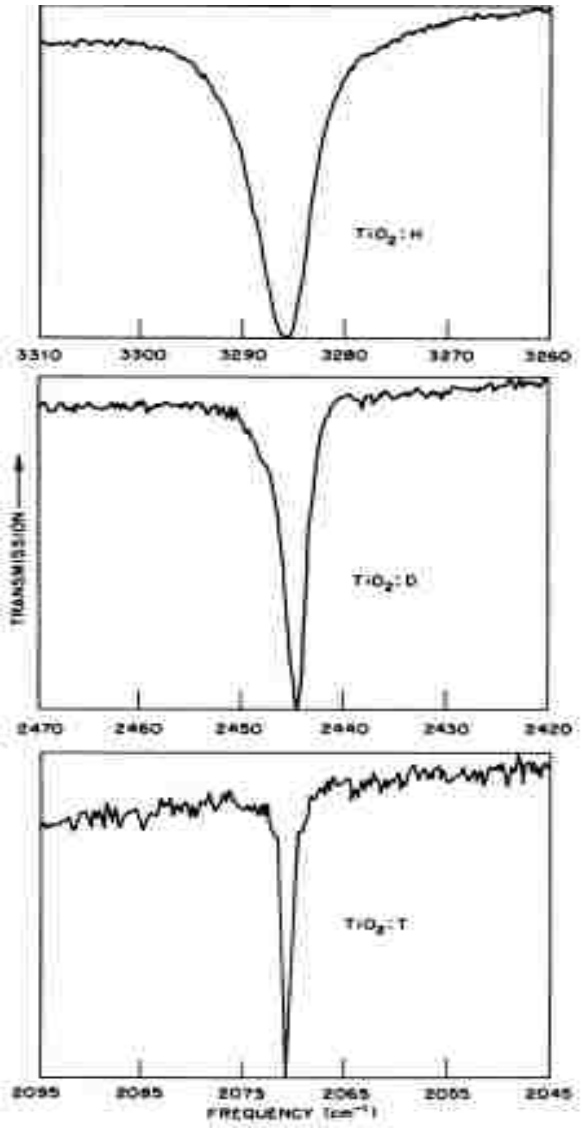

Fig. 4.2: Infrared stretching modes of OH, OD, and OT in TiO_2 measured at 77 K [4.8].

However, in a recent study [4.11] performed by Herklotz *et al.*, a very different story was told and the differences mentioned above were established. In recent experiments, instead of a single, sharp IR line, three closely spaced and overlapping lines were detected at 2445.0, 2445.7, 2447.8 cm^{-1} for the OD center. These lines were assigned to different charge states of

the same defect, namely the ground and excited vibrational modes of the neutral state and also a vibrational mode for a positive charge state. The relative intensities of these lines were found to be strongly dependent on temperature as is shown in Fig. 4.3. Herklotz *et al.* also observed that above 20 K, the neutral state intensity was decreased while the positive state intensity was increased as is shown in Fig. 4.4 (a). This observation supported the idea that different charge states were associated with the same defect. Moreover, they correlated the intensity change of the OD (and OH) centers to the temperature dependence of an additional broad absorption that was attributed to free carriers [4.12].This correlation is shown in Fig. 4.4 (b). In this figure, the strength of the free carrier absorption is plotted vs temperature, and a significant increase becomes apparent above 20 K, similar to the appearance of the positive charge state. Based on these data, Herklotz *et al.* assigned these OH and OD centers to shallow donors and the multiline structure to its two different charge states.

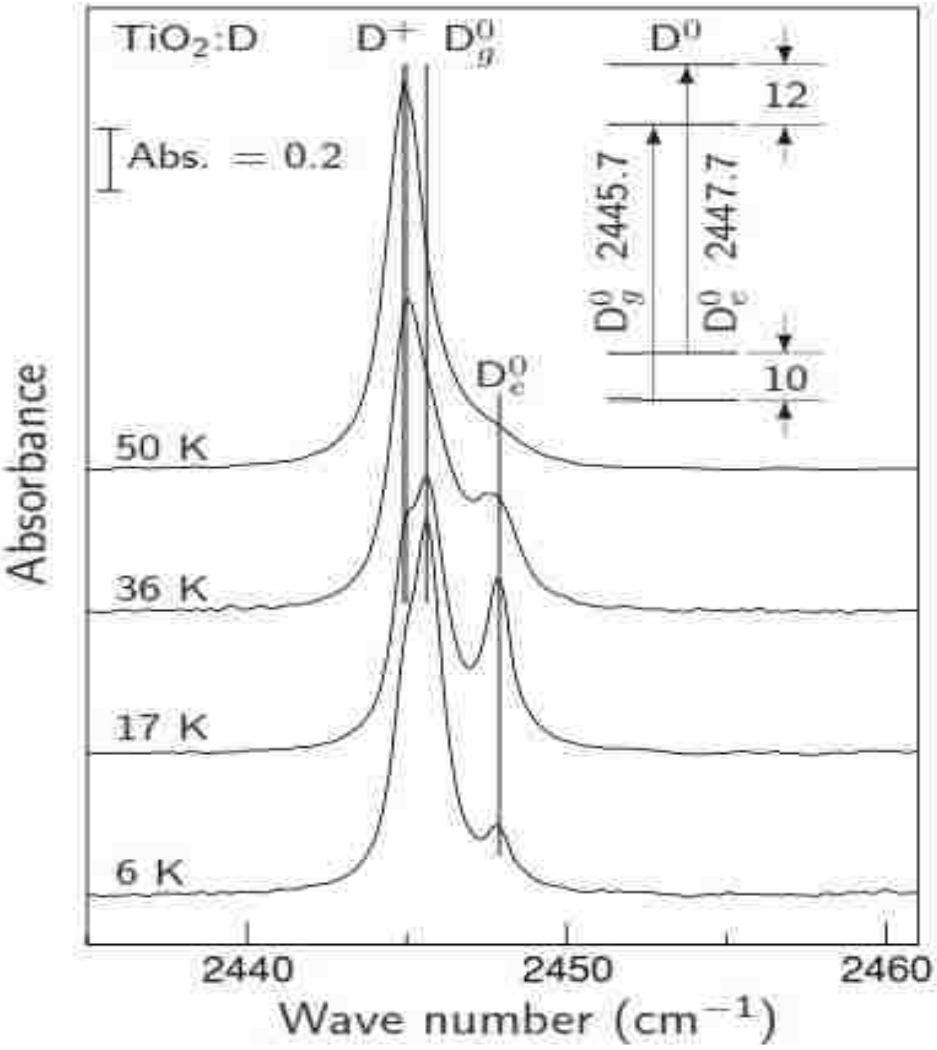

Fig. 4.3: IR absoption spectra of deuterium treated TiO_2 (resolution= 0.2 cm^{-1}) meausured with unpolarized light at different temperatures. The energy diagram for the neutral charge state is shown in the inset [4.11].

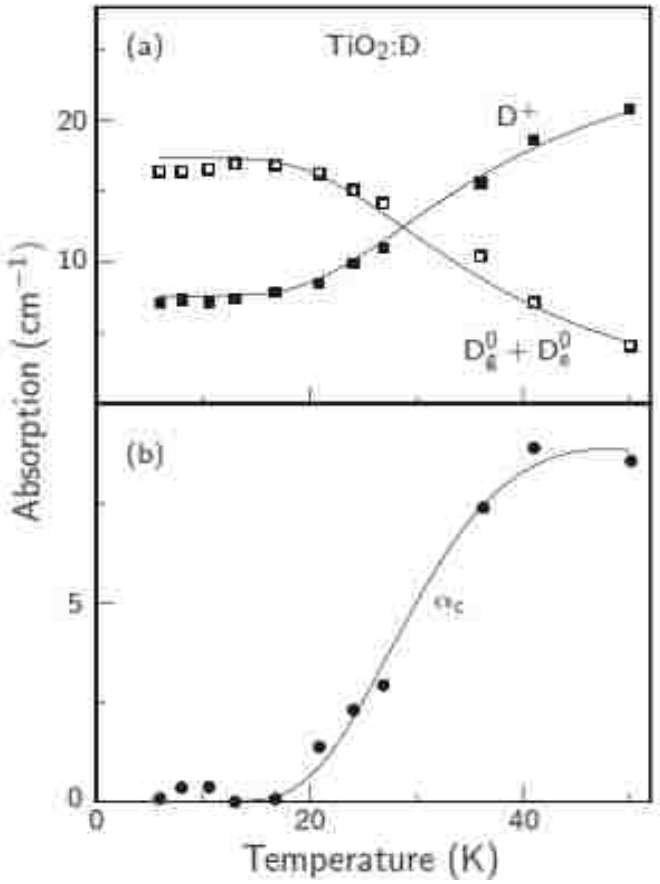

Fig. 4.4: (a) IR absorption of neutral and positive charge states vs temperature for the O-D center in TiO_2. (b) The free carrier absorption vs temperature. Points are experimental data and solid lines are the best-fit curves to the experimental data [4.11].

In order to answer the questions related to the OH and OD stretching modes raised by these previous studies, we have performed further experimental and theoretical studies. In the following sections, the OH and OD centers in TiO_2 will be investigated but the OD center will be studied more intensely than the OH center because the IR lines for OD are sharper and reveal greater detail.

We will begin with high-resolution vibrational spectroscopy performed as a function of temperature to gain insight into the different vibrational properties seen for OD in TiO_2 in the 1970's and in recent studies and into how these results might be interpreted.

4.2 Experimental Set-up and Samples

Hydrogen and deuterium in TiO_2 have been studied experimentally using IR vibrational spectroscopy. The rutile phase TiO_2 samples used in our experiments were obtained from different sources. Some of our samples were provided by Commercial Crystal Laboratories. Fortunately, we are also in possession of the very samples, grown by the National Lead Co., studied by Bates and Perkins in the 1970s [4.8]. These samples are approximately 2 mm thick disks with faces parallel to the (100) plane. For the experiments of Bates and Perkins, the samples were given the following thermal and chemical treatments. Crystal growth was induced by flame fusion in the presence of water vapor and was the reason for the presence of a high concentration of OH centers in these samples. Thus, OH centers in as-grown material were studied by Bates and Perkins without additional treatment with H_2. However, for deuterium treatments, disks were heated for 5h in the pressure of about 0.4 atm of D_2 gas at 600°C. Then the samples were subsequently heated for 2 h at 800°C in a flowing stream of oxygen to restore their transparency. This was the condition of the TiO_2 samples prior to starting our own experiments.

In order to introduce deuterium in our measurements, TiO_2 samples from both sources were placed in sealed quartz ampoules with 2/3 atm of D_2 gas at room temperature and annealed at elevated temperature (at 500°C for 4 h). The treatments in D_2 were terminated by

quenching the ampoule to room temperature in water to complete the annealing. Subsequent anneals were performed in a tube furnace either in flowing N_2 or in air and terminated by quenching the sample in water.

IR absorption spectra were measured with a Bomem DA3.16 Fourier transform infrared spectrometer. Light was polarized with a wire grid polarizer that was placed after the sample. O-H and O-D vibrational stretching modes for TiO_2 samples were measured between 4 K and 60 K with an InSb detector. Samples were cooled by an Oxford Instruments CF1204 cryostat with He contact gas in order to make precise temperature dependent measurements.

4.3 Experimental Results and Discussion

4.3.1 O-D stretching vibrational mode

We started our experiments with TiO_2 samples taken from the collection that had been prepared by Bates and Perkins [4.8]. These samples were stored in dated sample boxes from the 1970's. Initial measurements were performed without any additional annealing treatments. IR measurements in the OD range at various temperatures revealed two different results. The upper spectra in Fig. 4.5 show the same single sharp line at 2445.0 cm^{-1} that was observed by Bates and Perkins [4.8]. However, the lower spectra show the same multi-line structure that was observed by Herklotz *et al.* [4.11]. Experimental results measured at 4 K and 17 K are compared in Fig. 4.5 because these temperatures reveal the changes in the multi-line structure more clearly.

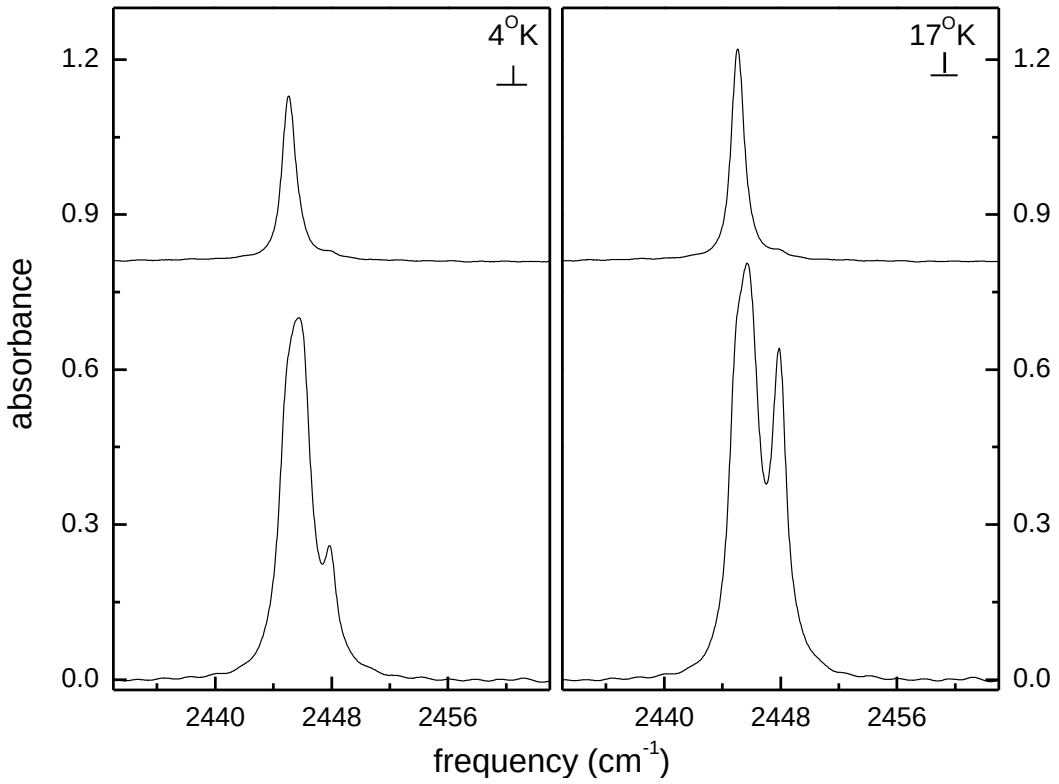

Fig. 4.5: IR absorption spectra (T= 4 K and 17 K, resolution= 0.1 cm^{-1}, [100] optical viewing direction) measured with **E⊥c** for TiO_2 samples prepared by Bates and Perkins [4.8]. The samples were reported to have been deuterated by annealing in a D_2 ambient (5 h at 600 °C) followed by an anneal in flowing oxygen (2 h at 800 °C). The upper and lower spectra represent two different samples from that collection.

These surprising results motivated further investigations to understand the reason behind this variation. In order to detect the cause of this behavior, the samples from Commercial Crystal Laboratories were prepared in our lab for further experiments. Fig. 4.6 shows the IR spectra for one of these TiO_2 samples. The lower spectrum in this figure was obtained from the sample which was treated in D_2 gas for 4 hrs at 500°C and immediately

quenched to room temperature. The partially resolved multiline structure for the OD center is observed clearly. The sample was also observed to be made blue in color by the treatment, as also witnessed in other studies [4.13-4.14]. The upper spectrum, on the other hand, tells a different story. In this case, the sample used to generate the lower spectrum was subsequently annealed in air at 500°C for 30 mins after the D_2 treatment. In addition to obtaining a single, sharp IR line at 2445.0 cm^{-1}, similar to the results of Bates and Perkins, the blue color also disappeared, restoring the sample's visible transparency. Similar results have been obtained using samples from both of our sources, i.e., the collection of Bates and Perkins and the samples from Commercial Crystal Laboratories.

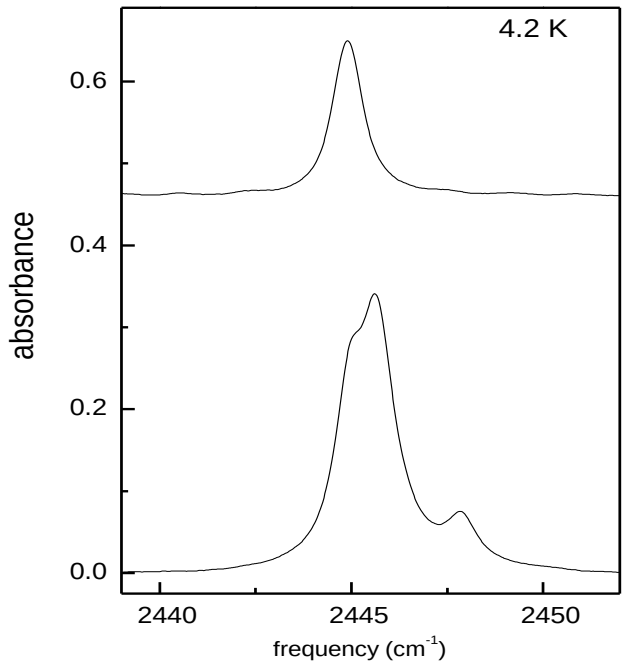

Fig. 4.6: IR absorption spectra (T=4.2 K, resolution 0.1 cm^{-1}) measured with **E⊥c** for TiO_2 samples prepared at Lehigh. The samples were deuterated by annealing in a D_2 ambient (4 h at 500 °C). The lower spectrum was measured without further annealing. The upper spectrum was measured following a subsequent anneal in air (30 min at 500 °C).

The single, sharp line (2445.0 cm^{-1}) seen in the spectra of samples that were D_2 treated and subsequently annealed in air can be attributed to a positively charged OD center (OD^-) that is present in a more fully oxygenated sample.(Charge states are referenced to a Ti^{4+}, O^{2-} ionic model). The two additional IR lines observed in the spectra of samples that were treated only in D_2 can be attributed to the neutral OD center (OD^{2-} present in a reduced TiO_2 sample. These additional lines were detected at 2445.7 and 2447.8 cm^{-1}. Since Bates and Perkins treated their samples in flowing oxygen to restore transparency after annealing in D_2 gas, their samples were intended to be fully oxygenated and this caused the observation of the

single line spectrum. It should be noted that some of the samples in their collection were not fully oxygenated and their measurement revealed the multiline structure as discussed above and shown in Fig. 4.5. Another reason why Bates and Perkins did not observe the partially resolved lines in some of their samples may be their usual measurement temperature. They performed most of their experiments at 77 K where the overlapping multiline shape could have been easily missed due to the broadened line shapes. Herklotz *et al.*, on the other hand, performed their measurements at low temperatures and with samples not intentionally oxygenated. Our experiments solve the puzzling discrepancy between the two previous studies by Bates and Perkins [4.8] and Herklotz et al. [4.11].

The IR data from a detailed air-annealing study of a D_2 treated sample is presented in Fig. 4.7. IR spectra for measurement temperatures of 4 K, 17 K and 50 K are shown in the panels of the figure. Measurements at 50 K make it difficult to resolve the multiline structure because the lines are broader. In addition to the effects of the measurement temperature, we were also interested in the effects of annealing temperature. A range of 100°C to 650°C was used for annealing temperatures, and a selection of the spectra measured between 250°C to 650°C are shown in comparison with of an as-treated sample. Since the measurements for the 100°C-250°C annealing temperature range did not produce any significant changes compared to the as-treated sample, they are not included in the plot. Note that a magnification of up to x32 was used for some spectra and is labeled in the plot. A quench in water to room temperature followed the annealing treatment for all of the measurements. Our annealing results show that with increasing annealing temperature, the multiline structure evolves to a single line that corresponds to the charged OD^- state. The neutral OD center starts to be

eliminated above 250°C and the charged OD^- center starts to dominate the IR spectra at higher annealing temperatures. Only OD^- (or full oxygenation) is present at around 650°C. This is a higher annealing temperature than observed in measurements shown in Fig. 4.6, possibly because quenching was used in the experiments shown in Fig. 4.7. The results shown in Fig. 4.6 are for a sample that was held in air at room temperature for cooling after annealing.

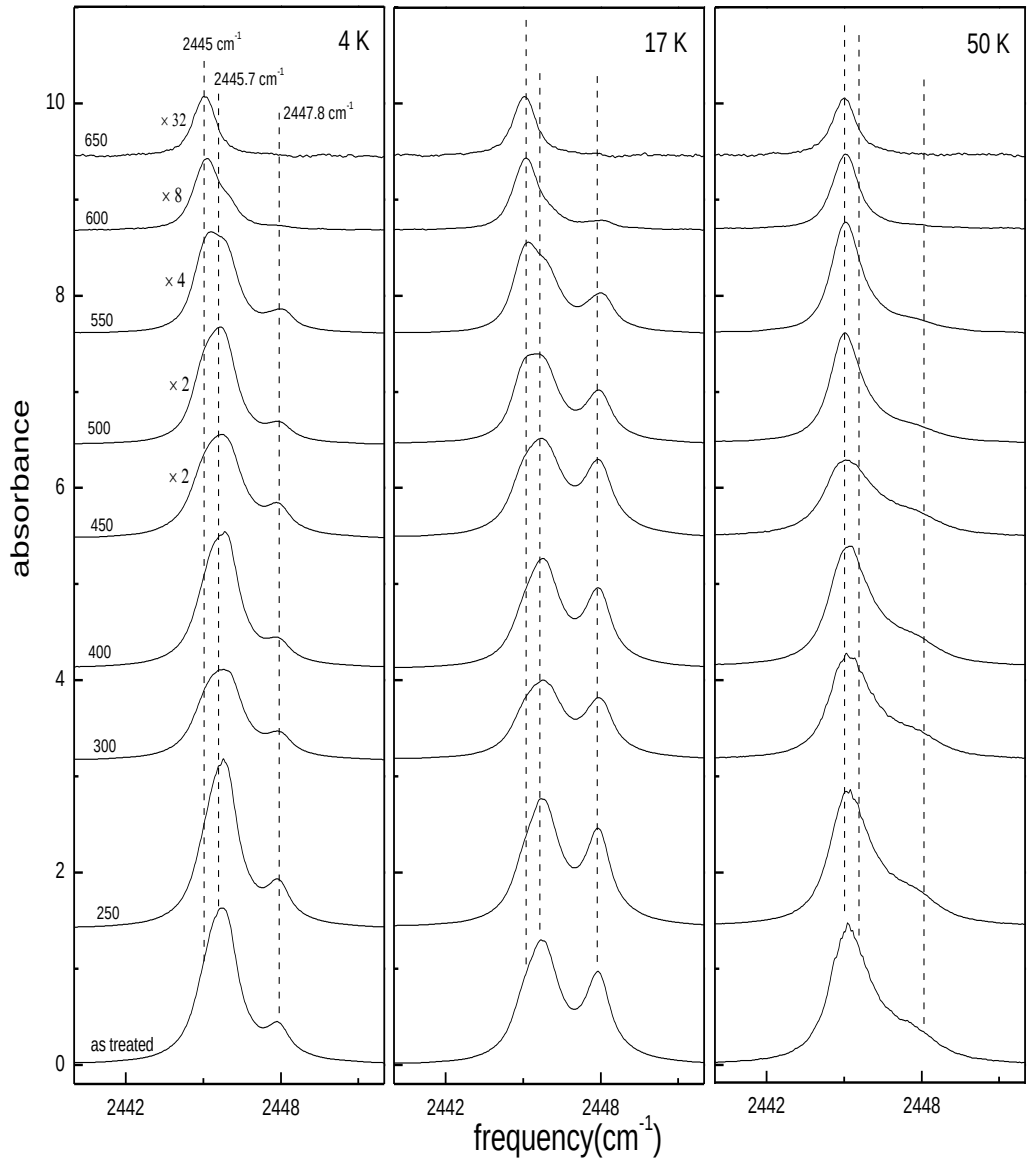

Fig. 4.7: IR absorption spectra (T=4 K,17 K ,and 50 K, resolution 0.1 cm^{-1} with **E⊥c**) for TiO_2 annealed in a D_2 ambient at 500°C for 4 hours with subsequent annealing treatments in air for 30 min at the temperatures shown. All anneals were terminated by a quench to room temperature in water.

Moreover, in order to understand where these charged and neutral states are located in the sample, a TiO_2 sample reduced by a treatment in a D_2 ambient at 500°C for 4 hours was mechanically thinned in several steps from each side, using silicon carbide for lapping and aluminum oxide powder and diamond paste for polishing. The thinning process was started with an initial thickness of 1.53 mm and ended at 0.62 mm. After each thinning step, an IR spectrum (at 4 °K and 17 °K) was measured (Fig. 4.8) in order to determine whether the charged and neutral states are located near the sample surface or throughout the sample bulk. Then, in order to reveal the changes in both neutral and charge states in more detail upon thinning, absorption lines of the charged and neutral states were determined by fitting the spectra with sums of Voigt line shapes (by using Peak Fit v4 software) as shown in Fig. 4.9 for the sample before and after all the thinning steps at 4 °K**.** In the reduced sample, the oxygen deficient neutral state gets relatively weaker deeper inside the sample while the charged state gets relatively stronger. The reason is that oxygen is reduced near the surface when the TiO_2 sample is annealed in D_2 ambient. Consequently, the oxygen-rich charge state (OD^-) gets stronger with respect to the neutral state when the sample surface is removed and the center of the sample is exposed. This also explains why when a sample is annealed in air, only the oxygen-rich charged (OD^-) state remains due to full oxygenation.

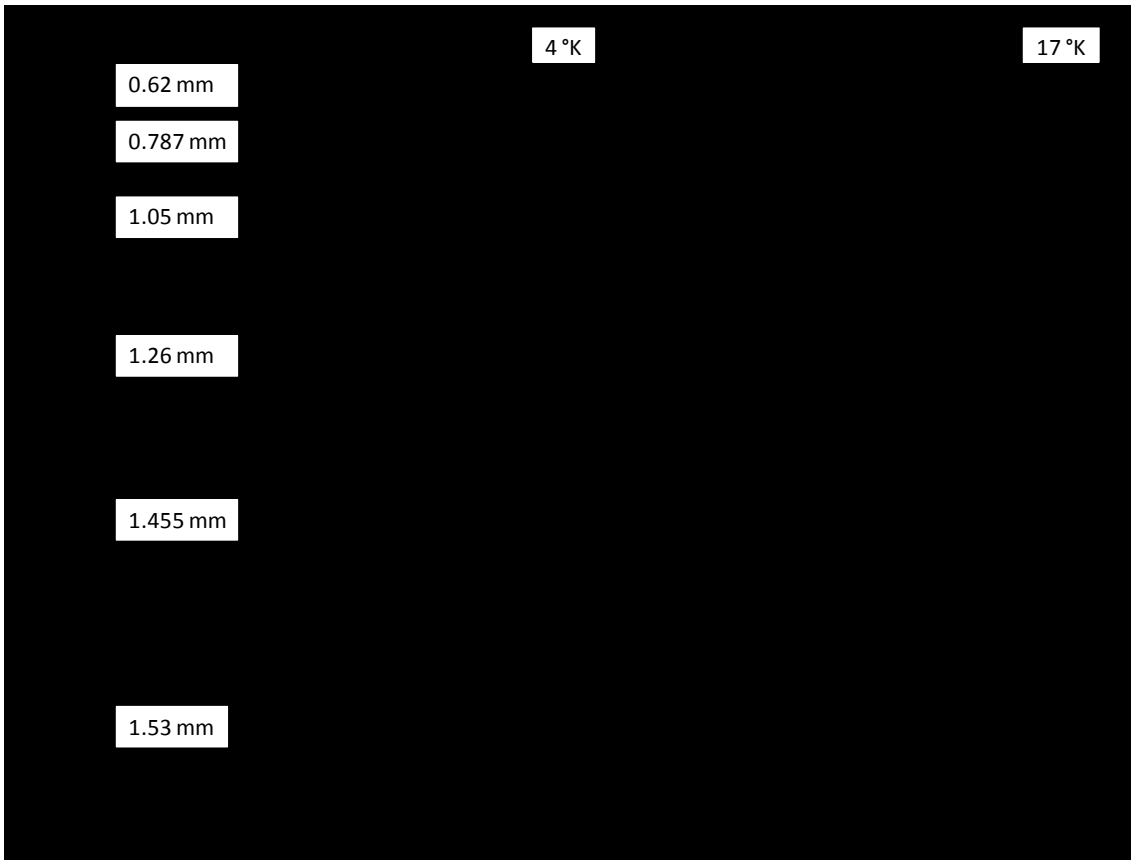

Fig. 4.8: IR absorption spectra (T=4 K and 17 K, resolution 0.1 cm^{-1}) for TiO_2 annealed in a D_2 ambient at 500°C for 4 hours. The sample was subsequently thinned in several steps from both sides, and measured at the thickness shown with polarized light **E⊥c**. An empty sample holder was used as the reference.

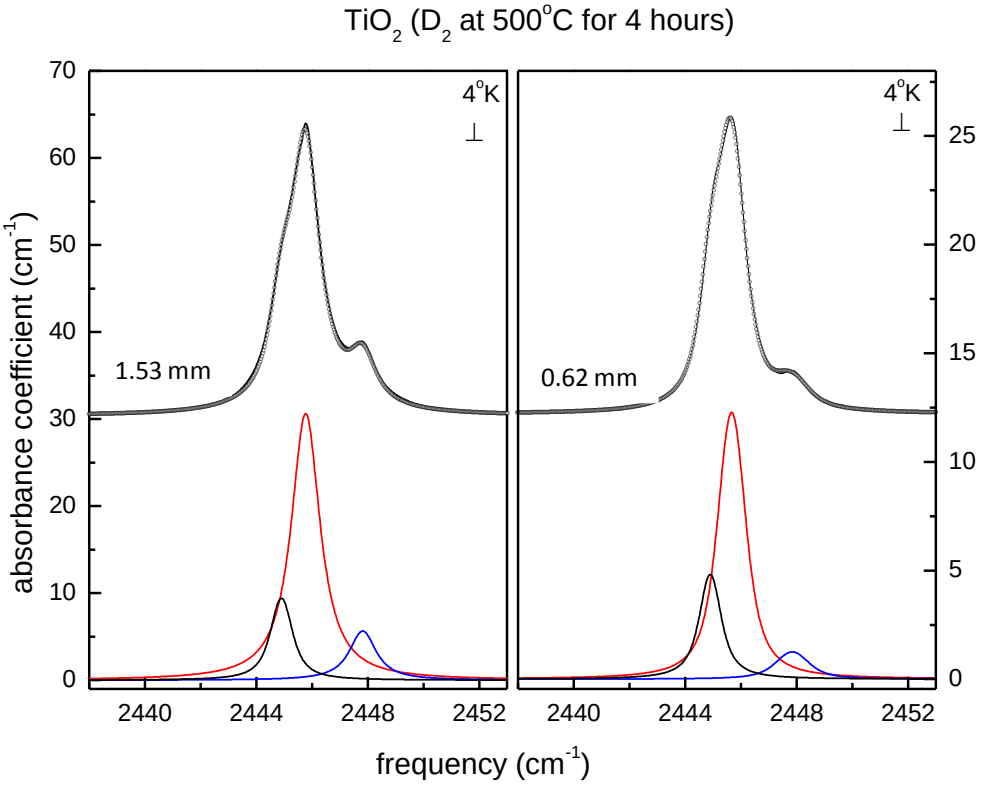

Fig. 4.9: IR absorption spectra (T=4 K, resolution 0.1 cm^{-1} with **E⊥c**) were measured for a TiO_2 sample annealed in a D_2 ambient (4 h at 500 °C) with the thickness 1.53 mm (on the left) and 0.62mm (on the right). The lower traces show fits to the spectra.

In addition to providing an explanation of the two different observations in the literature, our findings provide a strategy to distinguish and investigate the behavior of each state of the multiline structure separately. As a first step in our analysis, the OD^- charge state that is left alone in the spectrum after a full oxygenation of TiO_2 samples was studied by itself. For this purpose, a D_2 treated (4 hrs, 500°C) sample was subsequently annealed in air (30 mins, 500°C) and its IR spectra were measured at various temperatures from 3.5 K to 60 K. The temperature dependence of this single line attributed to OD^- is shown in Fig. 4.10 for the range 3.5 K to 35 K. Lorentzian line shapes corresponding to the best-fit curves determined by PeakFit v4 software are also presented in the figure. There is only a slight change in the line shape with increasing temperature, that is, the OD^- center shows little sensitivity to temperature changes.

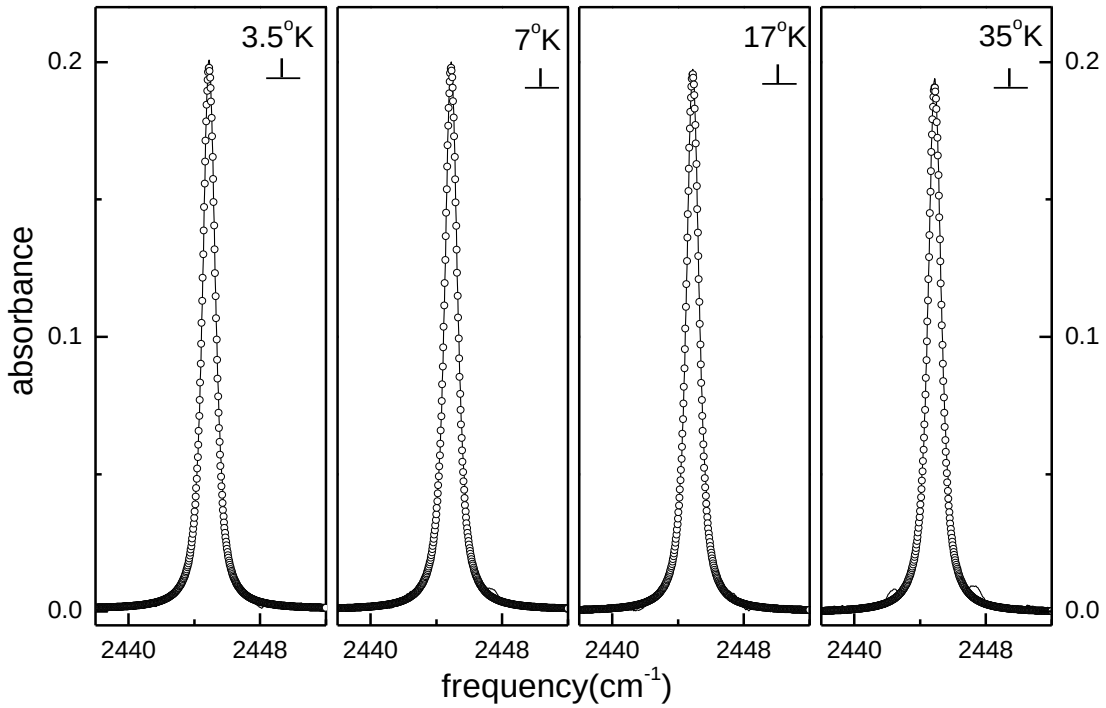

Fig. 4.10: IR spectra for the OD^- center measured at various temperatures (resolution = 0.1 cm^{-1}). Measurements were performed on samples treated in D_2 and subsequently annealed in air until only the OD^- charge state remained.

We have also measured the temperature dependence between 3.5 K and 60 K for the three partially resolved OD lines by performing experiments on D_2-treated (4 hrs, 500°C) samples. The resulting spectra for the range 4 K-50 K are presented as the upper curves in Fig. 4.11. In this case, strong temperature effects which are related to the temperature dependent behavior of the OD neutral state (2445.7 and 2447.8 cm^{-1} lines) are observed.

Distinguishing the overlapping curves in order to separately study the behavior of each state is not straightforward. As a first step, we fit the experimental results for the three-line spectrum (upper traces in Fig. 4.11) from across the range of measurement temperatures to a

sum of Voigt line shapes. We obtained good fits that revealed a constant contribution from the charged OD^- defect. Based on this insight, we subtracted the spectrum for the air-annealed sample (scaled by a single constant factor, independent of temperature) from the spectrum measured for the sample reduced by annealing in D_2, temperature by temperature. This procedure yielded the spectrum for the neutral charge state alone at each temperature (center traces Fig. 4.11). The spectra for the neutral OD center could then be fit by the sum of two Voigt line shapes (lower traces Fig. 4.11) with frequencies (4 K) of ω_L=2445.7 cm^{-1} and ω_H=2447.9 cm^{-1}. These fits were made with Peak Fit software.

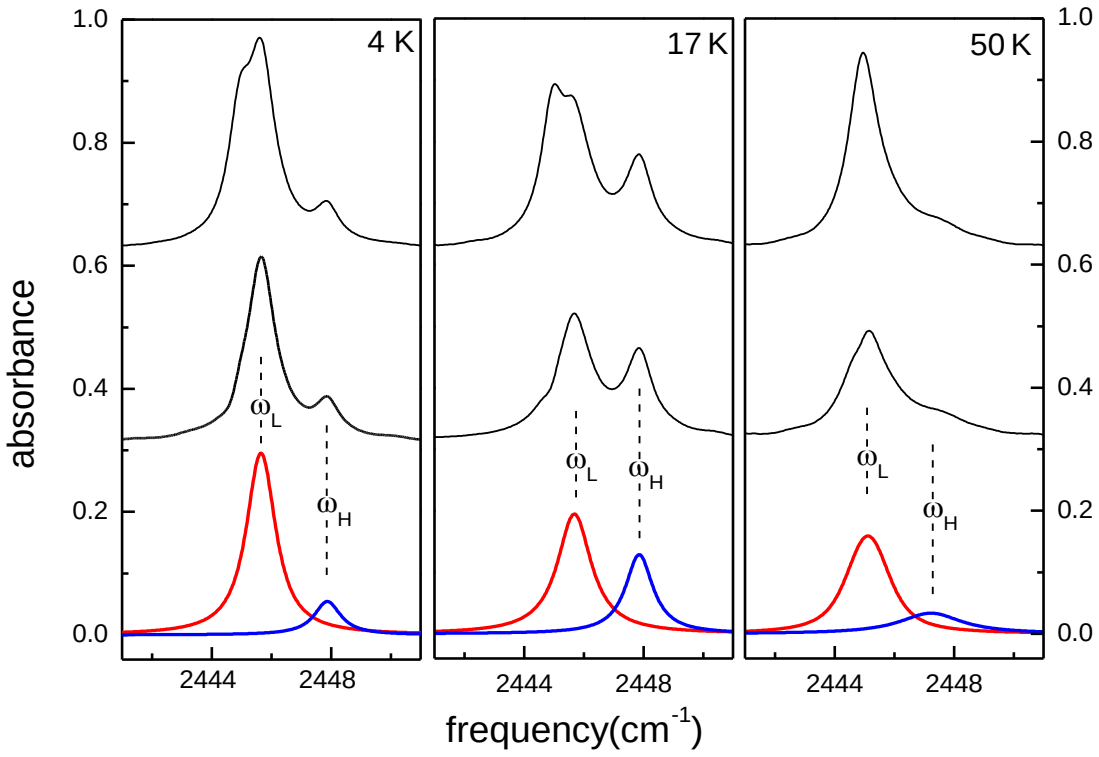

Fig. 4.11: IR absorption spectra (T=4 K, 17 K and 50 K, resolution 0.1 cm^{-1} with **E**⊥**c**) measured as a function of temperature for a TiO_2 sample annealed in a D_2 ambient (4 h at 500 °C). The upper traces show the IR spectra, as measured. The center traces show the spectra after the contribution from the line at 2445.0 due to the charged OD^- center has been subtracted. The lower traces show the fits to the spectra of the neutral charge state by a sum of two Voigt line shapes.

In order to investigate the neutral state's temperature dependence more carefully, the integrated areas of the two absorbance lines at ω_L and ω_H [$A(\omega_L)$ and $A(\omega_H)$] which are attributed to the neutral OD center are plotted vs. temperature, as shown in Fig. 4.12. The neutral OD center has an interesting temperature dependence. Between 4 K and 20 K, $A(\omega_L)$

decreases in intensity while $A(\omega_H)$ increases in intensity, showing what appears to be a simple activated behavior. However, above 20 K, $A(\omega_L)$ regains intensity at the expense of the intensity of $A(\omega_H)$. This behavior is surprising and requires further consideration. As a side note, the total area of the IR lines of the neutral OD center remains approximately constant between 4 K and 60 K.

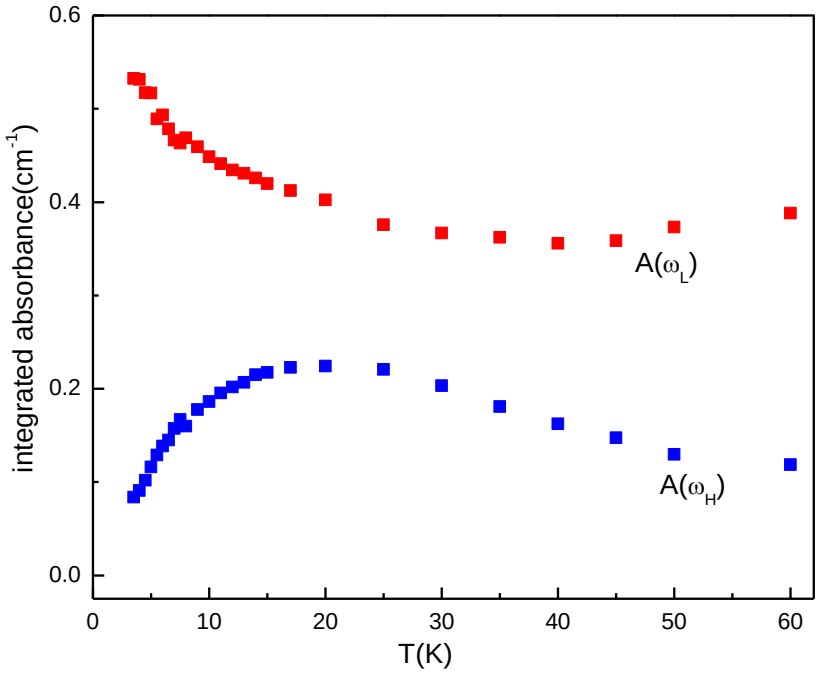

Fig. 4.12: The integrated areas of the absorbance lines, $A(\omega_H)$ and $A(\omega_L)$, measured as a function of temperature for the two components assigned to the neutral OD center in TiO_2.

The next step in our analysis is to investigate the intensity ratio of these two absorbance lines as a function of temperature. For simple activated behavior, a linear slope is expected from a semi-log plot of this ratio versus inverse temperature (Fig. 4.13), following the relation

$$A(\omega_H)\Big/A(\omega_L) \propto e^{(-\frac{\Delta E}{kT})} \tag{4.1}$$

Between 4 K and 20 K, there is a linear slope. However, at higher temperatures (above 20 K) a sharp transition from an ascending to a descending curve is observed. The previously mentioned intensity switch between the absorption lines at ω_L and ω_H is the reason for this sharp transition at around 20 K. We interpret this change in slope as being due to an additional configuration of the neutral state that is indistinguishable from the ground neutral state configuration at ω_L.

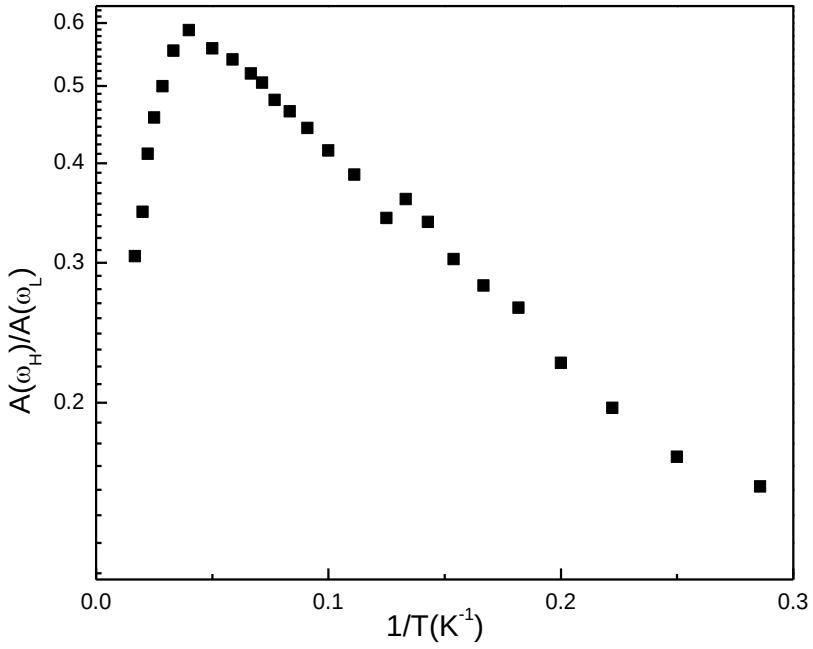

Fig. 4.13: Semi-log plot of the ratio of the areas of the IR lines at ω_H and ω_L associated with the neutral OD center vs. inverse temperature.

The temperature dependence of the IR lines corresponding to the neutral state cannot be fit by a simple model with two components with different energies. Previously, Herklotz *et* al. [4.11] proposed a model, supported by additional experimental observations. In this model, neutral OD was proposed to become ionized to give an IR line near ω_L at elevated temperatures. A correlation of the ionization of neutral OD with the appearance of absorption attributed by Herklotz *et al*. to free carriers supported this suggested model. The overall conclusion of Herklotz *et al*. was that D (or H) gives rise to a shallow donor in TiO_2 with an ionization energy of 10 meV and Drude-like, free-carrier absorption [4.12].

We propose a different model to explain the temperature dependence of the IR lines at ω_L and ω_H (shown in Fig. 4.12 and Fig. 4.13) that involves the properties of the neutral OD center alone. We favor this model due to two observations; 1) we have seen no appreciable absorption in our spectra that might be associated with free carriers as seen in Fig. 4.14; 2) we have seen no temperature dependence for the intensity of the OD^- state, i.e. no intensity exchange between the neutral and OD^- states. In our model, at least three configurations with different energies for the neutral OD center will be considered, as depicted in the inset to Fig. 4.15. The neutral OD configuration with lowest energy, E_1, gives a line at ω_L, while the configuration with energy E_2 gives a line at ω_H. And the configuration with energy E_3 gives a line again at ω_L that is indistinguishable from the contribution of the configuration with energy E_1. In summary, two configurations with different energies, namely E_1 and E_3, happen to have the same frequency, $\omega_{L,}$ while the configuration with energy E_2 has a different frequency, ω_H.

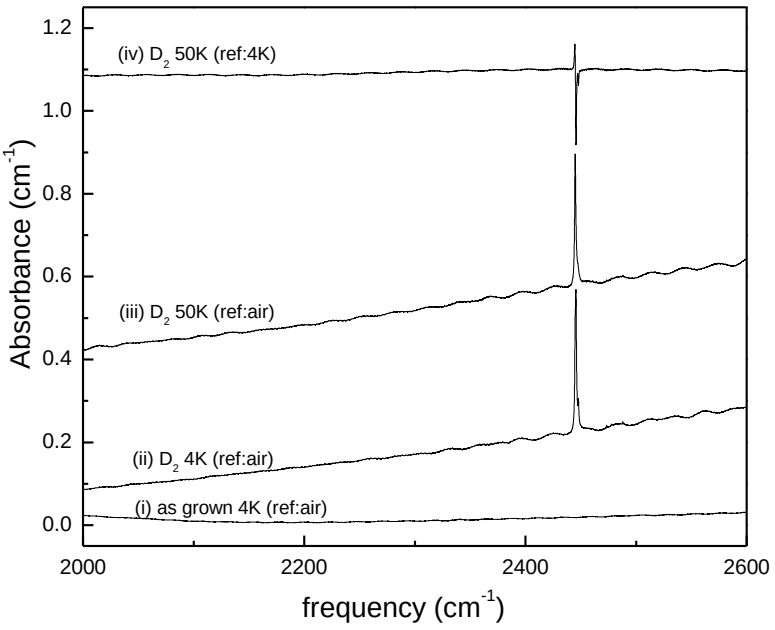

Fig. 4.14: The free carrier absorption spectra of an as-grown and D_2 treated (4h at 500 ^oC) TiO_2 samples measured at 4 ^oK and 50 ^oK with a resolution = 0.1 cm^{-1}. For spectrum (i), (ii),and (iii), an empty sample holder was used as the reference but for the spectrum (iv), the spectrum measured at 4 ^oK was used as the reference to repeat Herklotz's [4.11] free carrier absorption experiment with our samples.

In this model, the areas of the lines at ω_L and ω_H, are given by the following expressions:

$$A(\omega_L) = \left[p_1 g_1 + p_3 g_3 exp\left(^{-E_3}/_{kT}\right)\right]/_{Z} \quad , \tag{4.2}$$

and,

$$A(\omega_H) = {[p_2 g_2 exp\left({-E_2}/{kT}\right)]}/{Z}, \tag{4.3}$$

respectively, where Z is the partition function for the 3-level system (shown in the inset to Fig. 4.15) given by,

$$Z = g_1 + g_2 exp\left({-E_2}/{kT}\right) + g_3 exp\left({-E_3}/{kT}\right). \tag{4.4}$$

The g_i are the degeneracies of the different levels and the p_i account for the fact that the IR transitions for the different configurations can have different oscillator strengths. Finally, using the relations Eqs. 4.2 and 4.3, the ratio of the areas of the IR lines at ω_L and ω_H shown in Fig. 4.13, can be expressed as

$$A(\omega_H)/A(\omega_L) = \frac{p_2 g_2 exp\left({-E_2}/{kT}\right)}{p_1 g_1 + p_3 g_3 exp\left({-E_3}/{kT}\right)}. \tag{4.5}$$

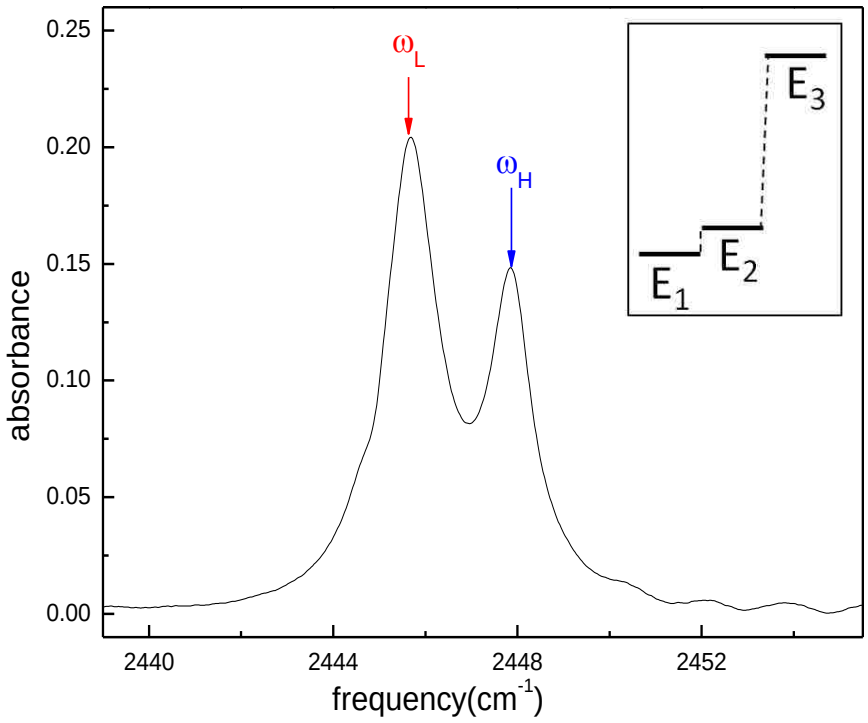

Fig. 4.15: IR spectrum of the neutral OD center alone, with two IR lines with frequencies ω_L and ω_H. (Inset) The energies corresponding to the three-level system.

In the following procedure, the values of p_i, g_i, E_2 and E_3 that give a best fit model to the experimental data will be determined. This optimization procedure has two steps. In the first step, the model given by Eq. 4.5 was fit to the data seen in Fig. 4.13 using the Microsoft Excel Optimization Solver. Independent of initial values for parameters, E_2 and E_3 converged to 0.5 ± 0.05 and 11 ± 4 meV respectively, and the fit of the model with the data is presented in Fig. 4.16. In this initial step, these energy values are determined and fixed for the next step. Before proceeding with the second optimization step, a detailed analysis of the model and the experimental data in the limits of low and high temperature will be given next. For convenience, consider the reciprocal of Eq. 4.5

$$A(\omega_L)\Big/A(\omega_H) = \frac{p_1 g_1 + p_3 g_3 exp\left(-E_3/kT\right)}{p_2 g_2 exp\left(-E_2/kT\right)} \tag{4.6}$$

For low temperature (<10 K), the relation of 4.6 versus 1/T simplifies to

$$A(\omega_L)\Big/A(\omega_H) = \frac{p_1 g_1}{p_2 g_2}\ exp\left(\frac{E_2}{kT}\right) \tag{4.7}$$

Therefore, in the limit of low temperature, the slope of the semi-log plot of $A(\omega_H)/A(\omega_L)$ (Eq. 4.5) versus 1/T is equal to E_2/k. Moreover, the y-intercept of the curve given by log (p_2g_2/p_1g_1) is a constraint that will be used in the fitting procedure. From a graphical analysis, a range between 0.61 and 0.95 was determined for the ratio (p_2g_2/p_1g_1).

$$0.61 \leq \frac{p_2 g_2}{p_1 g_1} \leq 0.95 \tag{4.8}$$

A similar procedure can be applied for the high temperature range (> 35 K). Starting with Eq. 4.6 and considering the high temperature limit, the relation simplifies to,

$$A(\omega_L)\Big/A(\omega_H) = \frac{p_1 g_1}{p_2 g_2} + \frac{p_3 g_3}{p_2 g_2} exp\left(-\frac{E_3 - E_2}{kT}\right). \tag{4.9}$$

In the limit of high temperature, the slope of the semi-log plot of Eq. 4.5 versus 1/T is equal to $(E_3\text{-}E_2)/k$. The y-intercept of the curve generates another relationship between the p_i and g_i for which the following ranges were determined from a graphical analysis and with the use of Eq. 4.8:

$$6 \leq \frac{p_3 g_3}{p_1 g_1} \leq 12 \tag{4.10}$$

In the second step, E_2 and E_3 values determined in the first step were used as fixed values in Eq. 4.2 and Eq. 4.3 in order to provide the best fit of the model to the experimental data shown in Fig. 4.12. The p_i and g_i values were adjusted using a least squares error minimization procedure, subject to the constraints Eq. 4.8 and Eq. 4.10. The Microsoft Excel Optimization Solver was used again for this purpose and the following values were found to yield the best fit to our data:

p_1	p_2	p_3	g_1	g_2	g_3
0.679	0.514	0.382	1	1	19.561

Table 4.1: Adjusted values of p_i and g_i for the best fit model to data.

The fit parameters p_i vary by only small factors near 1, consistent with the expectation that different OD configurations should have similar oscillator strengths. The degeneracies of levels E_1 and E_2 were found to be one while a high degeneracy was found for the level E_3. The sharpness of the transition between ascending-descending slopes seen for the semi-log plot in Fig. 4.13 requires a larger degeneracy for the level E_3. Using these values, a comparison of the model with the experiments is shown in Fig. 4.16 and Fig. 4.17. In Fig. 4.17, the model results shown by a solid line fits very well the integrated absorption data corresponding to the lines at ω_L and ω_H (shown by circles). Also shown in the figure with dashed lines are the model results for the contributions of levels E_1 and E_3 that sum to yield the area $A(\omega_L)$. The contribution from the E_3 level is significant above 20 K while the contribution from the E_1 level continuously

decreases with increasing temperature. A fit to the ratio of the areas of the IR lines at ω_L and ω_H is shown in Fig. 4.16. A very good fit that provides a good representation of the sharp transition in slopes near 20 K is obtained.

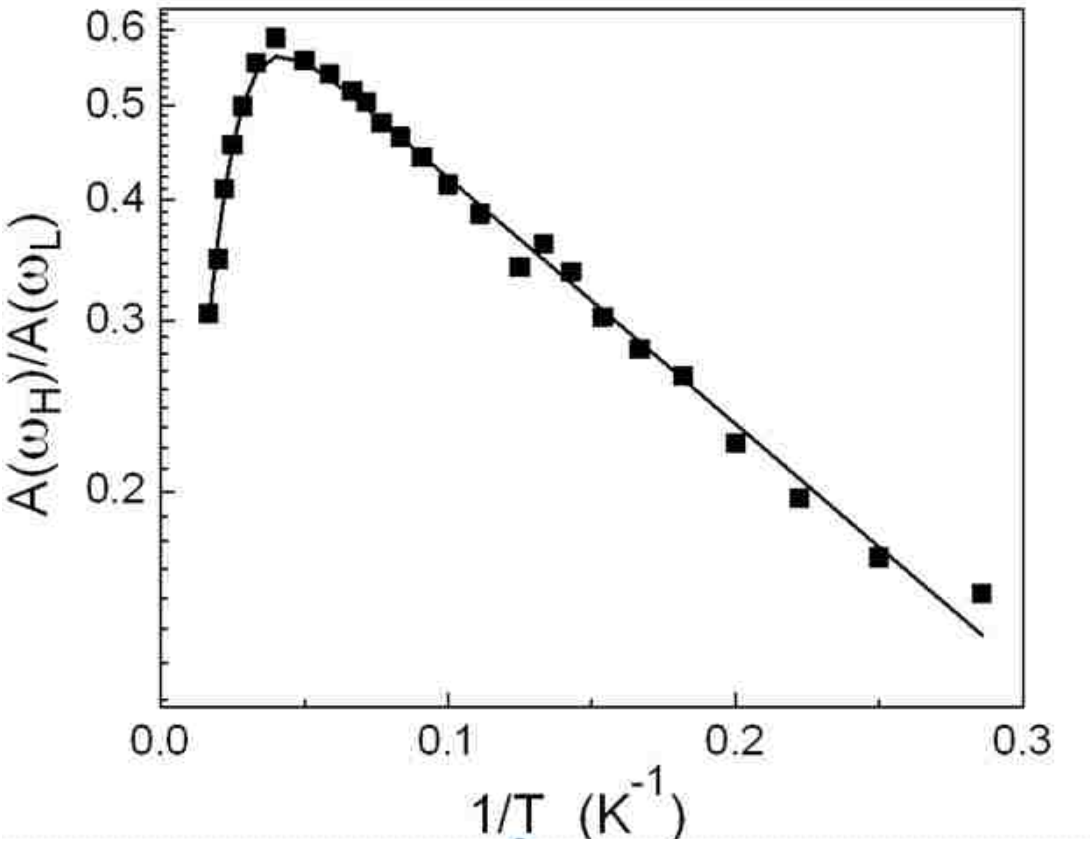

Fig. 4.16: Semi-log plot of the ratio of the areas of the IR lines at ω_H and ω_L associated with the neutral OD center vs. inverse temperature. The solid line shows a fit to the ratio of the areas of the IR lines at ω_H and ω_L associated with the neutral OD center vs. inverse temperature.

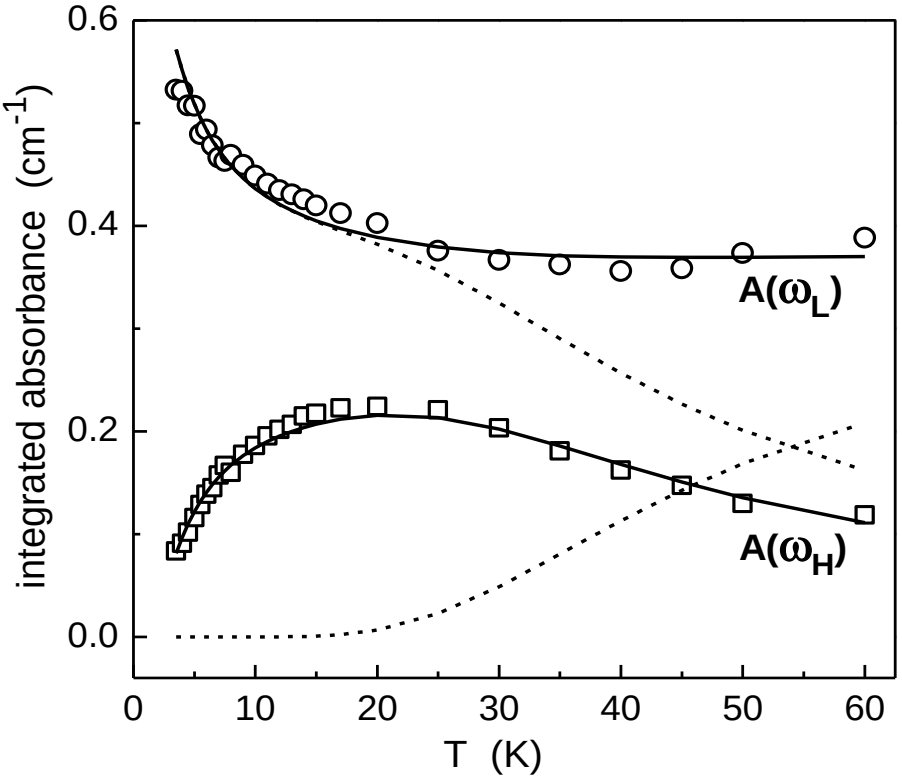

Fig. 4.17: The integrated areas of the absorbance curves, $A(\omega_H)$ and $A(\omega_L)$, measured as a function of temperature for the two components of the line shape assigned to the neutral OD center in TiO_2. The solid lines show fits to the experimental data for the line areas. The dashed lines show the areas of the contributions arising from the levels E_1 and E_3 that sum to yield the area $A(\omega_L)$.

The high degeneracy given by g_3 should also be mentioned here. Although a very good fit was obtained with g_3=19, other satisfactory fits are also possible with g_3>12 for the intensity ratio plot, as shown in Fig. 4.18, indicating a high degeneracy for the E_3 level. The sharpness of the transition between ascending-descending slopes increases with increasing value of g_3. We have selected g_3=19 for the analysis because it gives a very good fit to the intensity ratio and also gives the best fits to separate plots of $A(\omega_L)$ and $A(\omega_H)$ together. The fit of the model to

the $A(\omega_L)$ and $A(\omega_H)$ data for different g_3 values is shown in Fig. 4.19. Clearly, the match between model and data for $g_3<12$ and $g_3>20$ becomes less successful. The adjusted parameters found for the optimized fit using different g_3 values are listed in Table 4.2. It should be noted that in this analysis we have fixed g_3 to the values presented in the table and have done the optimization in a reversed order. We have first optimized $A(\omega_L)$ and $A(\omega_H)$ by constraining g_3 only and found E_2 and E_3 values. Then these were input in the second optimization step for the ratio $A(\omega_H)/A(\omega_L)$. If the optimization procedure is started with the ratio $A(\omega_H)/A(\omega_L)$, each g_3 value would yield the same E_2 and E_3 values which results in less satisfactory fits in the $A(\omega_L)$ and $A(\omega_H)$ plots.

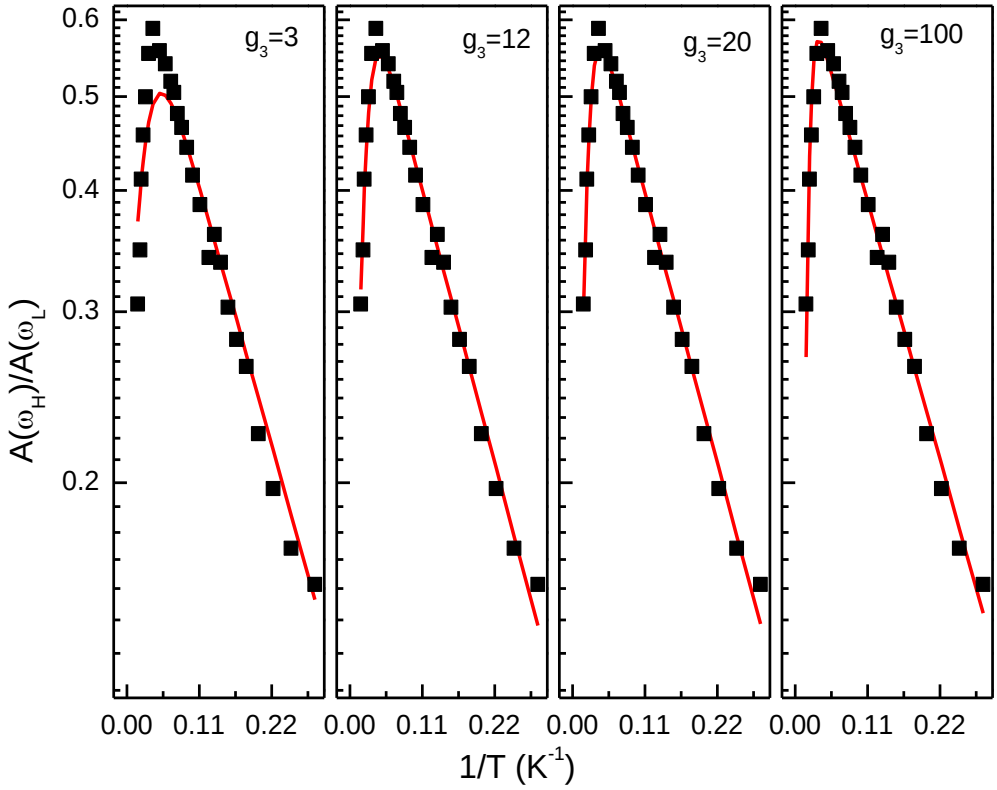

Fig. 4.18: Semi-log plot of the ratio of the areas of the IR lines at ω_H and ω_L vs. inverse temperature with different degeneracies (g_3= 3, 12, 20, and 100) for level E_3. The solid lines represent fits to the experimental data.

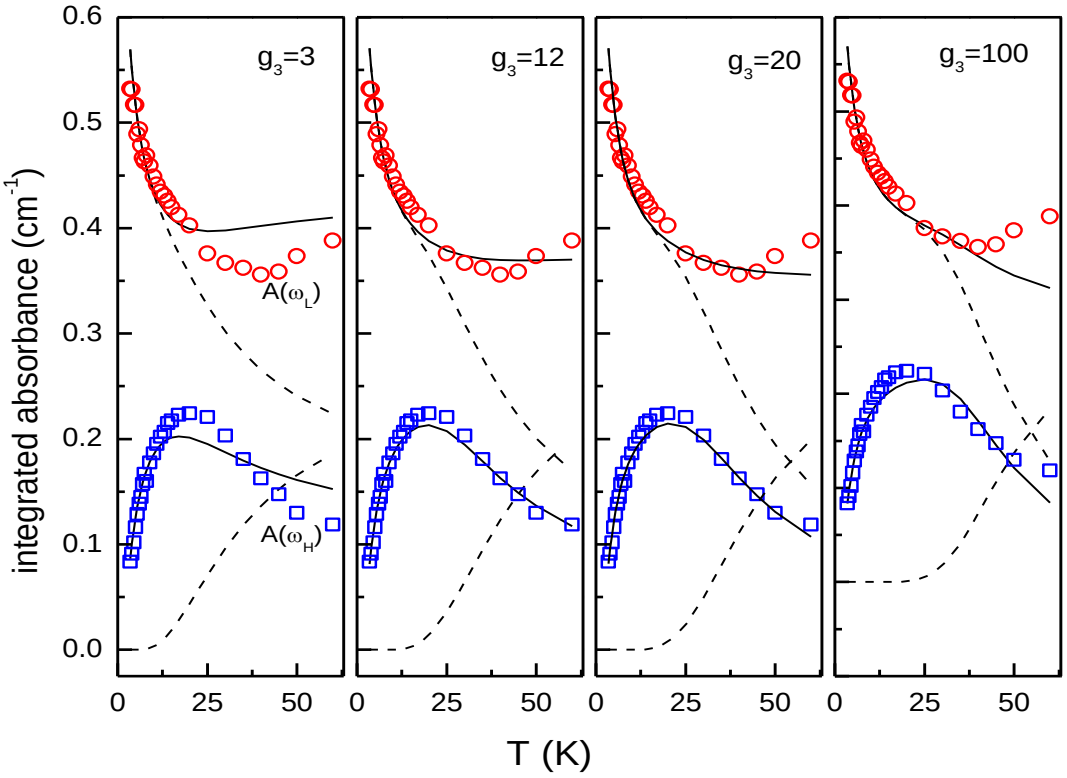

Fig. 4.19: The integrated areas of the absorbance curves, $A(\omega_H)$ and $A(\omega_L)$, measured as a function of temperature fitted with different degeneracies (g_3= 3, 12, 20, and 100) for level E_3. The solid lines show the fit to the experimental data. The dashed lines show the areas of the contributions arising from the levels E_1 and E_3 that sum to yield the area $A(\omega_L)$.

	g_3=3	g_3=12	g_3=20	g_3=100
E_2	0.482	0.507	0.502	0.480
E_3	4.958	9.005	10.895	17.448
p_1	0.685	0.677	0.678	0.685
P_2	0.512	0.518	0.512	0.493
P_3	0.496	0.384	0.356	0.287

Table 4.2: Adjusted values of the p_i and the level energies for degeneracies of level E_3 for the best-fit model to data with g_3 held fixed at the selected value.

4.3.2 O-H stretching vibrational mode

Up to now, the data analyzed and discussed are related to the IR lines of OD centers in TiO_2. In this section, the results for the OH lines from similar experimental and modeling approaches will be presented. Since the samples, the experimental set-up and the modeling method are the same as was introduced for the OD vibrational modes, the focus will be on the results for the OH modes.

Due to the increased noise and the reduced sharpness of the IR lines for the OH center, the determination of the frequencies for the IR lines that overlap is not as easy as in the OD case. An air annealed sample was first measured at temperatures between 3.5 K and 60 K, and as was observed for the OD lines, only the positive charge states, i.e. OD^- and OH^-, remain in the spectra. From these measurements, the frequency arising from OH^- was determined to be 3287.4 cm^{-1} at 4 K and changed only slightly at higher temperatures.

It is difficult to determine the frequencies of the overlapping components of the IR band for the O-H center. In order to determine the frequencies ω_L and ω_H for the OH range, a constant ratio of the frequencies of OH and OD has been assumed. The shift factors were found from the ratio measured for the frequencies of the positive charge state for OD and OH at each temperature. These factors were multiplied times the ω_L and ω_H frequencies for the OD center to obtain the corresponding frequencies for the OH center. The ratio for the temperature range 3.5 K-60 K was found to be 1.34459±0.00001 (the theoretical value for an OH diatomic is 1.374) and the ω_L and ω_H frequencies for OH were determined to be 3288.4 cm^{-1} and 3291.4 cm^{-1}, respectively, at 4 K.

The method used to fit the IR line shapes for the OD center was used to analyze the line shape for OH. The three overlapping OH lines, the contribution from the neutral OH center alone, and the fits for the components at ω_L and ω_H are plotted in Fig. 4.20. The same methodology used to find a best fit to the experimental areas of the IR lines at ω_L and ω_H for the OD neutral center was used to generate the best fit curves shown in Fig. 4.21 and Fig. 4.22 for the neutral OH center. The optimized parameters for this fit are listed in Table 4.3. E_2 was determined to be 0.5 ± 0.38 meV and E3 was found to be 11 ± 9.5 meV from the high and low temperature slopes of experimental data in Fig. 4.22. The error in energy level is found to be the value that doubles the total error in the least square analysis.

p_1	p_2	p_3	q_1	q_2	q_3
0.703	1.107	0.810	1	1	40

Table 4.3: Adjusted values of p_i and g_i for the best fit model to data for the O-H center.

The data for the OH range are more scattered due to the increased line widths and the difficulty of uniquely separating the lines. The fit is not as good as the one for the OD range. However, very similar trends are observed. At around 20 K, a sharp transition in the ratio of areas of IR lines at ω_L and ω_H is caused by an increase in the intensity of ω_L line which is the sum of contributions from the levels E_1 and E_3. Again, in the same temperature range, the contribution from the E_3 level starts to grow while the contribution from the E_1 level decreases.

The uncertainties in the values of the energies have prevented us from obtaining useful information about isotope shifts for the energy separations $E_2 - E_1$ and $E_3 - E_1$.

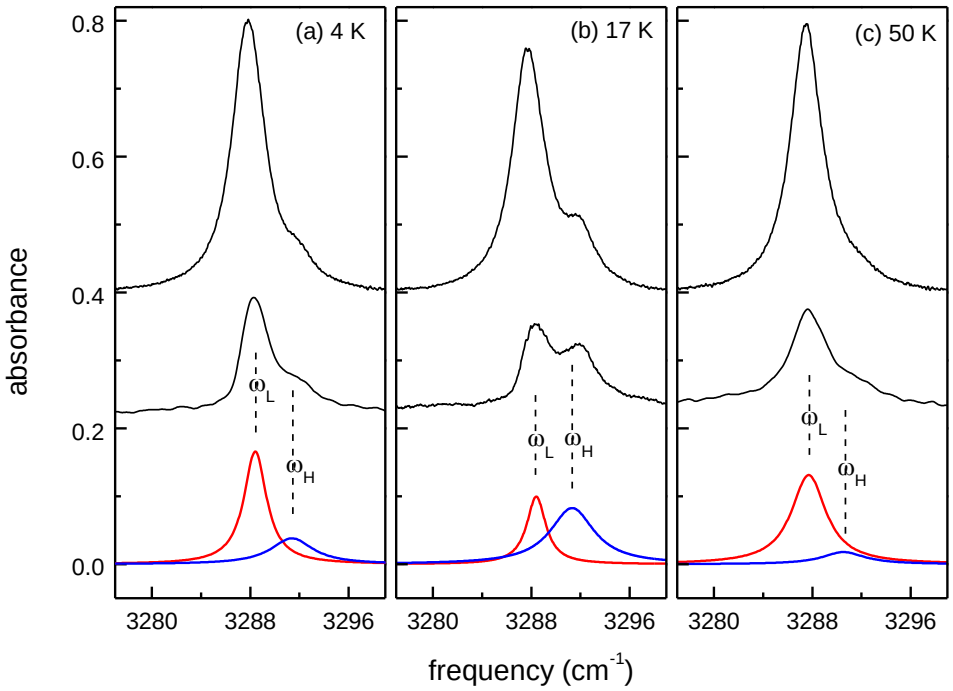

Fig. 4.20: IR absorption spectra (T=4 K, 17 K and 50 K, resolution 0.1 cm^{-1} with **E**⊥**c**), showing the O-H stretching region, measured as a function of temperature for a TiO_2 sample annealed in a D_2 ambient (4 h at 500 °C). The upper traces show the IR spectra, as measured. The center traces show the spectra after the contribution from the line at 3287.4 due to the charged OH center had been subtracted. The lower traces show the fits to the spectra by a sum of two Lorenzian line shapes.

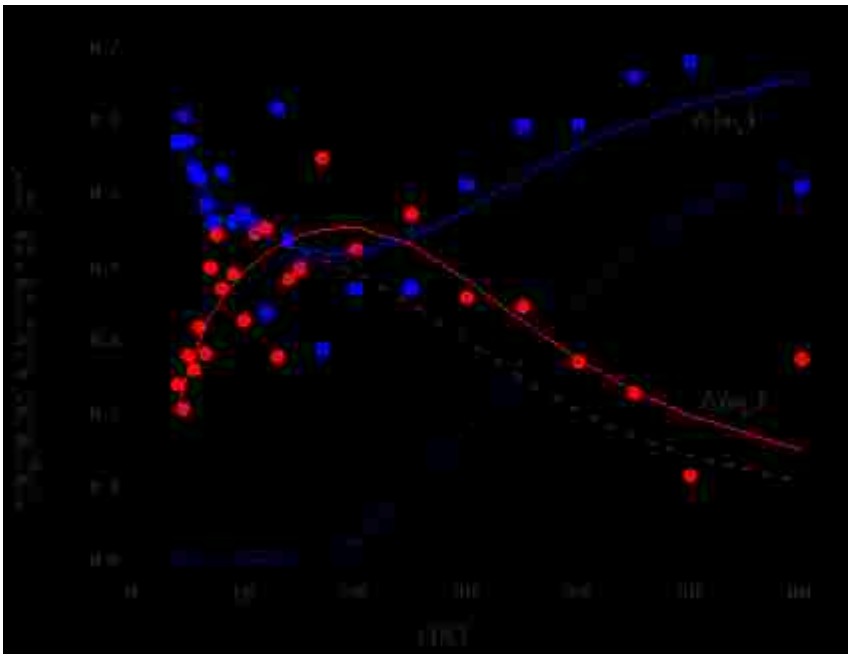

Fig. 4.21: The integrated areas of the absorbance curves, $A(\omega_H)$ and $A(\omega_L)$, measured as a function of temperature for the two components of the line shape assigned to the neutral OH center in TiO_2. The solid lines show fits to the experimental data for the line areas. The dashed lines show the areas of the contributions arising from the levels E_1 and E_3 that sum to yield the area $A(\omega_L)$.

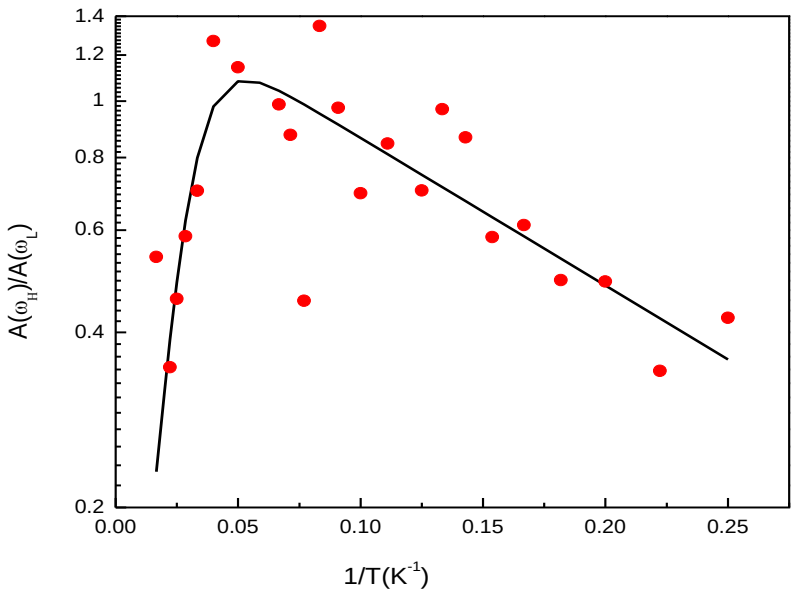

Fig. 4.22: Semi-log plot of the ratio of the areas of the IR lines at ω_H and ω_L associated with the neutral OH center vs. inverse temperature. The solid line shows a fit to the ratio of the areas of the IR lines at ω_H and ω_L associated with the neutral OH center vs. inverse temperature.

4.3.3 Small Polaron Model

In this section, we explain the physical origin of the three configurations with different energies that lead to the temperature dependent behavior observed in our IR measurements. For this purpose, we depend on theory performed by W.F. Fowler. CRYSTAL06 software [4.15] has been used for theoretical calculations in order to study various properties of TiO_2 and H_i in this rutile lattice. A hybrid DFT approach with a gradient-corrected approximation to the exchange-correlation functional [Becke's B3LYP potential [4.16] with (in most cases) 20 % exact exchange and Lee-Yang-Parr correlation [4.17]] was used to generate the theoretical results. The calculations were carried out in a periodic supercell with 48 or 72 host atoms. The

following computed lattice constants were used in these supercells: a = 4.572 Å, c = 2.984 Å, and u = 0.305 and Gaussian basis functions [4.18-4.20] were of the type 8411 for O, 8651(d3) for Ti, and 311p(1) for H.

The unusual electronic properties of TiO_2 and their relationship with the crystal structure have been examined first. Electron self trapping on Ti is such an unusual and important characteristic that stems from the Ti d-like character of the lowest conduction band [4.21-4.24], unlike the s/p-like character seen in many other metal oxides including SnO_2. This kind of behavior can be explained by the small polaron model [4.25]. According to this model, an extra electron can be self-trapped near a single lattice atom by displacing the nearby lattice atoms and creating a localized potential well. This is illustrated in Fig. 4.23 (a) [4.25]. In the figure, the excess electron represented by a dot is trapped near a lattice atom and displaces the neighboring lattice atoms as shown by circles. This changes the local potential well that was already provided in the lattice by the undisplaced atoms (top of Fig. 4.23 (b)) to a self-trapping potential well as shown just below, reducing the energy of the excess electron.

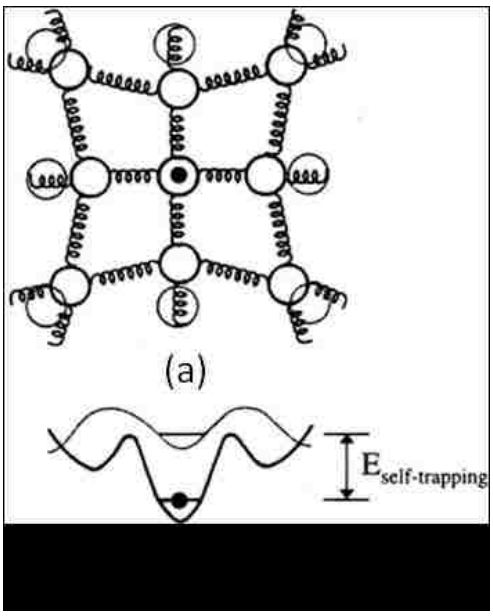

Fig. 4.23: a) Illustration of small polaron formation with a trapped excess electron (black dot) and associated displacements at neighboring lattice atoms (circles), b) Illustration of the change in the potential from that of a regular lattice configuration (top) to a modified, self-trapping well after atomic displacements (bottom) [4.25].

Similar to the explanation made for the small polaron model, electron self-trapping on Ti also occurs with associated displacements of neighboring ions. Thus, the electron behaves not as a Bloch function, but as a small polaron inside TiO_2 [4.25-4.28].In other words, it is energetically more favorable for the excess electron to localize in the d-orbital of one Ti atom than to spread out in the lattice with wave characteristics [4.10]. A band gap of 3.76 eV was determined from the band structure computation with CRYSTAL06. The bands correspond well with those of earlier calculations and exhibit the complex nature of the lowest conduction bands, even though the predicted band gap is larger than experiment [4.29].

In Fowler's calculations, electron self-trapping near a Ti atom in a rutile TiO_2 supercell was predicted. When an extra electron was placed within a TiO_2 supercell, it tended to localize around a single Ti atom. It should be noted that this occurs with 20% exchange potential although nearly complete localization requires a 30% exchange potential.

Another important observation resulting from Fowler's CRYSTAL06 calculations occurred when an interstitial H was included in the rutile supercell; slightly different initial choices of atomic positions resulted in slightly different minimum energy atomic configurations. And each of these exhibits spin localization on a different Ti! Thus the small-polaron nature of the electron persists, even when it comes from H_i. This result is consistent with several published accounts [4.30-4.32] in which either correlation or hybridization was included in the density functional formalism. Please refer to Fig. 4.24 for an example of the localization of a H_i electron in a 192 atom rutile TiO_2 supercell, calculated by the Vienna ab initio simulation package, VASP 5.2.8 [4.32]. We use these and other results to address the origin of the energy levels that emerge from the analysis of our experimental results.

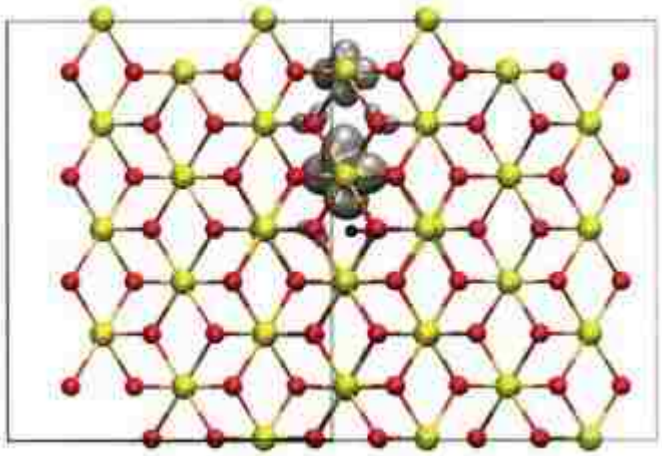

Fig. 4.24: Predicted localization of the electron of an H_i donor in a 192 atom TiO_2 supercell calculated by VASP 5.2.8. [4.32]

Before associating the small splittings seen in our vibrational spectra for TiO_2 samples to the small polaron phenomenon, we should consider some other possible and common sources of such splittings. The first alternative source to be investigated can be the effect of different heavy atom isotopes. Although the presence of ^{17}O and ^{18}O in TiO_2 can shift the spectra, it is very unlikely to be the reason for the splittings observed in our spectra due to very small abundances of these isotopes. Also, even if there were such isotopes in the crystal, we would expect a larger splitting due to these heavy oxygens than has been observed. Second, we can consider splitting due to effects of H or D tunneling between oxygen atoms. This can easily be ruled out since the splitting observed in our spectra would be too small to be associated with this effect. The potential energy function of H_i as a function of distance from O was previously calculated by Fowler et al. [4.33], and it was shown that the large relaxation characteristic of the O-H defect removes any potential tunneling degeneracy with respect to the O that lies across the channel. Basically, the O-O distance is too large for H or D tunneling

to occur in TiO_2. Finally, hindered rotation was considered as an alternative source for the splittings. Rotational effects can be ruled out with confidence due to the low symmetry of rutile. As a matter of fact, there is no axis of rotation for the OH complex lying in the xy plane of the TiO_2 rutile structure.

In conclusion, we propose that the near degeneracy of a small polaron electron that arises from H_i and can localize on different Ti, can be used to explain the energy splitting observed in the vibrational spectra of OD in TiO_2. Recent EPR studies of OH in TiO_2 provide further experimental support for this model [4.9-4.10]. In these studies, electrons from two distinct sources, namely H_i and substitutional F, were found to be localized at two distinctly different Ti atoms. In our model, we propose that each energy level, as shown in Fig. 4.25 (b), corresponds to the localization of an electron from H_i at a different Ti location. For E_1, we propose that the localization of the electron occurs at Ti_1 in reference to Fig. 4.25 (a), consistent with EPR results for neutral H at low temperature [4.10]. We suggest that the electron is localized at Ti_2 for E_2. For E_3, the localization occurs at Ti_3 or $Ti_{3'}$ or any one of more distant Ti. This model provides a physical explanation for the three configurations with different energies that are required to explain the temperature dependence of IR spectra. Moreover, the high degeneracy determined for E_3 in our model could be associated with the possibility that the electron can be localized on a variety of more distant Ti atoms without significantly affecting the OD IR frequency.

A number of interesting issues remain open. For example, since the energy differences between configurations are too small to reliably determine their order by theory, the assignment of these configurations is not completely consistent with theoretical predictions

[4.30-4.32]. According to these predictions, the lowest energy configuration corresponds to electron localization on Ti_3 or $Ti_{3'}$ but this result is not consistent with EPR observations [4.10]. The inaccurate theoretical ordering with such small splittings may come from defect-defect interaction associated with supercell size. Therefore, the guidance of theory is general and not specific. Nonetheless, the consideration of both theoretical and experimental results suggests that the small splittings seen in IR spectra can be directly attributed to small polaron effects that are unique to TiO_2.

Another point that should be noted is related to the degeneracy of the level E_3. Although we have used g_3=19 to produce the satisfactory fits seen in Fig. 4.16 and Fig. 4.17, g_3>12 also gives satisfactory fits (Fig. 4.18 and Fig. 4.19), suggesting that g_3 must be large. E_3 and g_3 are the energy and degeneracy of an "effective level" that accounts for an extra electron that can be localized on any one of more distant Ti lattice atoms.

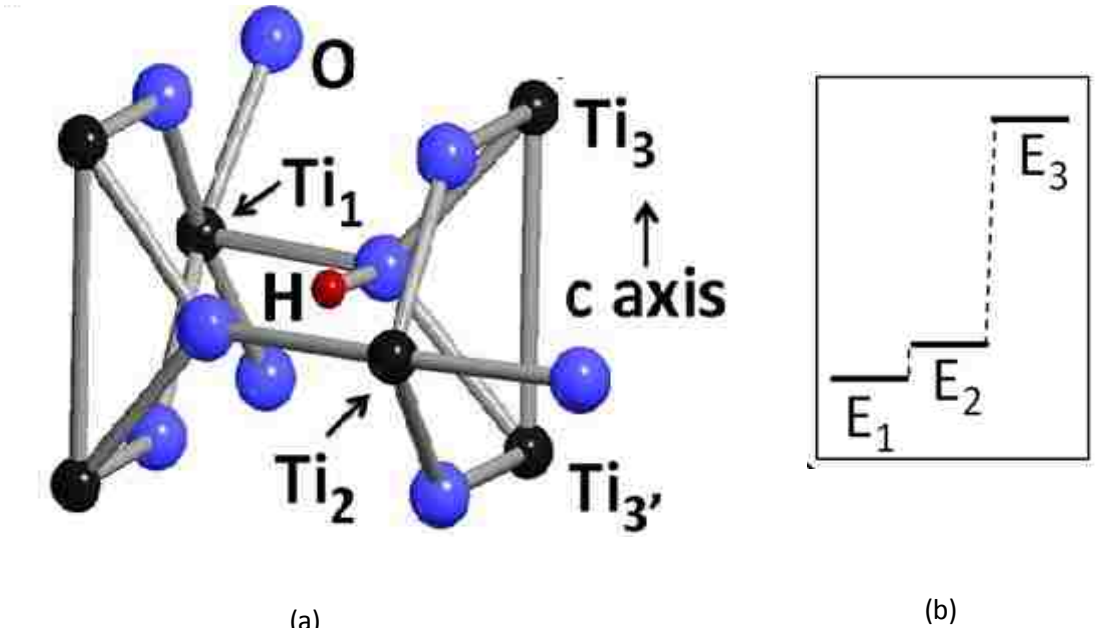

Fig. 4.25: a) The different configurations for the neutral OH (OD) center with a negative charge localized on different Ti^{3+} neighbors, drawn using Moldraw [3.7] b) Energies of three configurations used to fit the temperature dependence of the IR data.

4.4 TiO_2 Samples from Dresden

After our studies were completed, we arranged to exchange TiO_2 samples with the group in Dresden. These samples were grown by the Verneuil technique by Crystec GmbH (Germany). One sample is in its as-grown state and a second sample had been treated in D_2. IR spectra for these samples are shown in Fig. 4.26. These IR results are similar to the results we have obtained (seen in Fig. 4.14). Similar to our results, there is little, if any, free carrier absorption. The differences between our results and those of the Dresden group are not due

to differences between samples but rather are due to how we have chosen to interpret our data.

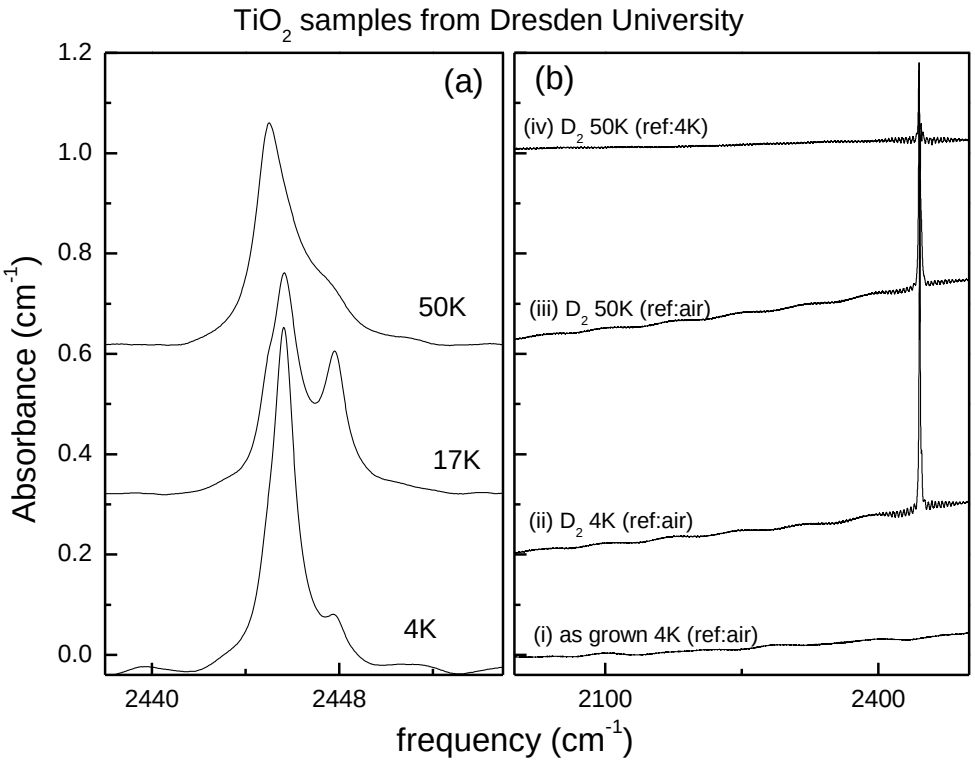

Fig. 4.26: (a) IR absorption spectra (T= 4 K, 17 K, and 50 K, resolution= 0.1cm^{-1}) of D_2 treated TiO_2 sample from Dresden measured with polarized light with **E**⊥**c**. (b) The free carrier absorption spectra of TiO_2 samples (as-grown and treated in D_2) measured at 4.2 ^{o}K and 50 ^{o}K with a resolution = 0.1 cm^{-1}. For spectra (i), (ii),and (iii), an empty sample holder was used as the reference but for the spectrum (iv), the spectrum measured at 4 ^{o}K was used as the reference.

4.5 Conclusion

Hydrogen and deuterium in rutile TiO_2 have been investigated by vibrational spectroscopy. New results obtained for samples previously studied by Bates and Perkins and a comparison of these results with those obtained for samples prepared at Lehigh allowed us to explain the different observations made by Herklotz *et al*. [4.11] and by Bates and Perkins [4.8]. When samples were treated in a D_2 ambient and quenched, the multiline structure arising from charged OD^- and a neutral OD center was observed in the spectrum. This result is consistent with recent observations made by Herklotz *et al*.. However, following a subsequent treatment in air, the sample becomes more fully oxygenated and the IR spectrum is simplified to a sharp, single line arising from the charged OD^- center, as was observed by Bates and Perkins.

After resolving the discrepancy between previous studies of OH and OD in TiO_2, we have extended our experiments to analyze the temperature dependence of the IR spectra. We have observed that the total concentration of the neutral OD center remains constant while the concentration of the charged OD^- center is unaffected by temperature changes over the test range of 3.5 K to 60 K. While these IR measurements have shown a temperature dependence similar to those of Herklotz *et al*. [4.11], a different model has been proposed to explain this behavior. According to the model of Herklotz *et al*., the neutral OD center acts as a shallow donor in TiO_2 with a binding energy of 10 meV. It is still an on-going subject of discussion whether the character of H is shallow or deep in TiO_2 [4.35-4.36], and within the scope of this work, we have not seen an evidence of a shallow character. Instead, we have proposed a small polaron model to explain the temperature dependence of the neutral OD

center. Theoretical calculations performed by Fowler have revealed that an excess electron arising from H_i tends to localize on a Ti lattice atom and forms a small polaron by displacing neighboring atoms. Moreover, depending on the choice of the initial position, the localization of the electron occurs at different Ti sites, giving slightly different energy configurations. This provides a microscopic explanation for the small splittings seen in the IR spectra arising from the neutral OD center. A large value for the degeneracy has been found for one of the energy configurations, suggesting an electron localizing on any one of several distant Ti atoms and therefore not changing the associated IR frequency significantly. In conclusion, the small polaron model finds that an electron becomes localized on a Ti atom and explains the unusual temperature dependence of a neutral OD center in TiO_2. The model is consistent with the findings of a recent EPR study of H and F in TiO_2 [4.10] and with recent theory.

Similar experimental and theoretical studies have been conducted also for an OH center in TiO_2 samples. A similar multiline structure and temperature behavior have been observed for OH and we have been able to analyze this center with a similar approach. However, since the OH line shapes are broader, revealing less detail, useful information about isotope effects on the position of the three line structure could not be extracted from IR data. The analysis of the OH center finds a behavior that is consistent with the properties found by more detailed analysis that was possible for OD.

REFERENCES

[4.1] U. Diebold, *Surface Science Reports*, **48**, 53 (2003).

[4.2] M. D. McCluskey, M. C. Tarun, and S. T. Teklemichael, *J. Mater. Res.*, **27**(17), 2190, (2012).

[4.3] S. Klauer and M. Wöhlecke, *Phys. Rev. B***, 49**, 158, (1994).

[4.4] R.J. Swope, J. R. Smyth, and A. C. Larson, *Am. Mineralogist,* **80**, 448 ,(1995).

[4.5] O. W. Johnson, S. –H. Paek, and J. W. DeFord, *J. Appl. Phys.*, **46**, 10226, (1975).

[4.6] J. B. Bates, J. C. Wang, and R. A. Perkins, *Phys. Rev. B***, 19**, 4130, (1979).

[4.7] E. J. Spahr, L. Wen, M. Stavola, L. A. Boatner, L. C. Feldman, N. H. Tolk, and G. Lüpke, *Phys. Rev. Lett.*, **104**, 205901, (2010).

[4.8] J. B. Bates and R. A. Perkins, *Phys. Rev. B*, **16**, 3713, (1977).

[4.9] Shan Yang and L. E. Halliburton, *Phys. Rev. B*, **81**, 035204, (2010).

[4.10] A. T. Brant, Shan Yang, N. C. Giles, and L. E. Halliburton, *J. Appl. Phys.*, **110**, 053714, (2011).

[4.11] F. Herklotz, E. V. Lavrov, and J. Weber, *Phys. Rev. B*, **83**, 235202, (2011).

[4.12] P. Y. Yu and M. Cardona, *Fundamentals of Semiconductors, Physics and Materials Properties* (Springer, Berlin, 2010), 4th ed.

[4.13] D. C. Cronemeyer, *Phys. Rev.*, **113**, 1222, (1959).

[4.14] O. W. Johnson, W. D. Ohlsen, and P. I. Kingsbury, Jr., *Phys. Rev.*, **175**, 1102, (1968).

[4.15] R. Dovesi, V. R. Saunders, C. Roetti, R. Orlando, C. M. Zicovich-Wilson, F. Pascale, B. Civalleri, K. Doll, N. M. Harrison, I. J. Bush, Ph. D'Arco, and M. Llunell, ***Crystal06 User's Manual***, University of Torino, Torino, 2006.

[4.16] A. D. Becke, *Phys. Rev. A* **, 38**, 3098, (1988).

[4.17] C. Lee, W. Yang, and R. G. Parr, *Phys. Rev. B,* **37**, 785, (1988).

[4.18] R. Krishnan, J. S. Binkley, R. Seeger, and J. A. Pople, *J. Chem. Phys.*, **72**, 650, (1980).

[4.19] J. E. Jaffe and A. C. Hess, *Phys. Rev. B*, **48**, 7903, (1993).

[4.20] J. Muscat, Ph.D. thesis, University of Manchester, 1999; J. Scaranto and S. Giorgianni, J. Mol. Struct. Theochem **858**, 72 (2008).

[4.21] L. Chiodo, J. M. García-Lastra, A. Iacomino, S. Ossicini, J. Zhao, H. Petek, and A. Rubio, *Phys. Rev. B*, **82**, 045207, (2010).

[4.22] M. Mikami, S. Nakamura, O. Kitao, H. Arakawa and X. Gonze, *Jpn. J. Appl. Phys.*, 39, L 847, (2000).

[4.23] F. Labat, P. Baranek, C. Domain, C. Minot, and C. Adamo, *J. Chem. Phys.*, **126**, 154703, (2007).

[4.24] S. Yang, L. E. Halliburton, A. Manivannan, P. H. Bunton, D. B. Baker, M. Klemm, S. Horn, and A. Fuhishima, *Appl. Phys. Lett.* , **94**, 162114, (2009).

[4.25] D. Emin, *Phys. Today* , **35(6)**, 34, (1982).

[4.26] A. Yidiz, F. Iacomi, and D. Mardare, *J. Appl. Phys.*, **108**, 083701, (2010).

[4.27] B. J. Morgan, D. O. Scanlon, and G. W. Watson, *J. Mater. Chem.*, **19**, 5175, (2009).

[4.28] Analysis of time-domain spectroscopy experiments by E. Hendry, F. Wang, J. Shan, T. F. Heinz, and M. Bonn, *Phys. Rev. B,* **69**, 081101(R), (2004) suggests intermediate coupling of the polaron, in contrast to the work cited above.

[4.29] J. Pascual, J. Camassel, and H. Mathieu, *Phys. Rev. B*, **18**, 5606, (1978).

[4.30] F. Filippone, G. Mattioli, P. Alippi, and A. Amore Bonapasta, *Phys. Rev. B*, **80**, 245203, (2009).

[4.31] J. Stausholm-Møller, H. H. Kristoffersen, B. Hinnemann, G. K. H. Madsen, and B. Hammer*, J. Chem. Phys.*, **133**, 144708, (2010).

[4.32] P. Deák, B. Aradi, and T. Frauenheim, *Phys. Rev.*, B **83**, 155207, (2011).

[4.33] W. B. Fowler, A. Murphy, and M. Stavola, Bull. Am. Phys. Soc. **56(1)**, Q12.00009 92011).

[4.34] P. Ugliengo, D. Viterbo, and G. Chiari, Z. Kristallogr. **207**, 9 (1993).

[4.35] S. F. J. Cox *et al*., *J. Phys.: Condens. Matter*, **18**, 1079, (2006)

[4.36] W. P. Chen, Y. Wang, and H. L. W. Chan, Appl. Phys. Lett. **92**, 112907, (2008).

Chapter 5

Conclusion

The hydrogen-related defects in two rutile-structure transparent metal oxides, namely SnO_2 and TiO_2, have been studied by FTIR spectroscopy. Hydrogen impurities have been known to be an important factor in the electrical and optical properties of metal oxide semiconductors which are unusual materials that combine electrical conductivity and optical transparency in the visible range.

The first oxide investigated was SnO_2, and the subject of interest was the determination of the thermal stabilities of the O-H centers in hydrogen and deuterium-treated samples and their relationship to the free carriers that are introduced by shallow donors. We found that electrically inactive hydrogen that is already present in as-grown samples interacts with native defects to give rise to O-H centers and shallow donors during heat treatment. Two H-related donors that give rise to free carriers were found to be present in these samples through an annealing study. The first donor is marginally stable at room temperature and was assigned to H_i and to the O-H line at 3156.1 cm^{-1}, in agreement with a previous assignment by Hlaing Oo *et al*. A second shallow donor was assigned to H at an oxygen vacancy ,H_o, that is a more thermally stable donor (up to near 600°C). About 35% of the free carrier absorption was determined to be due to H_i while the remaining 65% was from H_o.

Thermal treatment of SnO_2 also produced additional O-H and $(O\text{-}H)_2$ centers that do not give rise to free carriers. Our IR spectroscopy studies utilizing the annealing and polarization properties of hydrogen or deuterium treated samples revealed that an inter-

conversion between electrically inactive centers and H-related shallow donors can occur. We investigated the structure and chemical reactions of several O-H and $(O\text{-}H)_2$ centers, taking advantage of their distinctive polarization properties in our experiments and theoretical work performed in collaboration with Prof. Fowler. The polarization data and theoretical calculations contradicted the previous assignment of the line at 3281.8 cm^{-1} to H being trapped at a Sn vacancy and with an axial configuration. We proposed that the line 3281.8 cm^{-1} is due to H being trapped next to an interstitial Sn atom with some relaxation from the normal to the c-axis. Using the polarization data and theory, the 3334.2 and 3343.2 cm^{-1} lines were assigned to an $(O\text{-}H)_2$ center trapped by an interstitial Sn atom. A IR line at 3339.0 cm^{-1} was proposed to be due to the (O-H—D-O) form of the same center.

Rutile TiO_2 was the second metal oxide studied. We began our experiments on TiO_2 by resolving a discrepancy between the observations of two earlier studies of the OD center and the IR lines near 2445 cm^{-1} that OD give rise to. Our experiments revealed that the multiline or the single line structures, reported by two different groups, were obtained depending on the oxygenation level of the D_2 treated samples.

The temperature dependence of the IR spectra was then investigated. Although similar IR results to those from a previous study done by Herklotz *et al.* were obtained, we presented a different interpretation and model to explain the observe temperature dependence. Herklotz *et al.* related the multiline structure to different (neutral and positive) charge states of the same OD center and assigned the neutral OD center to a shallow donor. In our experimental data, the positive charge state (OD^-) showed insignificant temperature dependence and also the total concentration of the neutral OD center remained constant over

the test range 3.5 K to 60 K. In addition, our measurements did not show appreciable free carrier absorption, so we have not seen evidence for the shallow character of OD within the scope of this work. Instead, we have proposed a different model related to the neutral OD center only. With the help of Prof. Fowler's theoretical calculations, we explained the physical meaning of the temperature dependence of the neutral OD center. These calculations revealed that an excess electron arising from H_i tends to localize on a Ti lattice atom and forms a small polaron that arises from the displacements of neighboring atoms. Moreover, depending on the choice of the initial position, the localization of the electron occurs at different Ti sites, giving slightly different energy configurations. This provides a microscopic explanation for the small splittings seen in the IR spectra arising from the neutral OD center. In summary, we propose a small polaron model to describe the temperature dependence of the neutral OD center that has at least three configurations with different energies.

My experimental studies reveal how hydrogen can change the properties of transparent metal oxides. Further research needs to be done to fully understand the effects of hydrogen on the properties of these unique materials. Our research group plans to investigate hydrogen in other metal oxides, such as In_2O_3, MgO and ZnO.

Vita

Figen Bekisli was born in Nazilli, Turkey on January 10th, 1979. She started her undergraduate studies at the Middle East Technical University (METU) in September, 1997 and graduated with a B.S degree from the Physics Education Department in May, 2002. In the fall of the same year, she started working as a physics teacher in a private educational institution in Ankara and taught high school and freshmen level college physics for 4 years. Her graduate work in the Physics Department at Lehigh University started in the beginning of the Fall 2008 semester. She served as a Teaching Assistant for the first two years of her graduate studies. She also began working in the Solid-State Spectroscopy Lab under the supervision of Prof. Michael Stavola during the summer of 2009 and continued her research in this group, focusing on the physics of hydrogen in semiconductors studied by infrared spectroscopy. She has worked as a Research Assistant in this group between 2010 and 2013 and specialized particularly on the effects of hydrogen in semiconducting oxides.